NNT : 2016SACLS417

Thèse de doctorat de l'Université Paris-Saclay préparée à L'Université Paris Sud

Ecole doctorale n°564
Physique en Île-de-France
Spécialité de doctorat: Physique

par

Arlensiú Eréndira Celis Retana

Gap en graphène sur des surfaces nanostructurées de SiC et des surfaces vicinales de métaux nobles.

Thèse présentée et soutenue à Saint-Aubin, le 10 novembre 2016.

Composition du Jury :

Mme.	Odile Stephan	Professeur Université Paris-Sud	(Présidente du jury)
Mme.	Francine Solal	Professeur Université de Rennes 1	(Rapporteure)
M.	Jean-Marc Themlin	Professeur Université d'Aix-Marseille	(Rapporteur)
M.	Edward Conrad	Professeur Georgia Tech Physics	(Examinateur)
Mme.	Laurence Magaud	Directeur de recherche Institut Néel	(Examinatrice)
Mme.	Muriel Sicot	Chargé de recherche Université de Lorraine	(Examinatrice)
M.	Antonio Tejeda	Chargé de recherche Université Paris-Sud	(Directeur de thèse)
Mme.	Amina Taleb-Ibrahimi	Directeur de recherche Synchrotron Soleil	(Co-directrice de thèse)

Acknowledgments

I would like to thank first of all the jury members Pr. Francine Solal, Pr. Jean-Marc Themlin, Pr. Odile Stephan, Laurence Magaud and Pr. Edward Conrad, for their insight, fruitful discussions, interest and advice in this work. As my thesis developed in three main sites (Université Paris Sud, Synchrotron Soleil and Université de Lorraine), there are numerous people I would like to acknowledge and thank for their contribution to this thesis work.

To my thesis director, Antonio Tejeda, you were more than I could wish for in a supervisor, as you were very involved in my work, whether it was from the office next door or from any country around the world. For these past three and a half years I appreciated greatly the trust you put in me, from small things as the first time I mounted a sample (which took a few hours) until the end where I could perform experimental campaigns on my own. I could always rely on you and I feel very lucky to have had such a supportive supervisor. Every time I started to doubt myself you were always there to remind me the value of what I was doing (like our 4-point graph, which is actually a great deal of work !). I will always remember the joy I felt when something went exactly as we planned and how eager I was to show you the results, as I knew you would be just as excited as me; you truly understand the satisfaction of science well-made. And never forget the time the security people confused me with your kid, which always brings a smile to our faces.

To my thesis co-director, Amina Taleb-Ibrahimi, I want to thank you because you made me feel like a part of your family by giving me advice not only on the scientific plane but also on the personal one. I know you were working from the shadows and always had a good word to say about me. You never hesitated to tell me the good and the bad, and I appreciate your honesty. I am also glad I could share with you experiences outside of the thesis framework, as the amazing discovery of the best restaurant in Barcelona (that I will keep on visiting). Thank you for your trust, your support, your advices and your cakes !

To my thesis godmother, Alina Vlad, I want to thank you for your disponibility and encouragement words. Every talk we have is always a pleasure.

During my stay at the Université de Lorraine, I met wonderful people that helped me expand my scientific knowledge. I would like to thank the director of the "Surfaces et Spectroscopies" team, Daniel Malterre, for your kind welcome to the team, for your interest in my work, for the opportunity to experience your great teaching and your challenging questions that always kept my head spinning. This first year wouldn't have been possible without the supervision of Muriel Sicot. We spent together numerous STM/STS experimental sessions on the iridium system, in which I tried to absorb from you as much as I could (this lead to numerous "cahiers" full of tiny notes until the finest detail). I appreciate your sense of detail and I was especially glad that you could understand my struggles with the size of the experimental setup. Thank you for your patience, your experience and your support.

As part of the "Surfaces et Spectroscopies" group, I am grateful to Luc Moreau, for his never-ending help when my arms were too tiny to reach the helium entry of the microscope, when I needed help to transport the nitrogen tank through the university, as well as his thoughts on the importance of knowing what is happening inside the black box instead of just pushing a button. I would also like to thank the rest of the Surface and Spectroscopies team, Bertrand Kierren and Yannick Fagot-Revurat, for their great conversation at lunch time or any time we crossed each other at a conference. To Julien Granet, you were a great office mate for the one year I was in Nancy. Thank you for your help and advice with the microscope, as well as your humour and kindness. To Guillaume Vasseur, you made me feel at home when I was in Nancy, you were so patient with my very poor french when I arrived and always had time for a beer, dinner or coffee time and a little chat on how the experiments were doing.

At the Université de Paris Sud I had the opportunity to perform high level experiments and collaborate with experts on the STEM field. I would like to thank Alexandre Gloter and Alberto Zobelli from the "Microscopie électronique" group, for their contributions on the understanding of the graphene sidewall system from the experimental (STEM) and theoretical (DFT) point of view. In addition, I would like to thank Xiaoyan Li for her experience-sharing on the thinning process that I later adapted to the sidewall samples. I am grateful to Romain Bourrellier for the help on the very first trials we performed on graphene.

I also would like to thank the director of the Laboratoire de Physique des Solides - Sylvain Ravy and the "Lumière Ultrabrève, Cohérence et Èlectrons" team, namely

Marino Marsi, Evangelos Papalazarou, David Le Bolloc'h, Vincent Jacques, Nicolas Moisan, Carlo Spezzani and Luc Ortega for their fruitful discussions and interest in my work, as well as the casual day to day conversations at lunch time.

To the doctoral and post-doctoral colleagues of various teams, Min-I Lee, Isabel Gonzalez-Vallejo, Niloufar Nilforoushan, Lama Khalil, Marco Caputo, Ewen Bellec and Anna Tararan, I want to thank you for all the support, the coffee breaks and insightful conversations that most of the time had nothing to do with science. However, when a problem came (especially with Igor, yes, you know), I'm glad we could exchange solutions and also think about science. You made my stay at LPS very pleasing and full of surprises.

During these three years of PhD, I spent a fair amount of time at the Synchrotron Soleil in association with the Cassiopée beamline, where all my ARPES experiments were performed. I would like to thank the permanent staff of the beamline, François Bertran, Patrick Lefèvre, Julien Rault, Françoise Deschamps and Daniel Ragonnet for their support on my experimental campaigns, their trust, their kind words of encouragement and numerous conversations about french culture at lunch time. I would like to acknowledge the support of Stefan Kubsky and François Nicolas during the STM experimental campaigns on the platinum and iridium system and thank them for their flexibility on my laboratory requests and confidence in my handling of the Surface Laboratory chambers.

I would like to thank post-doctoral colleague Irene Palacio, with whom I began the study of the graphene sidewall system. You taught me to have confidence and to fight for what is right. I admire still the energy you have all the time. You helped me to grow both on the scientific and personal plane, and it was always fun to be around you. Thank you for your support and high hopes for me, you see, I made it.

To the post-doctoral colleague, Maya Narayanan, we spent a lot of time together, as long experimental campaigns, summer schools, conferences and even a trip to Atlanta with our collaborators. I want to thank you for all your support and help through my PhD. You have a very positive way of thinking and many stories to tell, especially when we had long beamtime hours. I think we became a well-oiled machine by the end of my PhD and I am grateful for having shared so many different experiences with you and to have learned from you.

I would also like to thank our collaborators from the Georgia Tech Institute, Walt de Heer, Claire Berger, Edward Conrad, and doctoral students Meredith Nevius, Feng Wang and Jean-Philippe Turmaud, as they provided the graphene sidewall samples

that were studied in this thesis work. I had the fortune to share numerous experimental campaigns with them, which deepened the quality of this work. Additionally, I spent two weeks in Atlanta at the Georgia Tech Institute, where I could learn from their growth techniques and have an enriching scientific exchange.

I want to thank my friends, for their support and love, close or far away, I carry you around with me, to Eliza, Liya, Yao, Andrea, Mariana, Aramís, Marifer, Kirill, Maria, Mario, Katerina, Erik, Philipp, Laura, Corinna, Tamara and Irving.

I also want to thank my family for their support, especially to my parents Virginia and Juan Carlos and to my brother Pavel. It was always difficult to understand what it is that I do, but it was a thrill to share this success with you (and thanks for the Mexican food at the "pot").

To Marc-Antoine, my life partner and best friend, thank you for your care, support, patience and understanding. I cannot begin to thank you for the sacrifices you made during the writing time, like all those times you had to cook at weird hours, or when we couldn't spend time watching our favourite series/movies. This was a success for both of us that would have never been possible without you.

Contents

Introduction

Electronic devices have become our everyday companions. They are everywhere in our lives since miniaturization has allowed extremely powerful devices to be portable. Miniaturization itself was made possible thanks to the development of nanoelectronics. In this seek for miniaturization, graphene has been extensively studied because of its many appealing properties, as its ability to dissipate heat, its high mobility, its high current carrying capabilities or its ballistic transport.

However, in order for graphene to be used as a transistor channel on electronics, it must be possible to switch between the on/off states (1/0 states) in an efficient way (fig. 1). The problem is that since graphene has a zero band gap, it is always conductive and hence always in the "on" state. In order to generate the "off" state, it is necessary to open a band gap in graphene, allowing to switch between conductive "on" state or non-conductive "off" state (fig. 1b). A great effort has thus been put into opening a band gap in graphene without significantly affecting its mobility.

Strain can in principle open a gap [1–3], but the uniaxial strain to produce useful gaps for electronics is extremely high and not realistically achievable. Chemical methods have also been proposed, based on doping or functionalization by an atom or a molecule [4–8]. Doping leading to gaps as large as 1 eV and hydrogenation up to $\sim$ 700 meV were reported [4, 5, 9–11]. Because of the nature of the chemical grafting process, disorder is almost inevitable, which leads to a significant degradation of the mobility.

A particularly elegant method to open a band gap is by electronic confinement [12, 13]. For certain graphene ribbons of a few nm in width, theory predicts that the band gap varies as a function of the ribbon width W [12, 13] with $\Delta E(W) \sim 1$ eV$\cdot nm\ W^{-1}$. This means that a band gap of $\sim$ 100 meV is expected for a ribbon of 10 nm, or conversely, a ribbon of width $\sim$ 1 nm would be required to get the band gap of silicon ($\sim$1 eV). As quantum confinement only relies on the geometric structure of the ribbon, the band gap can in principle be varied at will, contrary to the fixed band gap of a semiconductor silicon.

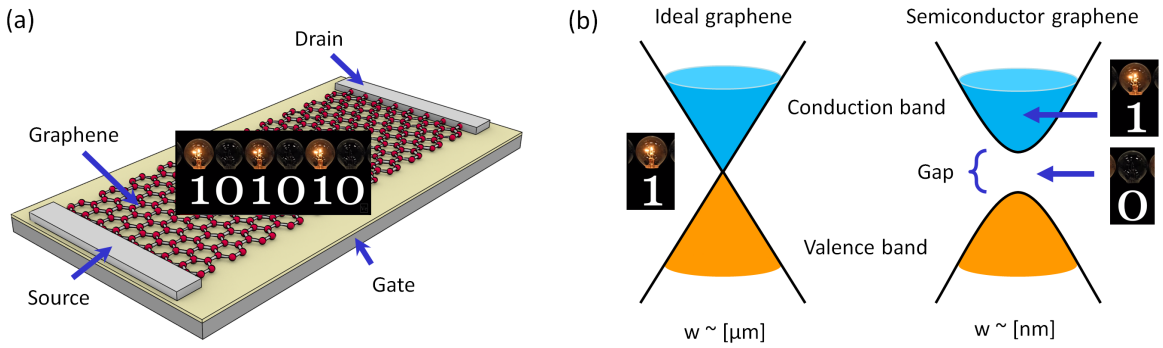

Figure 1: (a) Scheme of a transistor with graphene as its main conduction channel ideally producing both on/off states, represented by 1-0. (b) Electronic band diagram from ideal and semiconducting graphene. On ideal graphene, the "on" state is always present, as electrons can move freely from the valence to the conduction band. On semiconducting graphene, by opening a band gap we can obtain both the "on" (conductive) and "off" (non-conductive) states.

This thesis is precisely dedicated to the correlation between fabrication methods with the atomic structure and electronic properties. An introduction to the general physics of nanoribbons and the existing methods of synthesis is presented in chapter 1. We have focused on obtaining graphene nanoribbons by combining pre-structured substrates and an adequate growth method. The goal is to understand the ways of opening band gaps by nanostructuring in view of later tailoring a band gap opening. We have studied all these systems by ARPES, STM and STEM, which are described in chapter 2. We have used two approaches to open band gaps in graphene: the growth on vicinal metallic substrates (known for the catalytic decoupling of ethylene to promote graphene growth) and on annealed lithographic trenches on SiC. The metallic substrates used for the first approach are vicinal Ir and a curved multivicinal Pt exhibiting different vicinalities. Both on iridium and platinum, we were able to obtain a gapped electronic structure due to a periodic finite potential barrier on a continuous graphene layer. The combined results of the vicinal Ir and multivicinal Pt allowed us to explore the factors contributing to the band gap opening experimentally and by modeling. We have in particular studied the potential strength as a function of the periodic nanostructure, the vicinality type and the step-edge type. These results are described in chapters 3 and 4.

On our second approach, we studied graphene grown on annealed lithographed trenches on SiC (or sidewalls). The growth was performed by our collaborators in Georgia Tech. Motivated by the observation in ARPES of a band gap with unknown atomic origin, we performed a thorough structural study to understand the unexplored

graphene sidewall atomic structure and the origin of the band gap. By performing various microscopic and spectroscopic measurements, we conclude that the system consists of a continuous graphene layer subdivided in a large metallic nanoribbon on a sidewall SiC facet bordered by semiconducting miniribbons. These 1-2 nm wide semiconducting nanoribbons are responsible for the band gap opening via electronic confinement. These results are presented in chapter 5.

The manuscript ends with the conclusions, where we present a summary of the ways of opening band gaps on graphene, as well as the perspectives of my work.

Chapter 1

Fundamentals of graphene nanoribbons

1.1 Structure and electronic properties

Graphene consists of a single layer of carbon atoms in a honeycomb arrangement with carbon-carbon distance $a \approx 1.42$ Å. The hexagonal network has a motif of two atoms per cell (each atom corresponding to a inequivalent sublattice A (yellow) or B (green) in fig. 1.1) and a lattice parameter of 2.46 Å. The reciprocal lattice is also hexagonal rotated 30° with respect to the real space lattice. The lattice vectors and the reciprocal-lattice vectors are given by:

$$\mathbf{a} = \frac{a}{2}(3, \sqrt{3}) \ , \ \mathbf{b} = \frac{a}{2}(3, -\sqrt{3}) \tag{1.1}$$

$$\mathbf{a}^* = \frac{2\pi}{3a}(1, \sqrt{3}) \ , \ \mathbf{b}^* = \frac{2\pi}{3a}(1, -\sqrt{3}) \tag{1.2}$$

The band structure of graphene by tight-binding is:

$$E_{\pm}(k) = \pm t\sqrt{3 + f(k)} - t' f(k) \tag{1.3}$$

$$f(k) = 2\cos\left(\sqrt{3}k_y a\right) + 4\cos\left(\frac{\sqrt{3}}{2}k_y a\right)\cos\left(\frac{\sqrt{3}}{2}k_x a\right) \tag{1.4}$$

where t is the hopping between different sublattices (first neighbours) and t' is the hopping in the same sublattice (second neighbours). The plus and minus subindex correspond to the π and π^* bands respectively. The dispersion relation is shown in fig. 1.2 for hopping parameters $t = 2.7eV$ and $t' = 0.2t$. Due to its characteristic

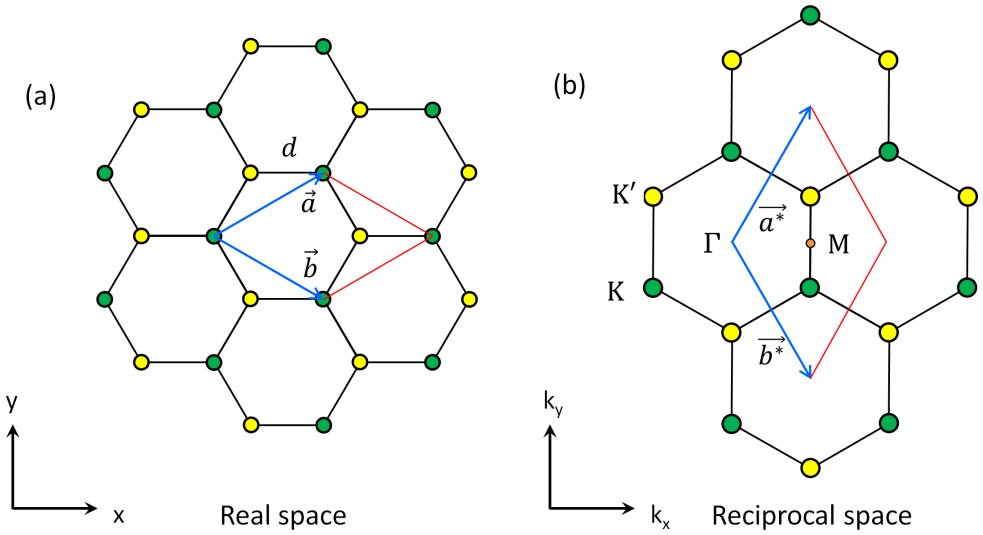

Figure 1.1: (a) Real lattice of graphene with hexagonal symmetry and two atoms per unit cell, (b) Four Brillouin zones showing the main high symmetry directions of reciprocal space ($\Gamma M = 1.475$ Å^{-1} and $\Gamma K = 1.703$ Å^{-1}).

atomic structure, the π and π^* bands touch each other at the K and K' points around the Fermi level (E_f), making of graphene a zero gap semi-metal. In the vicinity of the K points, the dispersion relation can be approximated by:

$$E_{\pm}(k) = \pm\hbar v_f k \tag{1.5}$$

which renders explicit the linear dispersion of graphene, where $v_f \simeq 1 \times 10^6$ m/s is the Fermi velocity.

When one spatial dimension of graphene is reduced to nanometric size, graphene nanoribbons are obtained. Ideal ribbons with simple edge orientation and termination, of extremely narrow width, and isolated from any substrate influence have been extensively seeked for. The edge termination is defined by the orientation of the ribbon with respect to the graphene lattice. Due to their high symmetry, the most studied graphene nanoribbons are those with zigzag and armchair edges. Zigzag ribbons have a honeycomb network oriented in such a way that the edge is made of the triangular edges of the hexagons (fig. 1.3a-top left). Armchair ribbons are oriented at 30° (or equivalently at 90°) from the zigzag orientation. In this case, the edge is made of hexagonal sides (fig. 1.3a-top right). All other ordered orientations are chiral.

Early tight-binding calculations [12, 13] have shown that the band structure of narrow ribbons depends on their orientation. Specifically, in these calculations, zigzag

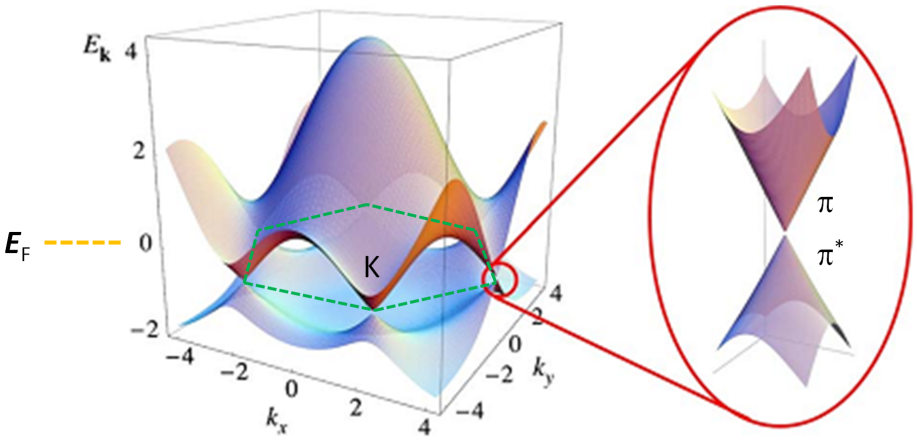

Figure 1.2: Electronic band structure of graphene around E_f in the tight-binding approximation with hopping parameters $t = 2.7eV$ and $t' = 0.2t$ [14].

ribbons are always metallic (fig. 1.3b) and armchair ribbons present an alternation of metallic and gapped electronic structures depending on the width. When present, the gap scales inversely with the ribbon's width. In fig. 1.3b, the calculated bands are projected either along the direction defined by the lattice parameter a (parallel to the armchair direction) or along z (parallel to the zigzag direction) (fig. 1.3a-bottom). With this convention, $\pi = k$ corresponds to the k-point where the Brillouin zone edge is reached along a^* or z^* reciprocal vectors, respectively [12] (fig. 1.3a-bottom). The width is characterized by N carbon dimer lines, which are different for armchair or zigzag ribbons, as presented in fig. 1.3a-top. The electronic structures for different values of N are shown in fig. 1.3b. Explicitly, the ribbon is metallic for $N = 3M - 1$, where M is an integer, and presents a gap otherwise. More recent ab initio calculations have confirmed the presence of a significant band gap in all 1 nm to ~ 4 nm wide armchair ribbons, with a gap value that decreases with width and oscillates with N [15, 17–21] (fig. 1.3c).

The situation is qualitatively different for zigzag ribbons, for which tight-binding calculations find a flat band at zero energy (highlighted by the box in fig. 1.3b) that corresponds to states that are located at the edge of the ribbons. These edge states produce a peak in the DOS at the Fermi level, enhancing the temperature dependence of their paramagnetic susceptibility. In the case of zigzag ribbons, first-principle calculations have shown that the flat band at zero energy found in simple tight-binding calculations is unstable relative to spin splitting. Magnetic ordering is predicted on the edges of narrow zigzag ribbons, with long-range ferromagnetic polarization along each

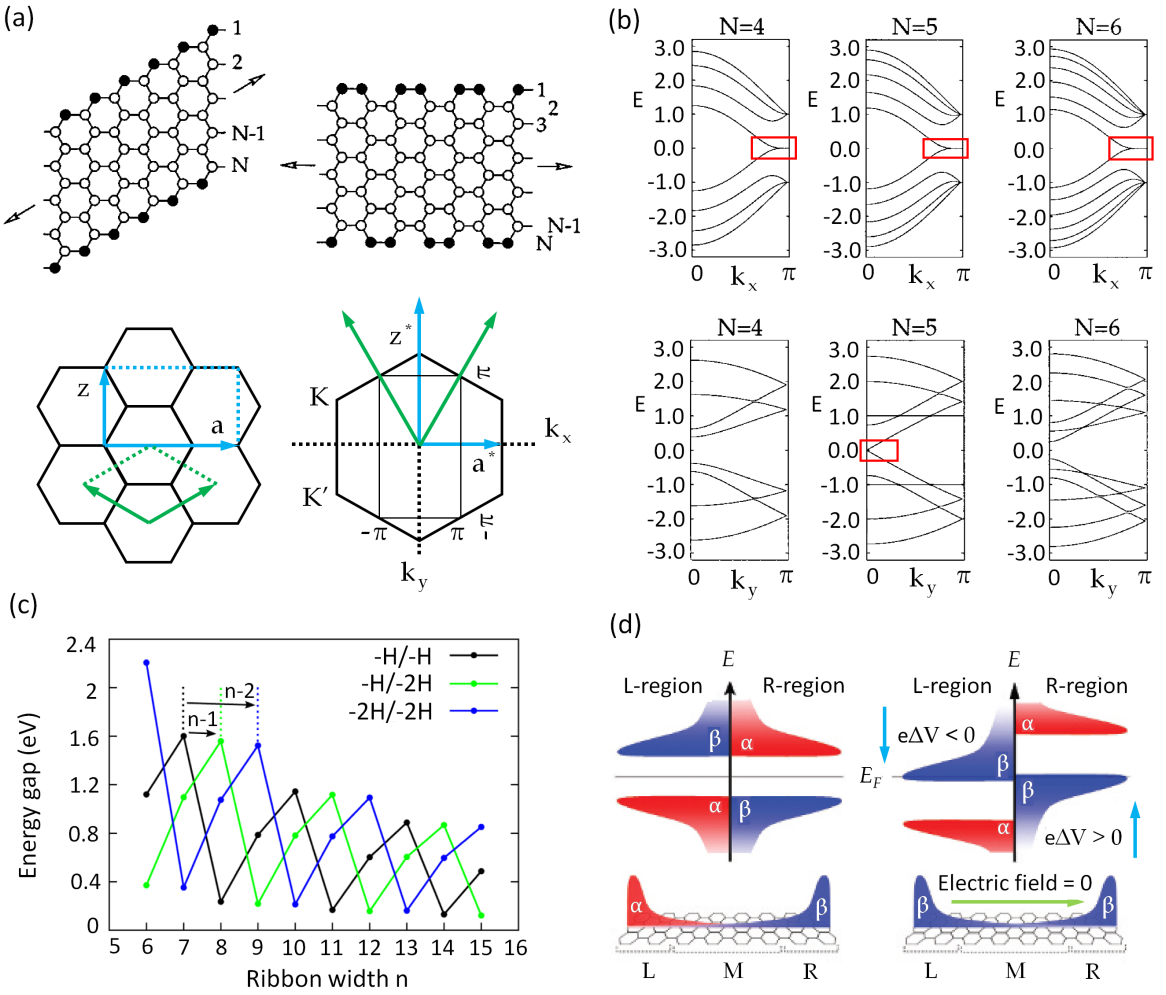

Figure 1.3: Theoretical properties of graphene nanoribbons. (a) Top: representation of a zigzag (left) and armchair nanoribbon (right). The arrows indicate the long direction of the ribbons. Bottom: scheme indicating the direction where the electronic structure in (b) was calculated. The left panel is the real space representing graphene and the right panel is its reciprocal space. The rectangular unit cell for calculations is defined by a and z. (b) Electronic band structure calculated by tight-binding for various graphene nanoribbon widths (N = 4, 5, 6, as defined in (a)). Top row: zigzag nanoribbons have a metallic state at E = 0. Bottom row: armchair nanoribbons exhibit either metallic or semiconducting behaviors, depending on the presence of an edge state at E_f (metallic states in the red box). The band gap is width-dependent [12]. (c) Density functional theory (DFT) calculations showing an oscillation of the band gap as a function of the ribbon width in functionalized armchair nanoribbons [15]. (d) ab initio calculation of the spin-resolved density of states (DOS) (top) and local DOS (bottom) of zigzag nanoribbons in the absence of an electric field (left). In the presence of a transverse electric field (right), the band at E_f is spin-polarized [16].

edge and anti-ferromagnetism across the ribbon of the edge states [13,22,23]. Therefore very close to charge neutrality, the electronic conductance is favored for one spin direction, which may have implications for spintronics. Half-metallicity is also proposed [16] by applying an in-plane electric field to modify the natural energy distribution of spins in the ribbon. This results in a single type of spin state at the Fermi level, as shown in fig. 1.3d. Another peculiarity of zigzag ribbons is that a perfectly conducting channel was predicted in tight-binding models, even in the presence of long-range impurity scattering [24]. This is because at charge neutrality, back-scattering requires a band of inverse dispersion dE/dk which is not present at the same K point in the Brillouin zone. This perfectly conducting channel is also predicted for chiral (non-armchair) ribbons. Exceptional transport properties are therefore expected for zigzag or chiral ribbons with perfect edges. All these properties strongly rely however on an atomic control of the width (smaller than a few nm) and of the edges of ribbons. It is thus extremely important to produce high-quality ribbons to obtain well-defined physical properties. In the following, we report the most common methods to produce graphene nanoribbons.

1.2 Preparation methods

Graphene nanoribbons can be synthesized by top–down or bottom–up approaches. The top–down approach consists of modifying a large graphene sheet (i.e. patterning) until a desired nanometric size and shape is reached. The bottom–up approach consists of assembling small building blocks to construct the desired larger object.

1.2.1 Top-down approaches

Lithographic patterning methods

Graphene nanoribbons can be fabricated by standard lithography and etching techniques from exfoliated graphene flakes, graphene grown on metals by chemical vapor deposition (CVD) or epitaxial graphene on SiC. For this, a mask is lithographically patterned on a graphene sheet so that graphene can be etched away by an oxygen plasma everywhere except for the strip protected by the mask [25–36].

Lithographic ribbons have been obtained with a minimum width down to about 10 nm [37,38]. Fig. 1.4a shows the schematic process for a nanowire mask and the resulting ribbons as imaged by a STM, after the mask was removed. Fig. 1.4b shows SEM

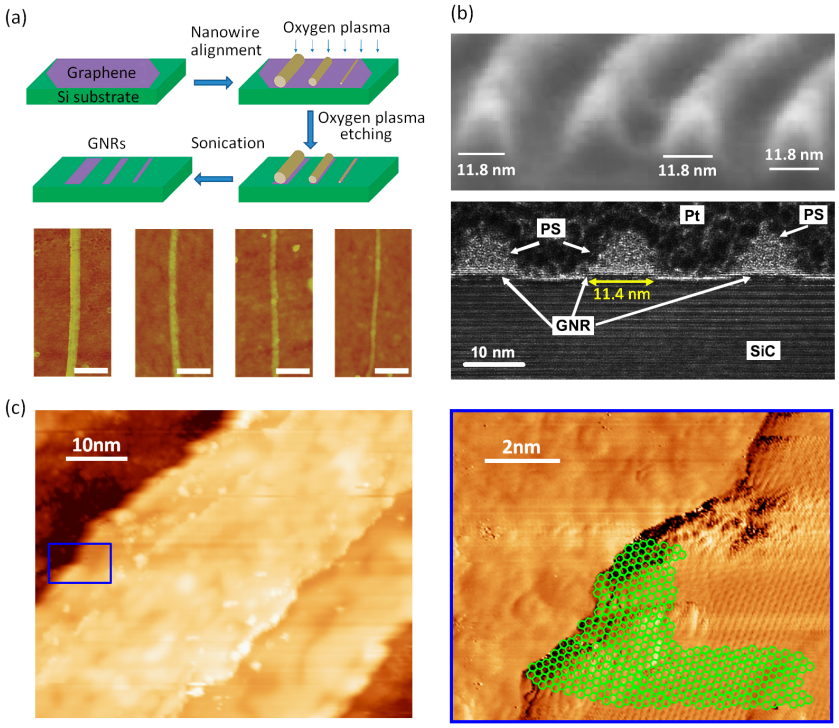

Figure 1.4: Lithographic ribbons. (a) Oxygen-plasma-patterned graphene nanoribbons with a nanowire protecting mask. Top panel: graphene is deposited on a substrate and nanowires are placed on top. An oxygen plasma etches away the unprotected graphene. The wires are removed and the nanoribbons are revealed on the substrate. Bottom panel: scanning tunneling microscope (STM) images of these nanoribbons [26]. (b) Microscopy images of lithographically-patterned graphene ribbons. Top panel: scanning electron microscopy (SEM) image showing the nanoribbon covered with the polystyrene etching mask resist. Bottom panel: cross-sectional transmission electron microscopy (TEM) image showing the ribbons with the polystyrene (PS) resist mask on top and a protecting platinum layer [27]. (c) E-beam lithographically-patterned graphene nanoribbons on SiC. Overall topography of the ribbon as seen by a STM (left) and zoom on the edge (rectangle) with atomic resolution (right) [-1.6 V, 0.1 nA].

and cross-sectional TEM image of an array of ∼10 nm wide nanoribbons. In this image the polymer mask was not removed for a better imaging of the spacing between the ribbons. The edge quality at an atomic level is better viewed by STM. Fig. 1.4c shows a STM image of a different ribbon obtained by e-beam lithography of epitaxial graphene on SiC. The edge has a nanometric corrugation that shows disorder, indicating how difficult it is to obtain pure zigzag or armchair edge types. A zoom of the image in the rectangle (fig. 1.4c-right) reveals the mixture of armchair and zigzag edges as highlighted by the superposition of the green graphene honeycomb structure. Rough edges come from the difficulty of patterning a resist with an electron beam at the atomic level, but also from the instability in the plasma etching process. Smooth and well-defined

edges and ribbon widths have not been demonstrated in lithographically-patterned graphene, although recent progress was made [38], and relatively high mobilities are reported $3500 cm^2 (V \cdot \mathrm{s})^{-1}$ [39].

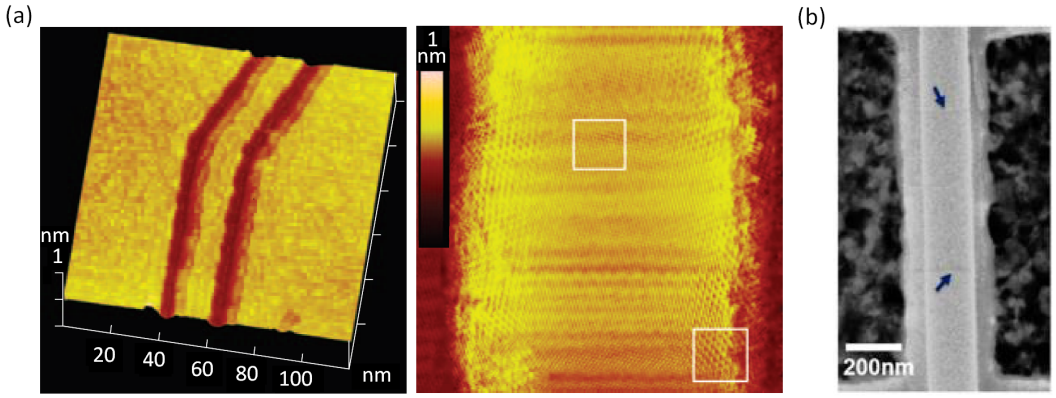

Figure 1.5: Local probe lithographic ribbons. (a) STM lithographic nanoribbons cut in highly-oriented pyrolytic graphite (HOPG). Left: STM image of a continuous nanoribbon with overall armchair and zigzag direction due to 30° change in the etching direction. Right: atomic resolution on the ribbon [40]. (b) TEM lithographic graphene nanoribbons. The arrows show the ribbon limits from suspended graphene [41].

Local probes not only allow direct observation of the quality of the edges, but they can also be used to etch material, and ribbon edges have been tailored with TEM, STM and Atomic Force Microscope (AFM). STM lithography has produced sub-10 nm nanoribbons cut out of HOPG along a desired crystallographic direction by applying high voltages to etch carbon away [40, 42]. AFM heated tips were used to locally deoxidize multilayer epitaxial graphene oxide to reduce it locally to graphene [43]; ribbon widths down to 12 nm were realized this way. AFM can be used on any kind of substrate and is therefore very versatile at producing nanostructures that can be directly measured [43].

Fig. 1.5a-left shows a nanoribbon initially etched in HOPG with a STM tip to obtain an overall armchair direction. The etch direction was then rotated by 30° to obtain a zigzag direction. Fig. 1.5a-right shows the degree of control that can be reached with this technique: the overall orientation can be selected with a nanometric precision although a significant edge disorder still remains due to the etching procedure. The lithographic principle is similar in TEM. Here energetic electron beams (>80 keV) can tailor ribbons down to width of 0.7 nm [41]. Fig. 1.5b shows a nanoribbon of hundreds of nm width tailored in this way from a suspended graphene flake. These images indicate that although these techniques are extremely local, control of the edge structure at the

atomic level remains a challenge. Moreover, these techniques are not well adapted for the large scale production of graphene nanoribbons. 'Millipede' microscopes could in principle use over 1000 tips for improving fabrication by parallel production [40].

Chemical methods

Chemical reactions give a high degree of control over the production of large quantities of graphene nanoribbons with a defined size distribution. In appropriate solutions, graphitic precursors (graphite or carbon-based molecules) can undergo chemical reactions that produce graphene nanoribbons in a powder or in a dispersed solution (fig. 1.6a) [44–47], with a ribbon size distribution centered around a specific value $\geq$ 1 nm. However, the ribbons are usually organized in a network, as shown by TEM in fig. 1.6b. It is possible to characterize individual nanoribbons, as in fig. 1.6c.

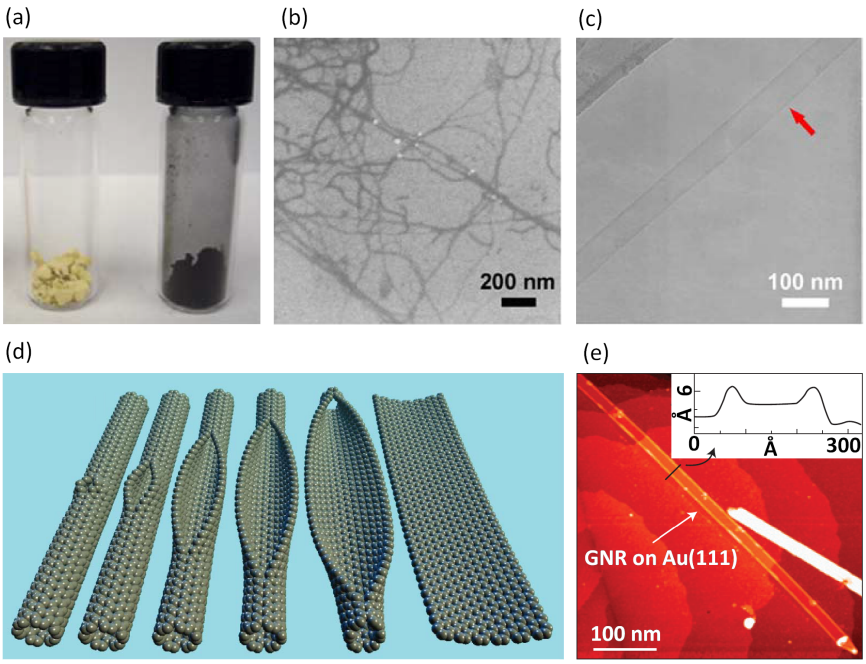

Figure 1.6: Graphene nanoribbons obtained by chemical methods. (a) Yellow precursor and final black graphene nanoribbon powder [44]. (b) SEM image of graphene nanoribbons dispersed in solution exhibiting a web-like structure. (c) TEM image of a single nanoribbon. The arrow points to a $\sim$ 60 nm wide nanoribbon [48]. (d) A schematic of the unzipping process of single wall carbon nanotubes (SWCNTs) into nanoribbons by chemical agents [48]. (e) STM image of unzipped carbon nanotube (CNT) deposited on Au(111). The inset shows the cross-sectional profile of the resulting ribbon [49].

The reported mobilities for this type of synthesis using time-resolved THz spectroscopy for ribbons dispersed in the liquid phase are within the range $150-15000\, cm^2(V\cdot \mathrm{s})^{-1}$

[50, 51]. Another chemical method exploits single wall carbon nanotubes (CNT) or multi-wall CNTs as graphitic precursors. These precursors are dispersed in solution with specific chemical agents that cause their walls to unzip. The unzipping process is schematically shown in fig. 1.6d. Selected nanoribbons are probed by a STM on a Au(111) substrate (fig. 1.6e). The width distribution, length and single/multiple layer character depend to a great extent on the initial CNT (diameter, single/multi-wall ratio of the batch and overall quality) [51–57].

Graphene cutting with catalytic particles

Carbon bonds can be dissociated via a catalytic reaction. Graphene nanostructures can be obtained from a graphene flake by depositing particles of a catalytic metal. In particular, metallic particles such as Fe or Ni interact with graphene in the presence of a hydrogen atmosphere and dissociate carbon-carbon bonds. This interaction etches the graphene while producing gas products composed of C and H, such as CH_4. Nanoribbons can be produced when the cutting paths of the particles run parallel to each other rather than cross, creating graphene nanoribbons as narrow as 10 nm with well-defined edges [58–60]. The directionality of the cutting paths is well-defined, as shown by the scheme of the AFM image of a graphene surface exposed to metallic particles (fig. 1.7). However the cutting directions cannot be predetermined so that a wide variety of graphene nanostructure shapes are obtained. If this technique is to lead to applications, further experimental work will be needed to control the nanoribbon shapes.

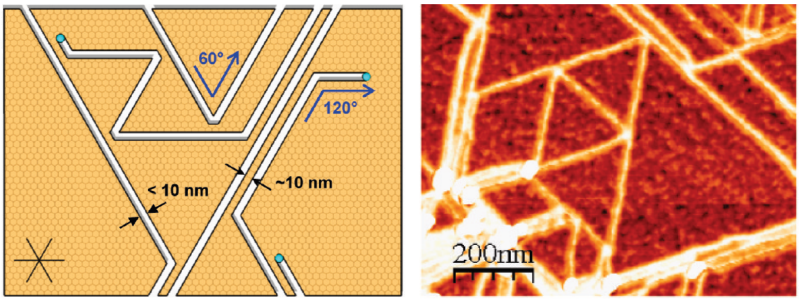

Figure 1.7: Graphene nanoribbon obtained by cutting with catalytic particles. Left: Model of paths made by metallic particles when cutting graphene by a catalytic reaction. Nanoribbons can be as narrow as 10 nm and display preferential zigzag edges. Right: AFM phase contrast image, showing the resulting patterns that include ribbons, triangles and rhombus [58].

1.2.2 Bottom-up approaches

Molecular precursor-based growth

In this process, graphene nanoribbons are formed out of monomeric precursors that react at the surface of catalytic metals. Monomers like DBBA (10,10'-dibromo-9,9'-bianthryl) or its derivatives are sublimated onto a slightly hot metallic surface (∼200°C) to stimulate the production of polymeric chains. A subsequent higher temperature annealing (∼400°C) favors the dehydrogenation of the polymer chains, resulting in graphene nanoribbons, as shown by STM (fig. 1.8a) [61]. A variant consists of a room temperature deposition before annealing [69]. Photoemission experiments on aligned parallel ribbons allow their electronic properties to be probed with k resolution.

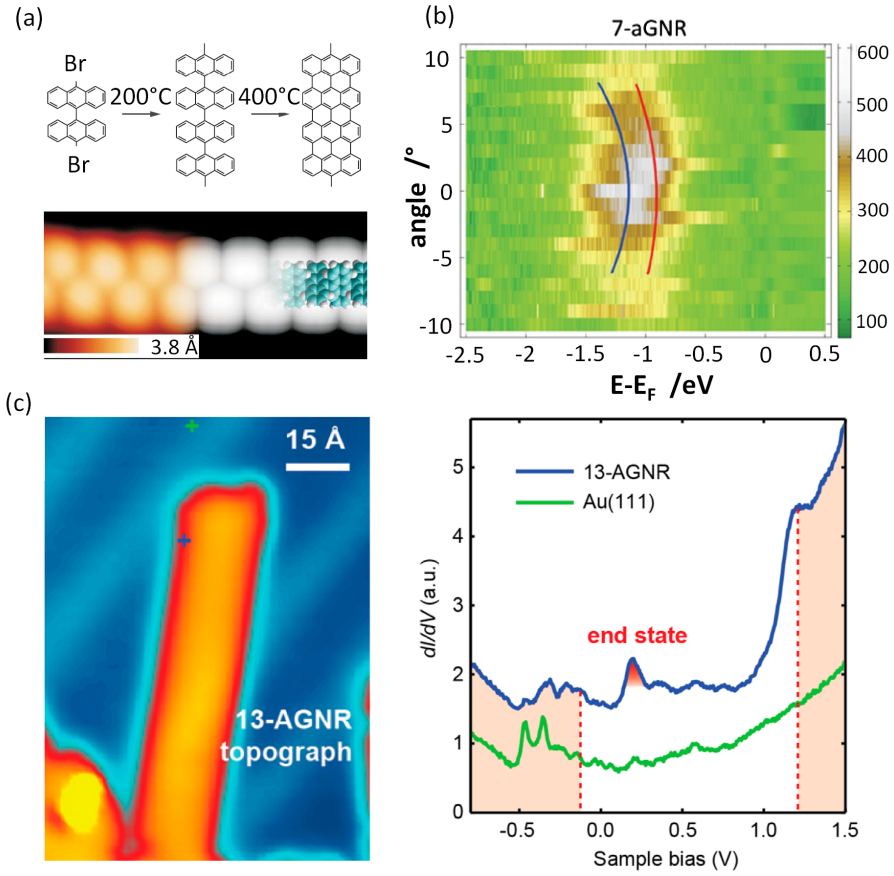

Figure 1.8: Molecular precursor-based nanoribbons. (a) Polymeric chain assembly reaction for DBBA molecules (top panel). STM image of the resulting armchair graphene nanoribbon (bottom panel) [61]. (b) Electronic states of armchair graphene nanoribbons in the direction along the ribbon [62]. (c) STM image of an armchair nanoribbon (left) and the dI/dV spectra on the edge (right), taken at the crosses in the left image [63].

Fig. 1.8b shows the electronic states of an armchair graphene nanoribbon at Γ, with a binding energy as large as 1 eV and with a low dispersion, indicating the localized nature of the spectral feature. A detailed analysis of the spectral weight reveals two components as expected from calculations [62], indicated in the figure by the two curved lines. Complementary information can be obtained by a STM, as local spectroscopy reveals the presence of 'end states' observed where the edge locally changes from armchair to zigzag (fig. 1.8c) [68]. All these studies show that while molecular precursor-based growth is restricted to metallic substrates, they provide a fruitful playground for fundamental studies of graphene nanoribbons.

Chemical Vapor Deposition

CVD can be used to generate graphene nanoribbons in a similar way to molecular precursor-based growth but in a single step. In this case a metallic template serves as the catalyst for the decomposition of hydrocarbons like ethylene (C_2H_4) or methane (CH_4) at high temperature (700–1000°C). Graphene forms by the assembly of the carbon atoms once the C-H bonds are broken. Depending on the catalytic template, the resulting nanoribbons vary in size [64–67].

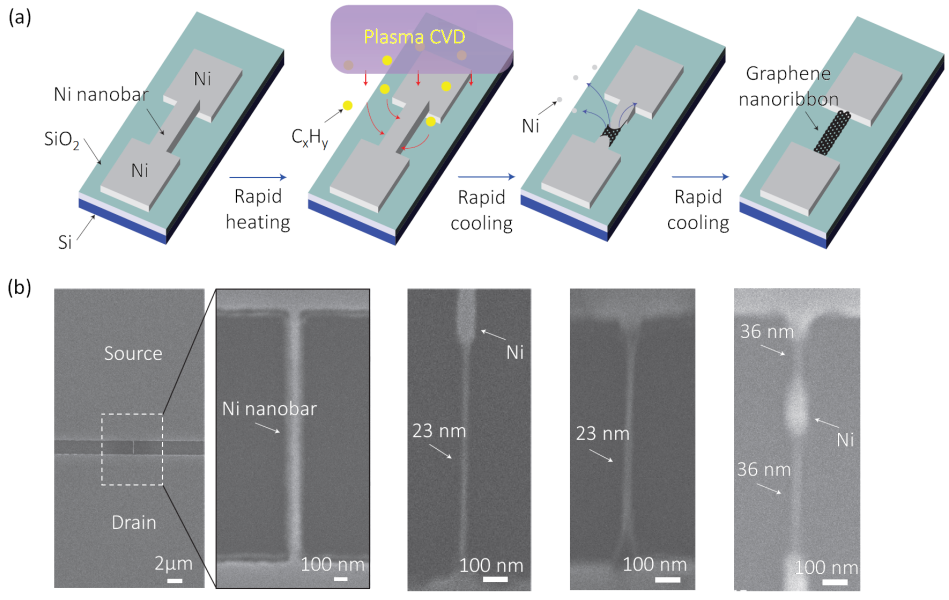

Figure 1.9: CVD ribbons. (a) Schematic of the CVD process to fabricate graphene nanoribbons by using Ni nanobars. From left to right: a Ni nanobar template is deposited on top of a substrate. Ethylene (C_2H_4) is exposed to the hot surface, where it reacts by catalysis with the Ni. Graphene is seeded on the bar until it covers it, generating a graphene nanoribbon. (b) SEM images of resulting nanoribbons with different sizes on the Ni template [64].

Fig. 1.9a describes the process for the nanoribbon growth. A Ni nanobar template is first evaporated onto a SiO_2/Si substrate. The substrate is then exposed to ethylene at high temperature, seeding the growth of the graphene nanoribbon at the nanobar. The precision of the size and shape of the nanoribbon is only limited by the ability to create proper templates. The SEM image of fig. 1.9b shows an example of a nanoribbon grown on Ni nanobars of various sizes connected to two electrodes. Note that the ribbon is sitting on a Ni template, and transfer methods are required for transport measurements.

1.3 Edge stability and edge states

Edge stability is an important aspect of nanoribbons if their electronic properties are to be tailored. In armchair ribbons, the theoretical gap is inversely proportional to the width. In zigzag ribbons tight-binding calculations predict metallic edge states [12, 13, 49, 68]. This expected behavior was observed by STM on a step edge of HOPG,

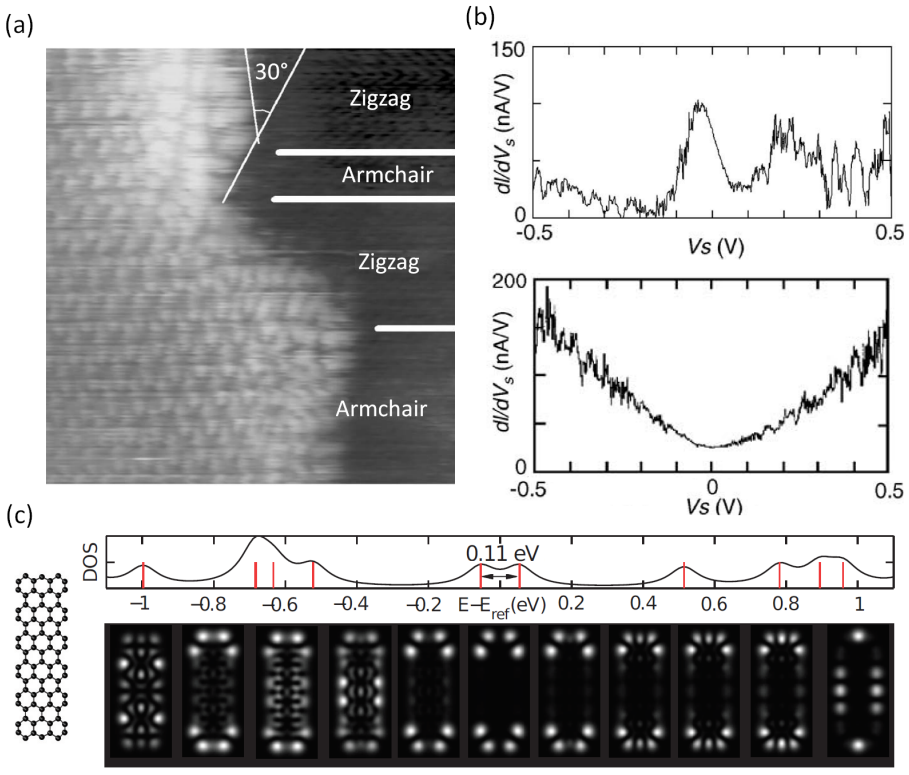

Figure 1.10: Edge states as a function of the edge orientation. (a) STM image showing a mixture of edges on graphite HOPG. (b) dI/dV spectra showing an edge state peak in the DOS for zigzag edges (top) and no peak for armchair edges (bottom) [68]. (c) Calculated DOS for a finite ribbon and simulated dI/dV maps at different energies for an s-wave tip [69].

(fig. 1.10a) where both armchair and zigzag orientations are shown. Scanning tunneling spectroscopy (STS) performed on both terminations confirms the presence of edge states on zigzag but not on armchair edges (fig. 1.10b). These measurements are consistent with DFT simulations for a finite armchair graphene nanoribbon, where the DOS is plotted versus the energy (fig. 1.10c). In the calculation, at $E = 0$, the armchair edges of the ribbon have a zero DOS, whereas a non zero DOS is located at the zigzag regions (fig. 1.10c). Edge states are observed by STS in ribbons obtained by opening SWCNTs [49].

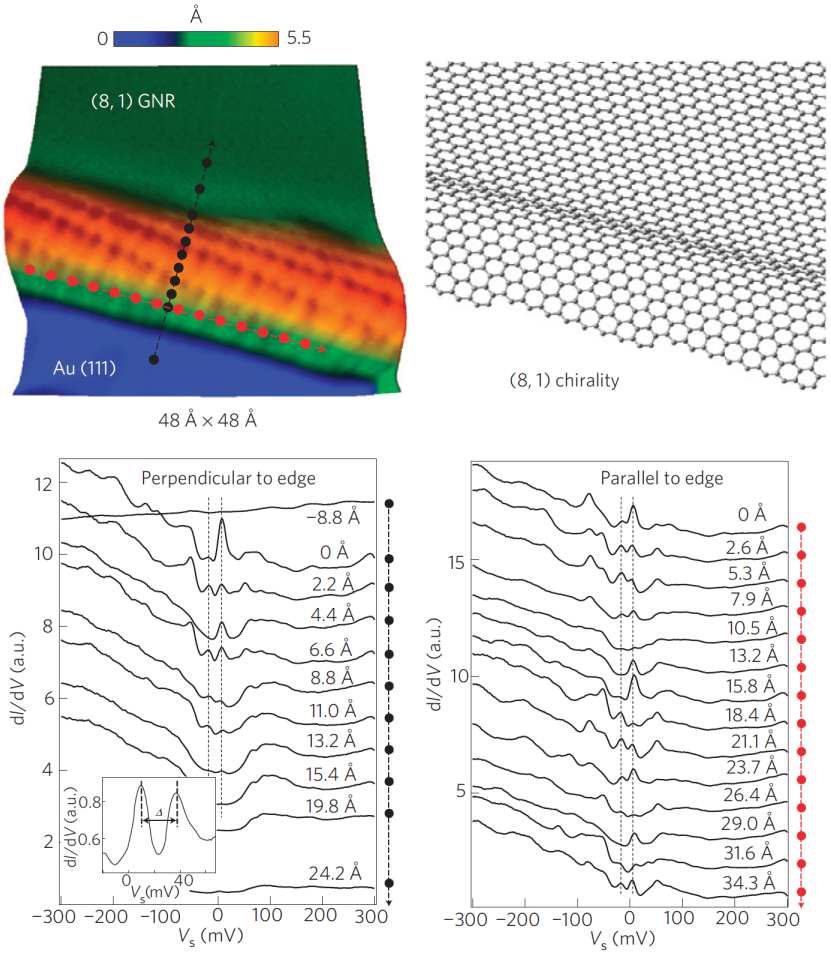

Figure 1.11: Edge states in a chiral ribbon fabricated by unzipping a CNT. Top panel: STM image of the ribbon and schematics of the edge. Lower panel: dI/dV curves measured in the direction parallel (red dots) and perpendicular to the edge (black dots). The oscillatory behavior of the peak intensity correlates with the structural periodicity of the edge [49].

Fig. 1.11 shows the spectra along the parallel and perpendicular directions to the edge of a ribbon with an edge different from a zigzag or armchair orientation (chiral). Peaks in the spectra correspond to states located at the ribbon edge. Periodic oscillations in

the peak amplitude are observed along the ribbon edge, correlated to the structural periodicity of the edge. The splitting of the peaks is attributed to spin-polarization of the edge as expected from theory [16, 21, 23]. In light of this structural dependence, the question of ribbon edge stability is relevant [70].

1.4 Transport gap

Band gaps can be determined unambiguously by spectroscopic measurements, either by optical absorption or by electronic structure measurements. The latter include STS, or a combination of photoemission spectroscopy (PES) and inverse photoemission

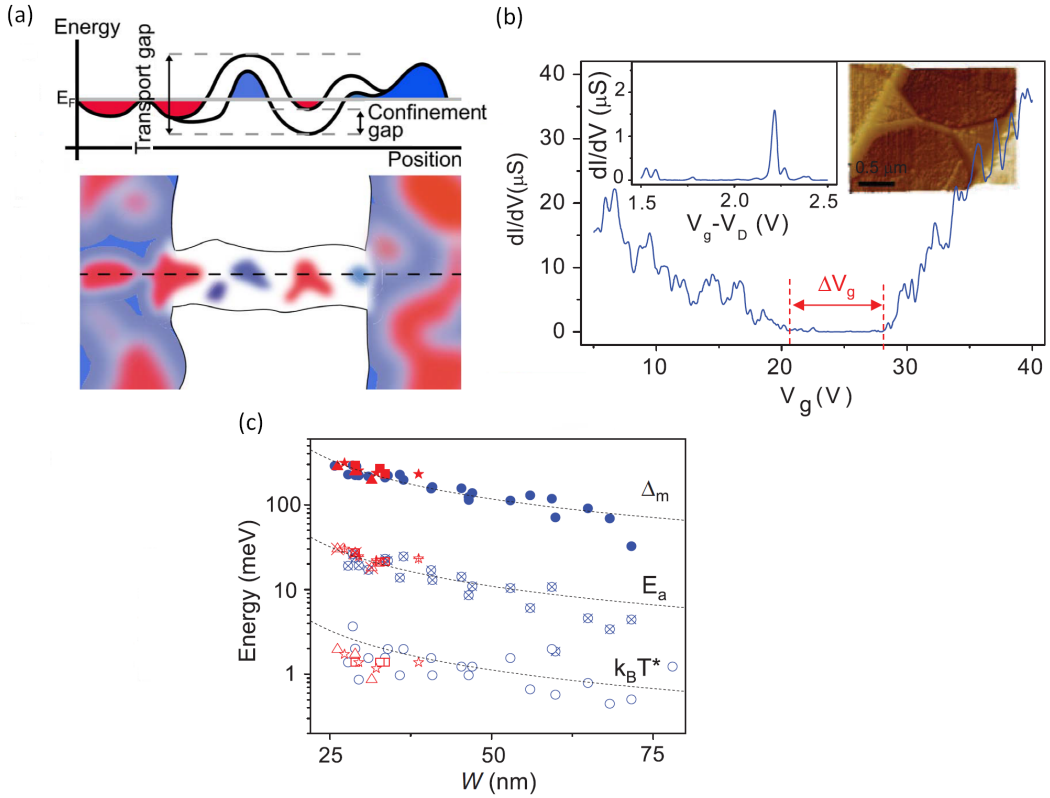

Figure 1.12: (a) Schematics of quantum dots created along a graphene nanoribbon creating a transport gap. The profile along the channel shows the comparison of the transport and the confinement gap [71]. (b) Differential conductance (dI/dV) as a function of back-gated voltage (V_g) near the charge neutrality point showing the transport gap region. Left inset: conductance peak present on the transport gap region. Right inset: AFM image of the graphene nanoribbon channel [72]. (c) Three energetic indicators (Δ_m—energy in the single particle energy spectrum, E_a—hopping energy, k_bT—characteristic temperature for activated transport) for the transport gap plotted versus the width of the nanoribbons, where each symbol represents a different ribbon length [72].

spectroscopy (IPES). Photoemission can determine the band gap when the Fermi energy is placed in the conduction band. Otherwise, when the Fermi level is somewhere within the band gap, photoemission gives a minimum value of the gap. Photoemission requires homogeneous areas for such determinations. STS has the advantage of being an atomic scale measurement, but does not probe the ribbon as a whole as is done in transport measurements. Transport measurements in general cannot distinguish between a vanishing conductance due to a true band gap (i.e. no states available) and a mobility gap due to localization effects (i.e. presence of non-conducting states). Very detailed low-temperature transport data analysis is required for that. In both cases, a vanishing conductance at low-bias voltage and a strong conductance increase with gate and bias voltages (i.e. large current on/off ratios) are expected, and these effects depend strongly on temperature.

In most of the ribbons, and especially in lithographically-patterned nanoribbons, defects associated with edge roughness and the inhomogeneous potential created by impurities create a series of interconnecting quantum dots (fig. 1.12a) [71, 73–75]. The overall effect of this potential is the onset of a 'transport gap', due to localization effects and Coulomb charge blocking. This means that the conductance drops to zero around the charge-neutrality point even in the absence of a true band gap. Fig. 1.12b shows the conductance as a function of bias for a graphene nanoribbon exhibiting a transport gap in the region of gate voltage ΔV_g. When the gapped region is analyzed more carefully (see the inset), small resonant conductance peaks can be seen. This gap is often inversely proportional to the width (fig. 1.12c) [31, 71, 72, 76], which makes it more difficult to unravel from a true band gap. The most recent published gap values, on/off ratios, resistances and mobilities for ribbons prepared with different processes are listed in Tables 1.1 and 1.2. The listed gaps are transport gaps (mostly at cryogenic temperature), unless otherwise specified.

Table 1.1: Band gap and structural properties.

	Fabrication methods	Orientation	Width(nm)		Gap(meV)	
Top-down	Conventional lithography	Not specified	4 - 500	[26,27,29,77], [31–36], [28,65,71–74,78]	4 - 500	[26,29,31], [34,74]
	Local Probe lithography	Not specified	0.7 - 12	[41,42]	100 - 500	[40,42]
		AC	2.5	[40]		
	Chemical	Not specified	3 - 300	[46,48,79]	10 - 400	[46]
	Unzipping CNTs	Not specified	10 - 300	[51,53–55,80,81]	10 - 50	[49,51]
		Chiral	80 - 200	[49]		
	Particle cutting	Not specified	>10	[59,60]	120 - 1600	[82]
		ZZ	>1.1	[58,82]		
Bottom-up	Molecular precursor-based	AC	0.7 - 13	[61–63,72,83]	1300 - 3100	[44,50,62]
		ZZ	1	[50]		[63,72–76,84]
	CVD	Not specified	20 - 3000	[64,66,67]	50 - 58.5	[64,66]
	Epitaxial graphene	Not specified	900	[85]	-	
Epi	Epitaxial sidewall	ZZ	40	[86,87]	-	
		AC	2 - 40	[88–90]	>500	[88]

Notes: Listed gap values are either transport gaps or band gaps. True band gaps are listed for local probe lithography (STS measurements [40,42]) and molecular precursor (PES-IPES [44,62], optical absorption [50], STS [32,84]) and unzipping CNTs (STS [49]) and epitaxial graphene (ARPES [88]). All others are transport measurements. Epi refers to graphene grown on SiC sidewalls as it will be discussed in chapter 5.

Table 1.2: Reported on/off ratio and transport properties for ribbons prepared with various processes.

	Fabrication methods	On/Off ratio		Resistance (KΩ)		Mobility ($cm^2(V{\cdot}s)^{-1}$)	
Top-down	Conventional lithography	5 - 1000 RT	[26,35] [34,65]	30 - 670	[29]	0.21 - 6000	[29,71] [35,65]
	Local probe lithography	-	[41]	100	[41]	-	[41]
	Chemical	10^7 RT	[46]	-	[46]	100 - 200	[46]
	Unzipping CNTs	10 - 100 RT	[54]	2	[51]	0.1 - 1500	[51,54] [81]
Bottom-up	Molecular precursor-based	-		-		150 - 150,000	[50]
	CVD	2 - 15,000 RT, LT	[64,66] [67]	100	[67]	40 - 1000	[64,66] [67]
	Epitaxial graphene	$5 \cdot 10^6$ RT	[38,85]	10	[85]	10 - 1000	[38,85]
Epi	Epitaxial sidewall	-		7 - 26	[87,90] [86]	2700 Ballistic	[90] [86]

Notes: RT (LT, respectively) refers to room temperature (cryogenic, respectively) measurements. Epi refers to graphene grown on SiC sidewalls as it will be discussed in chapter 5.

1.5 Devices

Integration of ribbons into devices has followed several directions, but all require junctions and heterojunctions. An example of an all-graphene pn junction was obtained by assembling different molecular precursors, connecting graphene ribbons with p- or n-doping in a continuous graphene ribbon [84], as shown in fig. 1.13a. Another example is epitaxial graphene, where the intercalation of one or two layers of Ge below the graphene layer changes the graphene doping from n to p respectively, creating small junctions (see fig. 1.13b) [91].

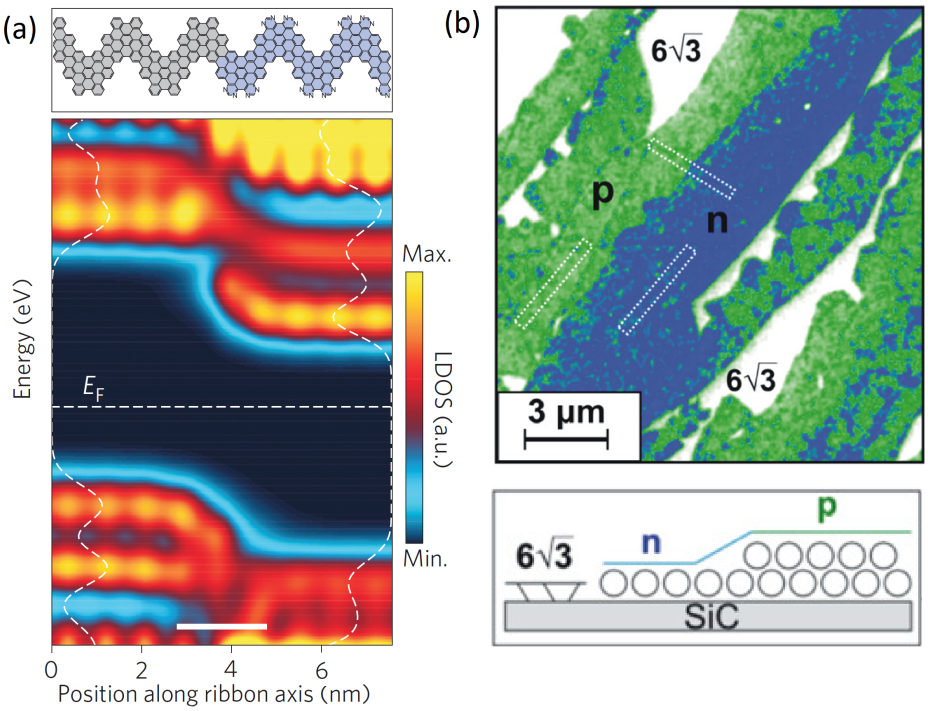

Figure 1.13: All graphene pn junctions. (a) Schematics of a graphene theoretical heterojunction, where the left part is p-doped and the right part is n-doped. Below the LDOS along the ribbon axis, as calculated by DFT, allows to visualize the pn junction [84]. (b) Color-coded SEM image of the n- (blue) and p-(green) doped areas obtained by the intercalation of one (two, respectively) layer of Ge at the interface between SiC and epitaxial graphene, as sketched in the bottom panel [91].

Although the intercalation is not very well controlled at this point it provides an easy route to both n- or p- doping depending on the number of the intercalated layers. In another instance, two-dimensional graphene was used as integrated leads in SiC semiconducting devices connecting a SiC channel [92] or an atomically thin SiC/Si_2O_3 channel [85]. Other devices integrating graphene nanoribbons include sensors [93, 94] or photodetectors [56, 95–97]. Fig. 1.14 shows some of the integration of graphene

nanoribbons in electronic devices. Fig. 1.14a presents a suspended graphene nanoribbon connected to multiple source-drain electrodes to measure its electronic properties. The electron beam of a TEM was used to nanosculpture the suspended ribbon into various widths so as to change its electronic properties [41]. Fig. 1.14b shows conventional lithography patterning on graphene flakes to obtain nanoribbons with different widths. Electrical measurements are possible due to the Pd source-drain contacts, back-gated on the substrate. Fig. 1.14c shows examples of graphene nanoribbons showing the feasibility of the production of large device networks in devices such as field-effect transistor (FET) [98–102]. The 50-FET array was obtained by CVD growth of graphene nanoribbons vertically along with four-contact electrodes on each ribbon (red inset) [66].

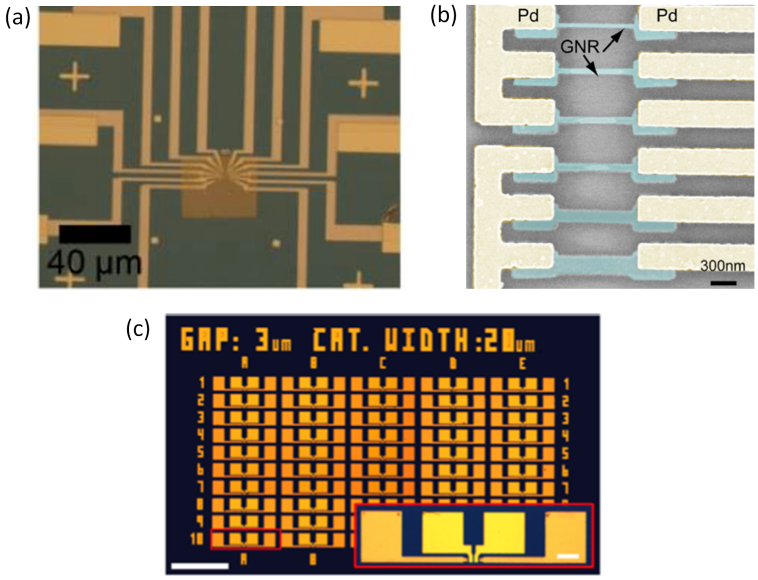

Figure 1.14: Devices. (a) A chip with multiple electrodes connected to a suspended graphene nanoribbon obtained by TEM lithography [41]. (b) FET device obtained by e-beam lithography patterning. The graphene nanoribbons are contacted by Pd electrodes [29]. (c) A 50 graphene nanoribbons FET array developed from CVD graphene on a catalyst template. The inset shows the four-electrode contact configuration [66].

Chapter 2

Experimental techniques

The structural and electronic analysis on surface science in general is better performed by using a set of complementary techniques. In our case, we have studied the electron properties of graphene nanoribbons by Angle-Resolved Photoemission Spectroscopy (ARPES), Scanning Tunneling Microscopy and Spectroscopy (STM/STS), Scanning Transmission Electron Microscopy (STEM) and Electron Energy Loss Spectroscopy (EELS). These techniques were performed at the Université Paris Sud (Laboratoire de Physique des Solides), at the Université de Lorraine (Institut Jean Lamour) and at the Soleil Synchrotron (Surface Laboratory and the Cassiopée Beamline). In the following, I will describe these techniques.

2.1 Scanning tunneling microscopy

The Scanning Tunneling Microscope (STM) is a microscope with the ability to resolve the atomic and electronic structure of conducting surfaces with a resolution of the order of the Å. The STM reaches such a resolution by scanning a sharp tip on top of the sample to be studied. When a potential is applied between the tip and the surface, electrons can flow between them without contact because of the quantum tunnel effect, which is the basis of the operating principle in STM. The main element in an STM is the tip (typically W or Pt-Ir) attached to a three axis piezodrive (x, y and z piezoelectric transducers). As the tip is positioned close to the sample, typically a few angstroms away, a potential eV is applied and a tunneling current I flows from the tip to the surface or viceversa via quantum tunneling through the vacuum. By detecting and recording the scanning parameters, a 3D image of the surface can be generated (fig. 2.1a).

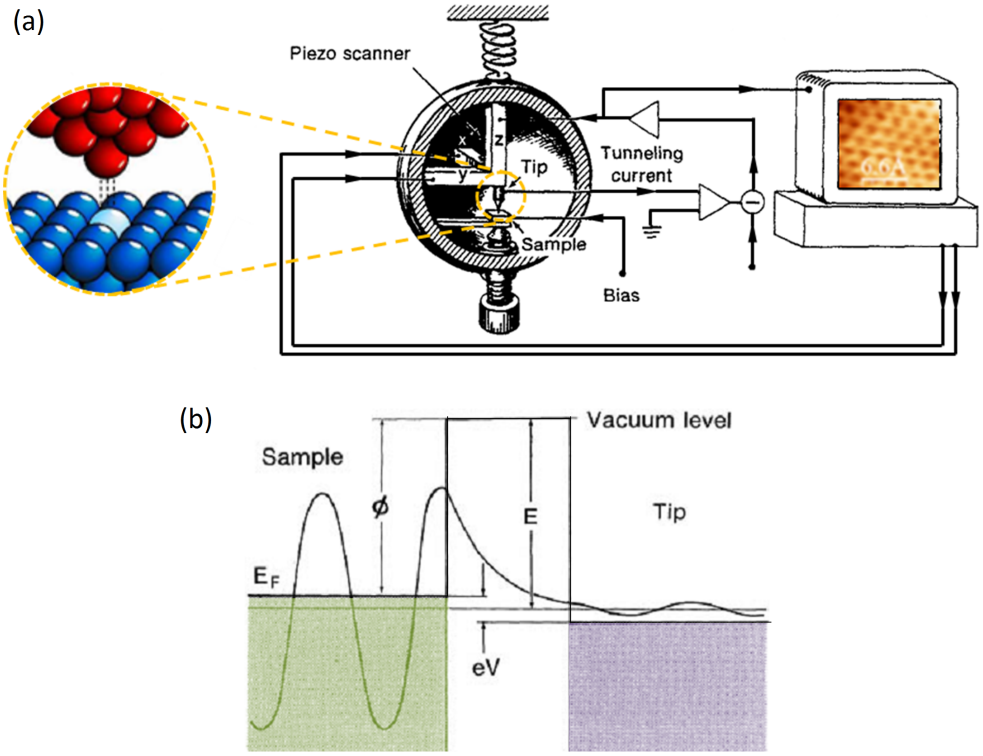

Figure 2.1: (a) Main elements of a Scanning Tunneling Microscope. The three piezo scanner is controlled by the applied bias to scan over the sample. By detecting the tunneling current between the tip and the sample, an STM image is generated [103, 104]. (b) Electron quantum tunneling effect principle applied for STM measurements. The bias eV is applied to the sample so that electrons can tunnel through the barrier given by the workfunction ϕ in vacuum and towards the tip [103]. The wavefunction can tunnel through the barrier even if its energy it's lower than the barrier height.

The energy diagram of the system is constituted by the sample and the tip with the vacuum in between is shown in fig. 2.1b. The vacuum is a potential barrier ($U(z) = \phi$) that electrons classically cannot penetrate if their energy is lower than the potential barrier ($E < U(z)$). However, in a quantum system, the wavefunction $\psi(z)$ satisfies the Schrödinger equation:

$$-\frac{\hbar^2}{2m}\frac{d^2}{dz^2}\psi(z) + U(z)\psi(z) = E\psi(z) \tag{2.1}$$

and has a solution in the classically forbidden region of the form $\psi(z) = \psi(0)e^{-\kappa z}$ where $\kappa = \sqrt{2m(U-E)}/\hbar$ is the wave vector that describes the decaying behavior as electrons penetrate through the barrier. The total tunneling current through the barrier depends on all the states between the Fermi level of the sample and the bias applied (E_F and $E_F - eV$) as:

$$I \propto \sum_{E_n=E_F-eV}^{E_F} |\psi_n(0)|^2 e^{-2\kappa z} \tag{2.2}$$

If eV is small enough so that the density of states does not vary significantly with it, the current I can be rewritten as a function of the local density of states as following:

$$\rho_s(z,E) \equiv \tfrac{1}{\epsilon} \sum_{E_n=E-\epsilon}^{E} |\psi_n(z)|^2 \tag{2.3}$$

$$I \propto eV\rho_s e^{-2\kappa z} \tag{2.4}$$

From this equation, the exponential sensitivity of the tunneling current with respect to the tip-surface distance is highlighted, which gives the resolution to this microscope. There are two types of scanning mode for an STM, as shown on fig. 2.2:

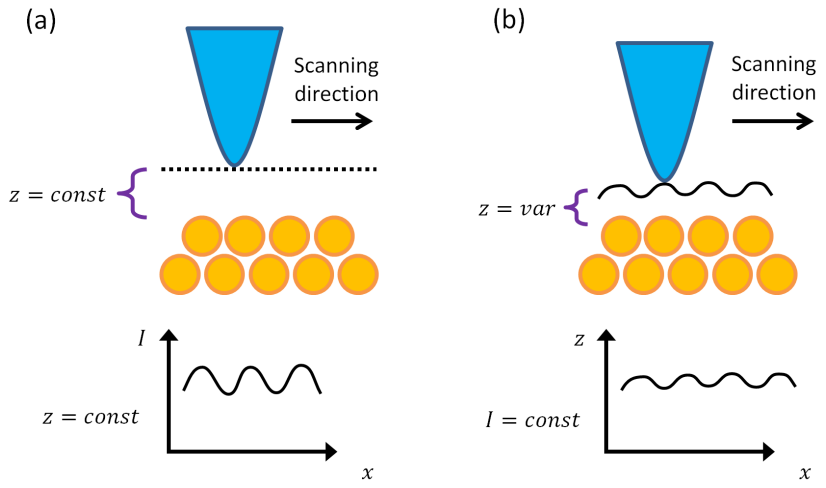

Figure 2.2: (a) Constant height mode, where the changes in tunneling current are measured along the surface while the height is kept constant. (b) Constant current mode, where the tunneling current is kept constant and the changes in height are recorded.

1) Constant height - the tip is kept at a constant height setpoint value while the surface is scanned and the changes in tunneling the current are recorded.

2) Constant current - the current between the tip and the surface is kept constant while the change in the height is recorded. A feedback look keeps the tunneling current constant as it moves over the surface. This is the most common mode.

To further acquire information on the local density of states of the sample, it is possible to perform scanning tunneling spectroscopy. As the electrons flow between the

tip and the surface, there is a convolution of the local density of states of the tip and the sample. If the tip has a constant density of states, the current flow gives information about the density of the states of the sample (Eq. 3.4). To do this, feedback of the constant current mode is interrupted at a given spatial location, so the tip-sample distance z is kept constant. Then the tunneling current is scanned as a function of the applied bias (dI/dV), which is proportional to the sample local density of states (from Eq. 3.4, $dI/dV \propto \rho_s$). The typical curves for a metallic and semiconducting material are shown on fig. 2.3.

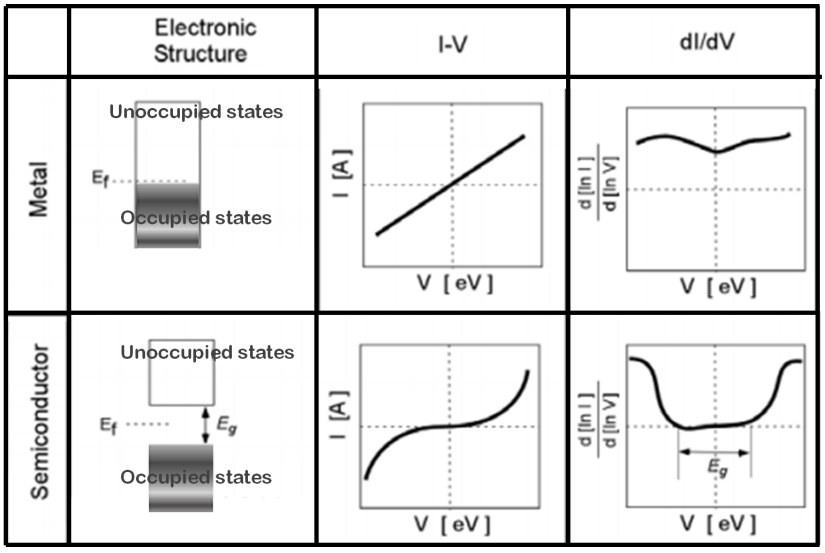

Figure 2.3: Band diagram, I-V and dI/dV typical STS curves for a metal and a semiconductor [105].

STM can be performed in a variety of environments and working temperatures. The experiments done at the Institut Jean Lamour were under vacuum, at RT, liquid-N_2 and He temperatures, allowing also to perform STS measurements at cryogenic temperatures. Experiments at the Surface Laboratory in Soleil Synchrotron were performed under vacuum at RT.

2.2 Scanning transmission electron microscopy

In Scanning Transmission Electron Microscopy (STEM), a narrow focused beam of electrons ($\sim$ 1 - 10 Å) is scanned through different positions of a thin sample ($\sim$ a few hundred nm thick). A detector at the lower part of the microscope column detects the transmitted electrons (fig. 2.4a).

An advantage of STEM over TEM is that the image is formed without imaging

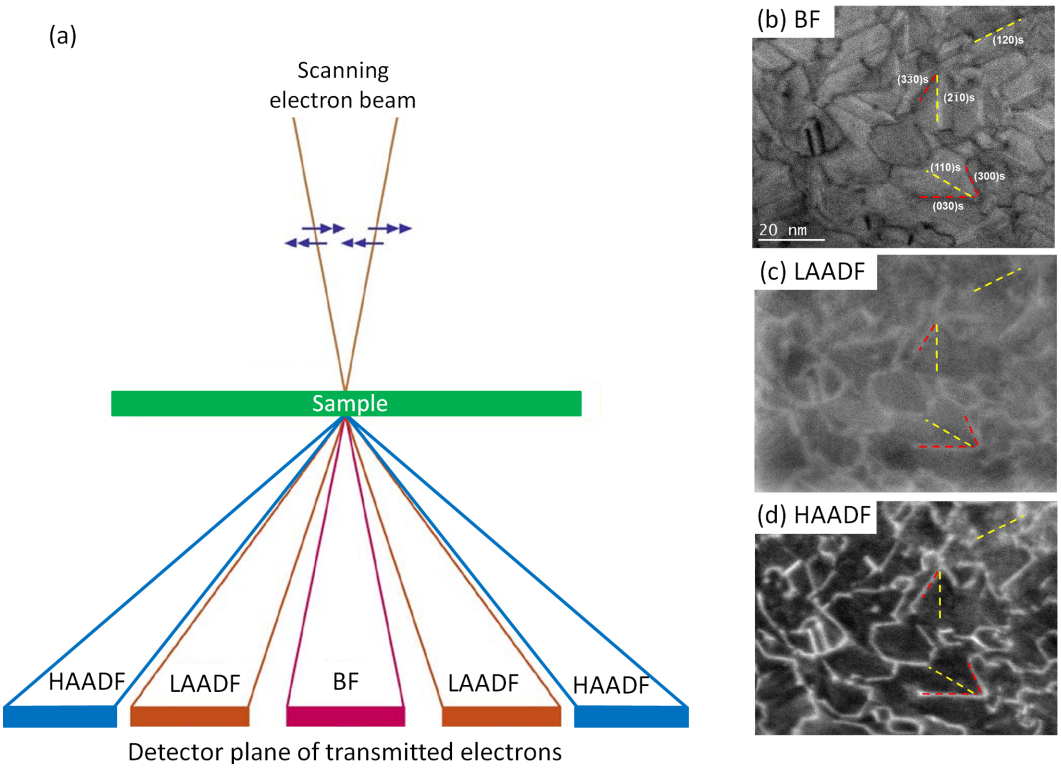

Figure 2.4: (a) Scheme showing the angular range to obtain the BF, LAADF and HAADF imaging modes of STEM [106]. (b) STEM image of a planar VO_2 thin film probed by the different modes [107].

lenses, therefore the resolution is only limited by the electron beam size, allowing the study of the atomic order of the electron density of the sample [106]. Different transmitted electrons can be collected according to the need of the study; we will mainly discuss three different modes, the bright-field (BF) mode, and two annular dark field (ADF) modes (high angular annular dark field-HAADF and low angular annular dark field-LAADF). BF images are obtained by positioning a detector that intercepts the direct transmitted beam, while the LAADF and HAADF are obtained by using annular detectors that surround the BF detector (fig. 2.4a). The LAADF mode allows to obtain images with a high contrasted intensity suited for light elements. On the other hand, the HAADF mode is sensitive to the atomic number of heavy elements (Z-contrast) [106, 108–110]. Since the ADF detects scattered electrons and the BF mode detects the direct-beam electrons, they are complementary modes. Fig. 2.4 shows a schematic for the three modes (panel a) and an example of measuring the same object with the three different modes (panels b-d).

STEM allows also to perform electron energy-loss spectroscopy, which gives information about the chemistry and electronic structure of the sample by collecting and

analyzing their energy distribution. In this way it is possible to obtain information about the bonding/valence state, nearest-neighbor atomic structure, dielectric response, free-electron density, bandgap and even the thickness [106]. The spatial resolution and sensibility of EELS is of the order of a single atom.

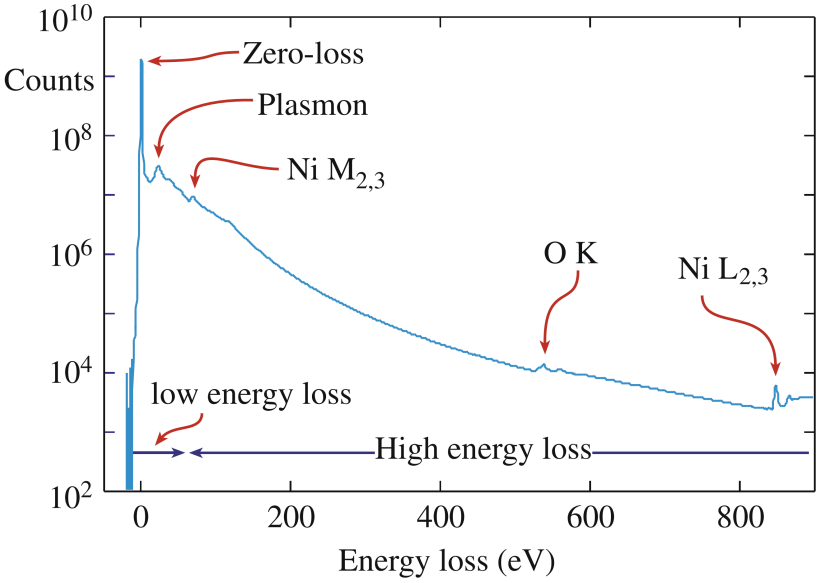

Figure 2.5: Typical EELS spectra for a fictional material showing the low and high energy loss regimes, where weakly and tightly bounded electron interactions can be found [106].

An EELS spectra for a fictive material is presented in fig. 2.5, showing the most common features. The most intense feature is the zero-loss peak. Plasmon features appear near to it and then the ionization edges of different chemical elements are observed. The spectra is divided into low and high energy loss regions. The low energy loss region provides information on the weakly bounded conduction and valence electrons, while the high-loss region is related to the tightly bounded or core-shell electrons [106]. Since this work focuses on the analysis of graphene, the EELS spectra here will focus on the carbon L-edge.

For this thesis, measurements were carried out at the Laboratoire de Physique des Solides in collaboration with Alexandre Gloter. The STEM measurements (BF, ADF and EELS) were performed on a STEM NION 200, where the spherical aberrations of the objective lens are corrected up to a 5^{th} order and the canyon type CFEG was used with an electron beam energy of 60 keV with a spatial resolution of $\sim$ 1 Å.

2.3 Angle resolved photoemission spectroscopy

Angle Resolved Photoemission Spectroscopy (ARPES) is a technique that allows obtaining information about the electronic states of a material, which are fundamental to understand their properties. The specificity of this technique is to allow the construction of an energy versus momentum map (E(k)) by analyzing the electrons coming from a sample. The working principle to eject electrons from the sample is the photoelectric effect, that describes the energy transfer from a photon to an electron of a material. When the photon energy ($h\nu$) allows the electron to overcome the energy barrier to escape the material (workfunction Φ) and its own binding energy to the system (E_b), by the principle of energy conservation, the kinetic energy of the outgoing electron is described by:

$$E_{kin} = h\nu - \Phi - E_b \tag{2.5}$$

This means that by measuring the kinetic energy of the outgoing electron, it is possible to retrieve the binding energy (E_b) of the electron inside the material. In order to construct the E(k) map, it is necessary to determine the momentum of the electrons. The electrons are ejected at a certain θ angle (fig. 2.6a). The measurement of the emission angle θ and the relationship between kinetic energy and momentum allows to retrieve the component of the momentum parallel to the surface.

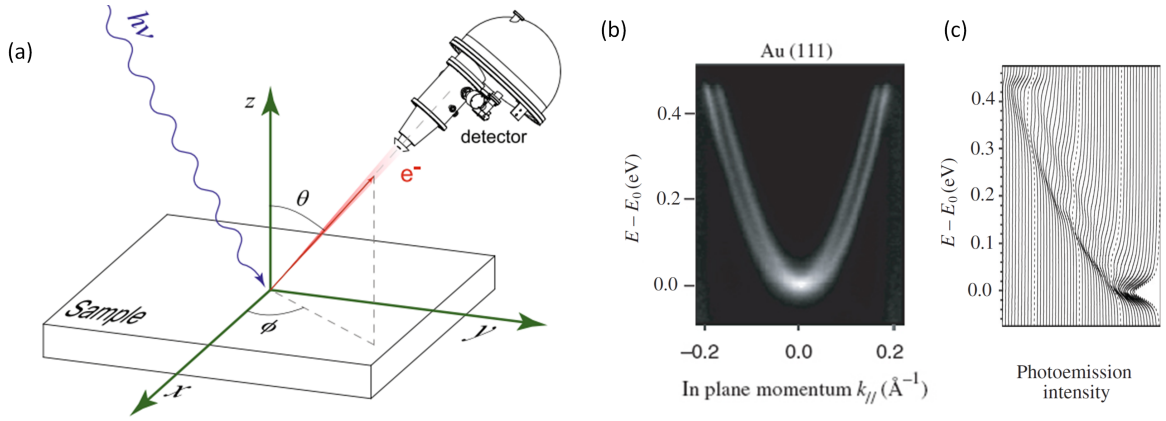

Figure 2.6: (a) Scheme of the ARPES configuration [111]. (b) E(k) map for a Au(111) surface [112]. (c) Energy Distribution Curves for the band dispersion on (b). Each line corresponds to an individual spectrum at a different emission angle.

Since the ejected electrons pass through a potential barrier as they exit the surface, the perpendicular component of the momentum is not conserved. However, the parallel momentum is conserved and is defined by:

$$p_{||} = \hbar k_{||} = p \sin\theta = \sqrt{2mE_{kin}} \cdot \sin\theta \tag{2.6}$$

where m is the mass of the electron [111, 113]. As the parallel momentum is conserved when the electron exits the solid, by measuring it in the vacuum is possible to obtain the momentum in the initial state. Therefore, by measuring both the energy and the emission angle, it is possible to recover the E(k) dispersion. Fig. 2.6a shows a semi-spherical analyzer collecting the outgoing electrons that are filtered by their kinetic energy and emission angle and are later collected on a CCD camera. The E(k) for a Au(111) surface measured in this way is shown on fig. 2.6b. A useful way to represent the E(k) band dispersion is via the Energy Distribution Curves (EDC), where the color-code is replaced by the numerical intensity (fig. 2.6c).

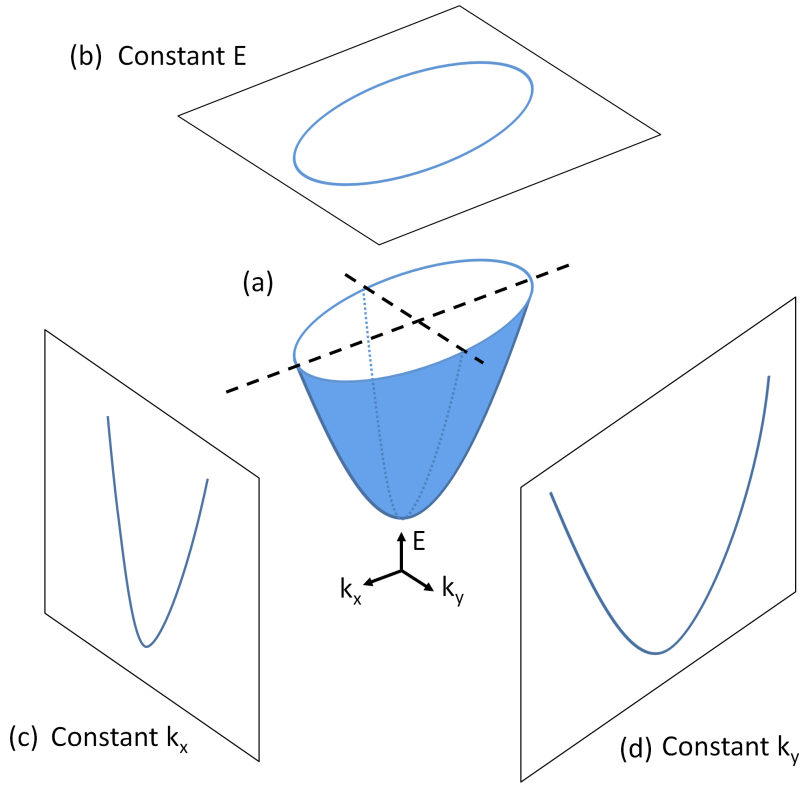

Figure 2.7: (a) Band dispersion along k_x and k_y for a parabolic band. (b) Constant energy cut of a parabollic band. Band dispersion as a function of (c) k_x and (d) k_y.

A wide range of emission angles can be explored by changing the angular position of the sample with respect to the semi-spherical analyzer. It is therefore possible to explore large regions of the k-space (the k_x and k_y parallel components) vs. binding energy (fig. 2.7a). This type of construction allows to visualize and follow the band structure along different crystallographic orientations. Constant energy cuts of the

whole electronic structure allow to visualize the electronic bands at a given binding energy as a function of the k_x and k_y components (fig. 2.7b). When the binding energy is equal to zero, this particular cut is called the Fermi surface. It is also possible to retrieve the E(k) dispersion of the bands in any in-plane direction (fig. 2.7c and d).

At the Cassiopée beamline in Soleil Synchrotron, the photon energy is selected by two undulators that cover a range between 8-1500 eV. The photon energy is then monochromatized in a modified SX700 monochromator that combines a variable groove depth grating, a plane mirror and exit slits. The spot size of the photon beam at the samples is of some tens of microns. The ARPES end station that I have used, operates with a Scienta R4000 semi-spherical analyzer with maximum angular range of the acceptance slit of $\Delta\theta = \pm 15°$. The sample temperature can be stabilized between Liquid-He and RT thanks to a cryogenic manipulator constructed at the Laboratoire de Physique des Solides.

Chapter 3

Electronic structure tailoring on Ir(332)

This chapter is dedicated to the modification of the electronic properties of graphene by nanostructuring of the substrate. We will induce the structuration in graphene by using a vicinal surface that can promote graphene growth. Ir(332) is a stable vicinal surface with small terraces of 1.25 nm. The growth study on Ir(332) was planned before the first publication on the topic appeared [114]. The work done by Srut et al. was then published at the time where our experimental work began, therefore we used these reported results on Ir(332), along with the well-known growth of graphene on Ir(111), as a basis and comparison point for the later growth on Ir(332) in our chamber. I have applied two different growth methods, namely temperature programmed growth and chemical vapor deposition. Growth by those techniques on Ir(332) induces a periodic potential on graphene, as seen by the presence of gaps in the band structure probed by ARPES. After applying the Dirac-hamiltonian model, we determined that a surface potential is induced in graphene by the nanostructuring. We finally modified the periodic potential by Cu intercalation, obtaining an array of n- and p-doped nanoribbons on a continuous layer.

3.1 Growth and structure of Gr on Ir(332)

Several noble metals have been used as substrates for graphene growth due to their catalytic properties, which contribute to the decomposition of hydrocarbons. In particular, graphene growth can be achieved on Ir(111). Here, graphene grows decoupled from the

substrate (Gr-Ir distance is 3.4-3.8 Å, which is larger than the interlayer distance in graphite). In this way, there is a low interaction between graphene and Ir, allowing a study of graphene's electronic properties in a quasi-free standing regime [115, 116]. Fig. 3.1a-b shows a LEED pattern of graphene on Ir(111). There is a domain aligned with the substrate (a zero rotation, that we will name R0), additionally, other domains appear where graphene has a twisted angle with respect to iridium. Both the quantity and quality of the graphene depends on the particular growth and conditions, and several graphene rotational domains with respect to the substrate can coexist [117–121]. The STM images on fig. 3.1c-d show three different coexisting domains that extend even through step edges. Domains are separated by defective boundaries where carbon atoms form heptagons and pentagons or wrinkles.

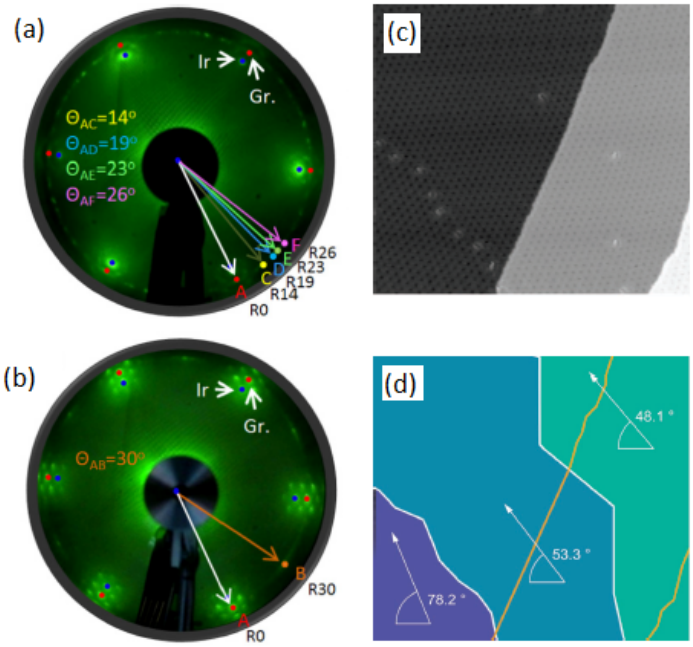

Figure 3.1: (a)-(b) LEED patterns of graphene growth on Ir(111) at different growth temperatures. (a) shows a wide variety of rotational domains with respect to iridium, named after their angle of rotation, while (b) presents only two rotational domains, namely R0 and R30 [118]. (c) STM image of a Gr/Ir(111) surface where three rotational domains coexist in a continuous graphene layer (108 nm × 108 nm). (d) Sketch where the three rotational domains are identified. The white borders represent the boundary of each domain, that extends across the terrace edges (yellow lines) [121].

The growth of graphene on a vicinal surface of Ir(111) could be similar, although we would be interested in searching for growth conditions that promote an array of discontinuous graphene nanoribbons, as shown on fig. 3.2a. An array of ribbons allows a simultaneous study by STM and ARPES. In such an array, each nanoribbon experiences

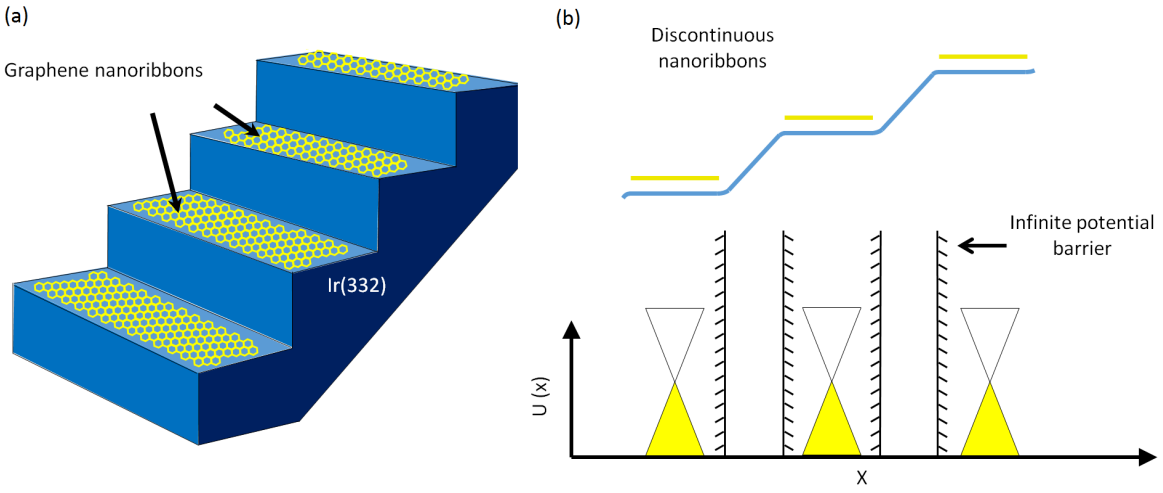

Figure 3.2: (a) Scheme of the ideal array of discontinuous graphene nanoribbons on top of the terraces of Ir(332). (b) Model for the electronic linear dispersion of graphene nanoribbons separated by a potential barrier.

a potential barrier on both edges acting as a potential well for electrons in graphene (fig 3.2b). The effects of such a potential should have a direct impact on the electronic band structure of graphene.

We have used a vicinal surface as a template for graphene growth with two different methods: Temperature Programmed Growth (TPG) and Chemical Vapor Deposition (CVD), which can form single domains on metallic surfaces [116–119, 121–130]. These growth results were obtained at the Institut Jean Lamour in Nancy, in collaboration with M. Sicot and D. Malterre. In the following I detail the growth studies to determine the optimal preparation that was then extensively studied by ARPES at Soleil Synchrotron.

3.1.1 Ir (332) substrate preparation

The pristine Ir(332) surface consists of Ir(111) terraces of 1.25 nm that extend along the $[10\bar{1}]$ direction and are periodic in the $[1\bar{2}1]$ direction (fig. 3.3a). To clean the Ir(332) crystal, cycles of sputtering followed by annealing have been performed. An intermediate annealing under oxygen atmosphere can be performed to eliminate the carbon impurities that diffuse to the surface as a product of the annealing [118, 123]. We found however, that a high quality surface could be achieved without this intermediate step. The sputtering was performed at RT with a 1keV Ar^+ flux at a 2×10^{-6}mbar pressure. The sputtering time was 10 min at three different positions (center and edges of the

sample). A subsequent annealing by electron bombardment was performed at 650°C for 15 min and then slowly cooled down for 35 min to RT at a rate of 20 ±1 °C/min. After repeated cycles of sputtering/annealing, LEED patterns were checked until obtaining a clean surface, as shown on fig. 3.3b. The clean surface is characterized by almost no background intensity and defined Ir spots. The surface is composed of two types of Ir spots: the $(1x1)$ spots of Ir due to the hexagonal iridium periodicity (marked in red), and a splitting of these spots due to the periodic nature of the vicinal surface along the $[1\bar{2}1]$ periodic direction (G_{per} marked in blue). Taking the distance between the Ir $(1x1)$ spots as a reference, the terrace size calculated by LEED is $L = 2\pi/G_{per} = 1.8 \pm 0.2$ nm.

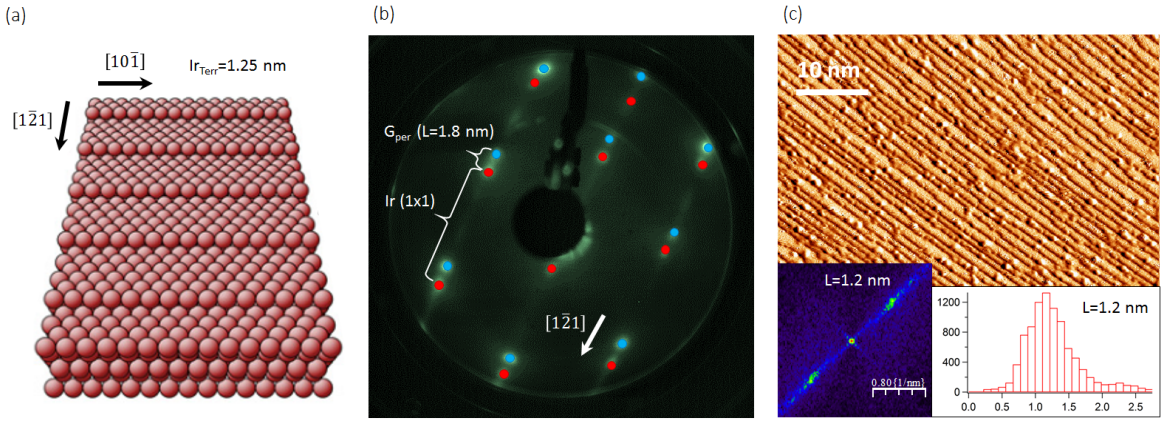

Figure 3.3: Clean Ir(332) structure. (a) Sketch of the pristine Ir(332) surface, with 1.25 nm terraces along the $[10\bar{1}]$ and periodic along the $[1\bar{2}1]$ direction [114]. (b) LEED pattern of Ir(332) at 148 eV showing the splitting of the Ir (1x1) spots due to the periodicity of the terraces. The difference between the red and blue spots gives a terrace size $L = 1.8 \pm 0.2$ nm along the $[1\bar{2}1]$ direction. (c) STM image on the clean Ir(332) vicinal surface [1 V, 0.5 nA]. Insets shows two methods to obtain the terrace width: A general estimate through a Fast Fourier Transform of the STM image ($L = 1.2 \pm 0.2$ nm) and the terrace width distribution of the STM image ($L = 1.2 \pm 0.3$ nm).

As a second quality check, the surface was later studied by STM (fig. 3.3c). At first glance, we observe that the terraces have an homogeneous distribution and straight edges. On the other hand, some present particles appear due to impurities, as the image was taken at RT [131]. To obtain the terrace size from the STM images, two methods were employed: the Fast Fourier Transform (FFT) of STM images and a direct analysis of the Terrace Width Distribution (TWD). After the FFT was obtained, a profile was traced through the central spot and the two secondary maxima. The terrace size was obtained by transforming the G distance in the reciprocal space into its corresponding distance in the real space ($L = 2\pi/G$). With this method, the recovered periodicity is $L = 1.2 \pm 0.2$ nm. For the TWD method, the STM image was analyzed pixel-by-pixel

perpendicularly to the steps in order to detect step edges and determine the terrace size with the histogram of the terrace widths. This method gives a distribution where $L = 1.2 \pm 0.3$ nm. The FFT image and the histogram obtained by TWD are presented on the inset in fig. 3.3c. The difference between the values obtained by LEED and STM can be explained by the local nature of STM, where images are typically of surfaces $\sim$ 3000 nm^2, while LEED averages over ~ 1 mm^2 with a coherence of ~ 100 nm^2.

3.1.2 Temperature programmed growth on Ir(332)

Temperature Programmed Growth (TPG)on Ir(111) has already alowed the growth of separate graphene flakes, being thus promising for our goal [119,125,129,132]. The TPG technique consists of depositing a hydrocarbon onto the catalyst surface at RT. Once the deposition is achieved, the surface is heated above 600°C to promote the decomposition of the hydrocarbon. The hydrogen is evacuated through the UHV pumping system, while the remaining carbon is mobile at the surface of the metal. The energy provided by the temperature is used to nucleate, grow and/or merge islands of graphene. Since the carbon diffusion towards the Ir bulk is insignificant [133], by annealing to the system, only graphene formation is promoted.

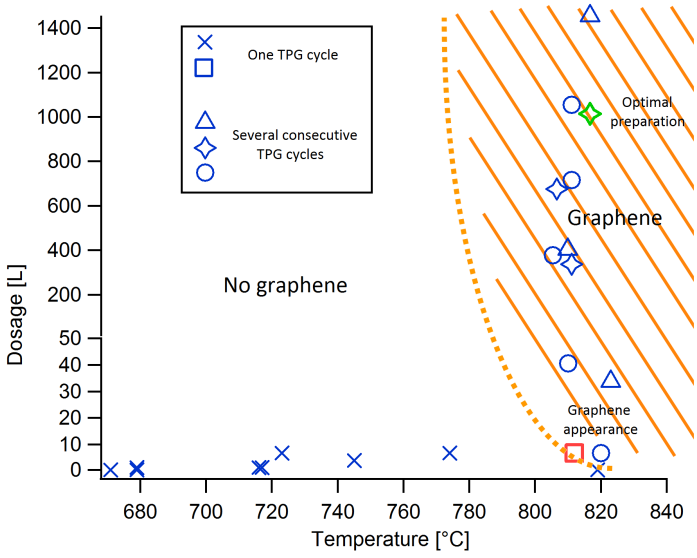

Figure 3.4: Dosage vs. substrate annealing temperature for different TPG preparations. The orange line indicates the dosages and temperatures where graphene appears. The cross and square symbols represent samples obtained in a single TPG cycle. The triangle, diamond and circle represent series of consecutive TPG cycles. The red square marks the first appearance of graphene, while the green diamond marks the optimal preparation.

As graphene forms a layer on top of the metal, the surface of the metal is covered when the first monolayer is complete, preventing any further catalytic interaction between the hydrocarbon and the metallic substrate. The formation of graphene is thus a self-limiting process to a single layer. If the substrate is cooled afterwards, a mono-domain island is favored in graphene. In principle, several TPG cycles are necessary to reach the full coverage of the surface [132], although a complete monolayer is not necessary for a nanoribbon array growth.

In our experiment, the preferred hydrocarbon for TPG is ethylene (C_2H_4), as it is the simplest, most common gas, and our collaborators at the Institut Jean Lamour in Nancy have the expertise of growing graphene with it. Its deposition is achieved with a leak valve. Both the partial pressure ($P_{C_2H_4}$) and the exposure time (t_{exp}) are key parameters. The dosage is measured in Langmuir [L], corresponding to the equivalent exposure of $10^{-6} torr$ for one second. The Ir(332) surface was later annealed to different T_{tpg} temperatures to stimulate the carbon-hydrogen bond breaking and the graphene formation. Finally, the surface is cooled down to RT at a controlled rate of 22 $\pm$1 °C/min. The parameters for $P_{C_2H_4}$ and t_{exp} vary from 1×10^{-8} to 2.5×10^{-6} mbar and from 1 to 60 minutes respectively. The details of all the preparations are presented in Table A.1 on the Appendix.

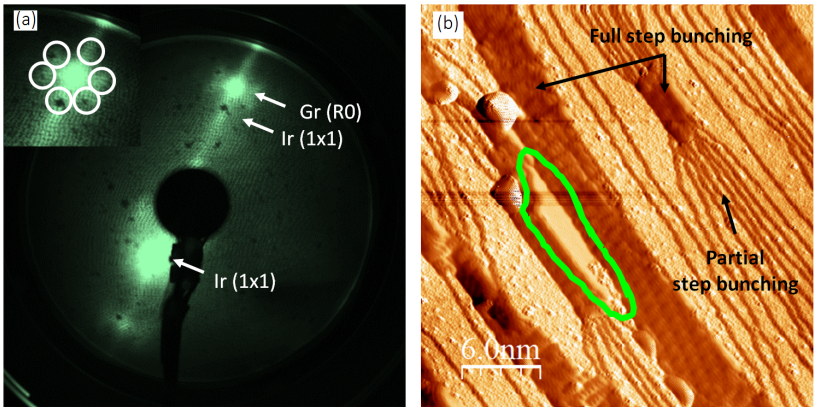

Figure 3.5: Characterization of the initial graphene growth obtained after one TPG cycle at an effective dosage of 6.75 $\pm$0.14 L. (a) LEED with an incoming electron beam of 34 eV showing the $(1x1)$ spots of Ir and R0 graphene spots. Inset shows the moiré spots around the R0 spot of graphene. (b) STM image showing the first stages of graphene growth on Ir(332) [1 V, 1.1 nA]. The pristine Ir(111) steps begin to coalesce and form step bunching in various degrees of completion (partial or full), shown by the arrows. Graphene appears on the wider terraces associated to full step bunching.

With the objective of growing individual nanoribbons on the terraces of Ir(332), we started with an exposure ten times lower than the optimal for fully covering Ir(111).

The systematic study of graphene formation by TPG as a function of the annealing temperature T_{tpg} and the exposure is presented in fig. 3.4. The initial optimization of the growth consisted of performing one TPG cycle at various exposures and temperatures until a graphene signal appeared in LEED (red square). The appearance of graphene allowed to fix the TPG temperature at $\sim 800°C$, which falls in the range for the growth on Ir(111). Once the growth temperature was set, series of TPG cycles were performed without sample cleaning to increase the coverage of the surface by accumulation until reaching the optimal preparation (green star). In fig. 3.4, the circle, triangle and star represent three different samples grown by several consecutive TPG cycles after the lowest exposure ones. Every appearance of the same symbol indicates an accumulated TPG cycle on the same sample. LEED was performed on every sample, so we can identify the growth conditions leading to graphene formation (orange dotted line).

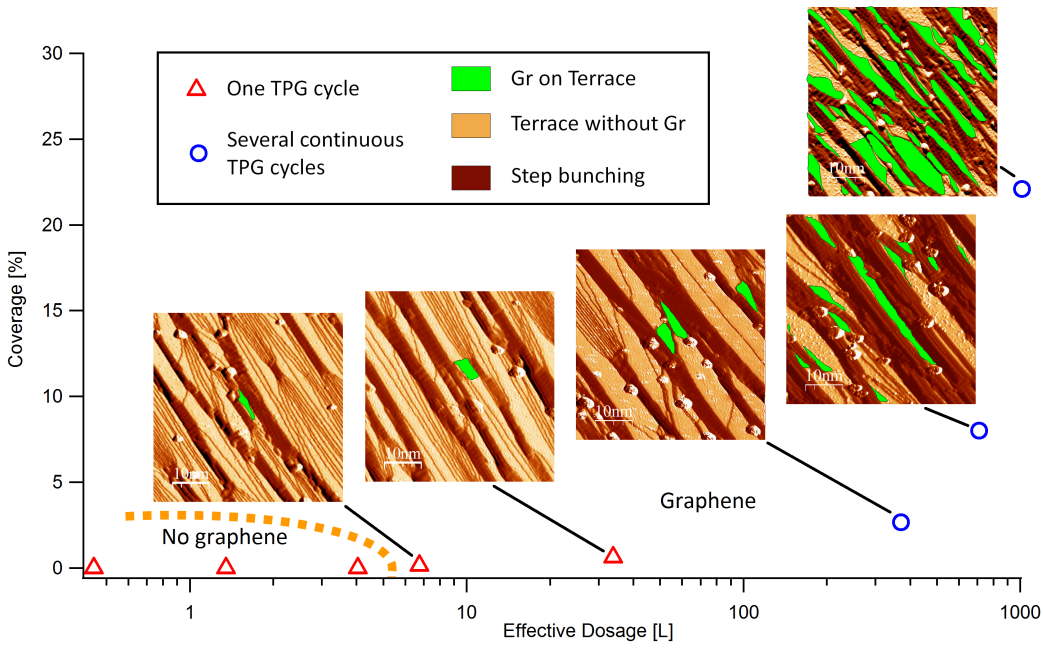

Figure 3.6: Coverage vs. effective dosage for different TPG preparations. The orange line shows the boundary of graphene formation. Red triangles represent samples obtained with one TPG cycle while blue circles were obtained after two or more cycles. Insets show STM images of the surface as the coverage increases (left to right:[1 V, 1.1 nA],[1 V, 0.5 nA], [1 V, 0.6 nA], [1 V, 0.6 nA], [1 V, 0.5 nA]).

LEED was performed after TPG cycles to roughly characterize the sample quality. Fig. 3.5 corresponds to the initial stages of graphene growth (red square in fig. 3.4) at 6.75 L and 812°C. The LEED shows that the surface has been modified with respect to the clean Ir(332) surface. The splitting of the $(1x1)$ spots characteristic of the clean Ir(332) suface dissapear, indicating that the regular periodicity of the steps has been

lost. Also, new spots appear associated to graphene which is aligned with respect to the iridium substrate (R0 rotation). Six additional features appear around the graphene spot (inset) resulting from the moiré pattern due to the different lattice parameters of graphene and iridium, even if they have the same crystallographic orientation.

Although many features of the surface were understood thanks to LEED, it does not provide information about the precise morphology of the surface. Hence we performed STM to investigate the initial stages of graphene growth (fig. 3.5b). It can be observed that a step-bunching process takes place. The pristine (111) steps coalesce and form step bunching in various degrees of completion (partial or full), shown by the arrows on fig. 3.5b. Once wider terraces are formed due to the full step bunching, the first patches of graphene appear on the (111) steps. The step bunching suppresses the initial periodicity of the Ir(332) surface, explaining the loss of the splitting on the LEED spots when graphene is grown. Additionally, the round-like islands are most likely carbides, which have been observed before by Šrut et al. [114].

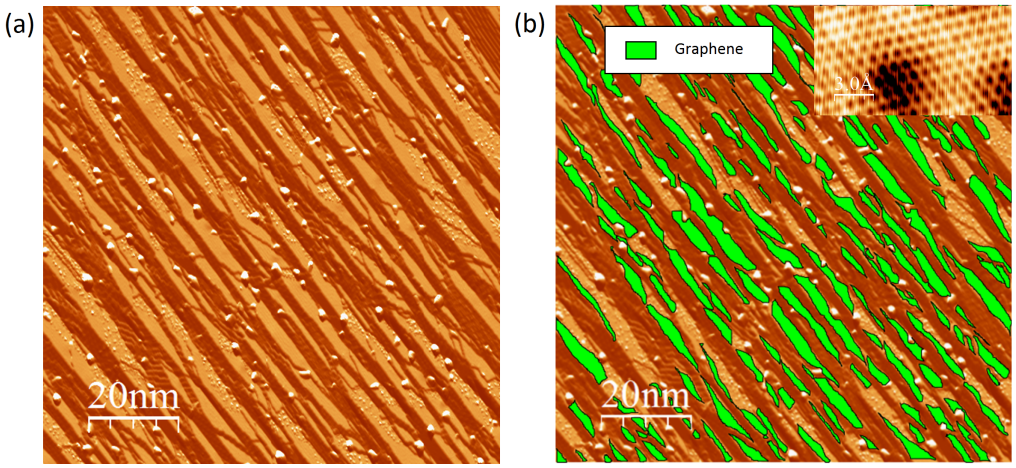

Figure 3.7: Characterization of the optimal preparation. (a) STM image showing the Gr/Ir(332) sample obtained after three TPG cycles with an effective dosage of 1014 ±1 L [1 V, 0.6 nA]. (b) Green areas represent the graphene areas in (a). These areas do not extend across the whole length of the terrace. Inset shows atomic resolution of the graphene R0 domain on a terrace.

When increasing the effective dosage, the surface is progressively covered, as shown in fig. 3.6, which corresponds mainly to the vertical points in fig. 3.4. In fig. 3.6, the red triangles correspond to one TPG cycle, while the blue circles correspond to two or more cycles. Graphene is first seen at dosages around 7 L, as shown by the orange line. Higher graphene coverage is obtained on several TPG cycles. The LEED intensity does not change as the coverage is increased, so the quantification of the coverage is based

on STM images at large scale. Besides showing the increase of graphene, STM images also show the stabilization of large terraces (orange) and step bunching areas (brown) in an ordered manner. The optimal preparation is presented in fig. 3.7. The treated STM image is shown in panel (a). Both the terrace and the step bunching arrays are developed. The average terrace width is now 4.4 ±1.4 nm as calculated from the FFT of the STM images. Graphene areas on the (111) steps are highlighted in green, as shown on fig. 3.7b. The inset shows the atomic resolution of the graphene network, which is rotated 0° with respect to Ir. Graphene is identified by STS, as shown in fig. 3.8. The spectrum on fig. 3.8b performed on the (111) terrace (green point in panel (a)), is very similar to the one on Gr/Ir(111). In particular, it reveals three features specific to the Gr/Ir(111) system [127, 128, 134], as shown in panel (c) [134]. The first feature associated to the S1 surface state has a maxima between −0.25 V and −0.5 V (F_1). The second feature is associated to unoccupied states and has a maxima around +0.6 V (F_2). The third feature is the dirac point (E_D^{Ir}) around +0.25 V, comparable the +0.2 V in panel (c), indicating a p-doping on the electronic structure of graphene on the terrace. The doping is slightly different to the one on Gr/Ir(111) (+0.2 eV),

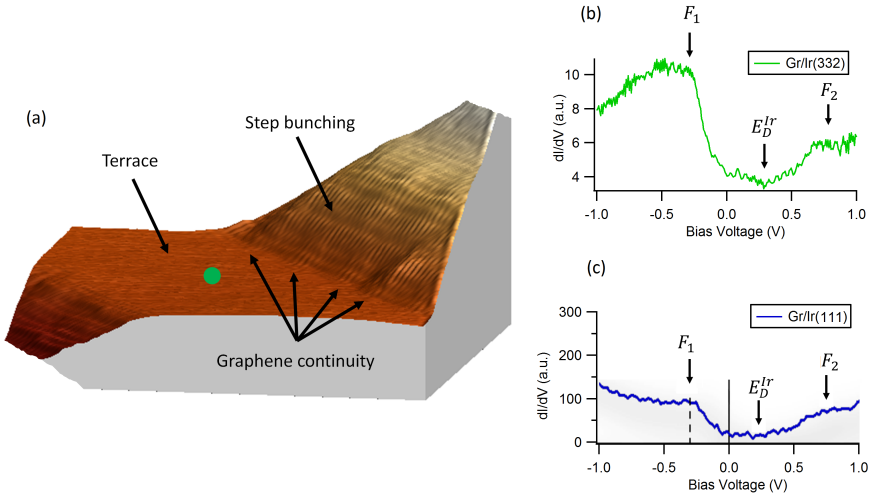

Figure 3.8: Continuity of graphene between step bunching and terraces. (a) 3D STM image [10 mV, 36 nA] of a boundary between a flat terrace and two step bunching areas. The continuity of the graphene network is indicated by arrows. The green point shows where the spectroscopy data in (b) was taken, while (c) is extracted from a previous experiment on Gr/Ir(111) performed in the same preparation chamber [134]. (b) STS shows three features: F_1 between −0.25 V and −0.5 V (associated to surface state S1), F_2 around +0.6 V (unoccupied states) and the dirac point (E_D^{Ir}) around +0.25 V, indicating p-doping. (c) STS on Gr/Ir(111) [134] showing the same F1, F2 and E_D^{Ir} features than Gr/Ir(332).

but it is not surprising, as experimental and theoretical reported values for the p-doping

vary from 0.1 V to 0.34 V [122,126,130,132,135,136]. As shown by fig. 3.7b, graphene does not occupy the full terrace length, which can only be achieved by approaching full coverage, but it is not suitable for discontinuous graphene nanoribbons growth.

It seems difficult to obtain discontinuous graphene on the (111) terraces, as STM reveals that graphene extends from the step-bunching to the terraces in a continuous way. Fig. 3.8a shows the continuity thanks to the atomic resolution. Our interpretation is that the observed continuity is due to the growth mechanism, where the steps of the step-bunching act as nucleation centers for graphene growth that then extends towards the (111) terraces. Fig. 3.9a shows an intermediate stage of graphene growth where the step bunching areas (orange) fully display a periodicity similar to the moiré of graphene. At the same time, only a fraction of the terraces are covered by overgrown graphene (green), while the majority of the (111) terraces are bare iridium (brown). It seems then possible to obtain a discontinuous network of graphene nanoribbons located at the step bunching regions in this stage of growth. Fig. 3.9b shows our model for this intermediate stage: Graphene is present on the step bunching area and slightly overgrown on the terrace, producing a network of discontinuous graphene nanoribbons. This spatial discontinuity could be seen by graphene as an infinite potential barrier at both sides of each nanoribbon, which is an interesting perspective to be explored in the future.

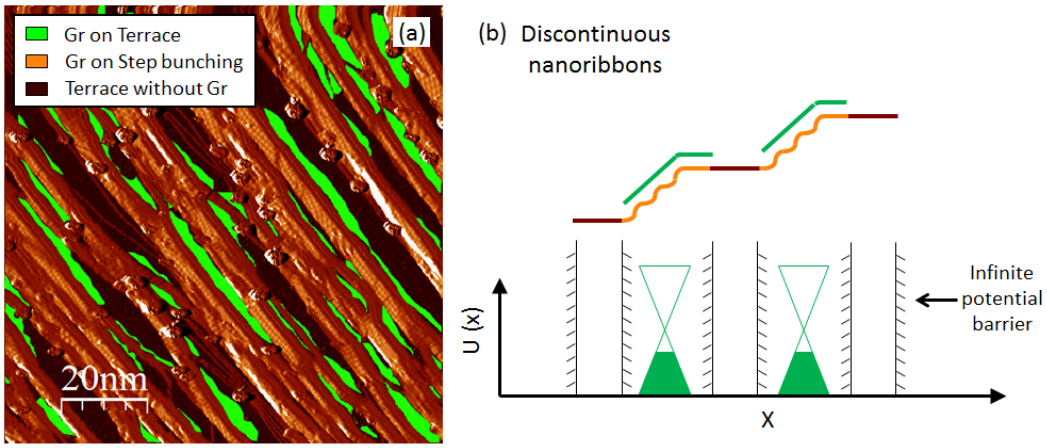

Figure 3.9: (a) STM image of an intermediate stage of graphene growth after three TPG cycles with an effective dosage of 1455 ±15 L [1 V, 0.6 nA]. Step bunching areas (orange) fully display a periodicity similar to the moiré of graphene. Overgrown graphene (green), occupies a fraction of the (111) terraces, while the majority of the terraces are bare iridium (brown). (b) Model for the intermediate stage: Graphene is present on the step bunching area and slightly overgrown on the (111) terrace, producing a network of discontinuous graphene nanoribbons. The spatial discontinuity is seen by graphene as an infinite potential barrier at both sides of each nanoribbon.

3.1.3 Chemical vapor deposition for Ir(332)

The Chemical Vapor Deposition technique (CVD) consists of exposing a hot catalytic surface to a hydrocarbon species. Contrary to the TPG technique, the dissociation of the molecule and graphene formation occur in a single step. The thermal energy promotes the nucleation, growth and/or merging of islands. Depending on the cooling dynamics, graphene can form mono- or multi- rotational domains or even wrinkles [117–121, 126]. As TPG, CVD is a self-limiting process, so once a graphene monolayer is formed, no active sites are available to promote further graphene growth [129].

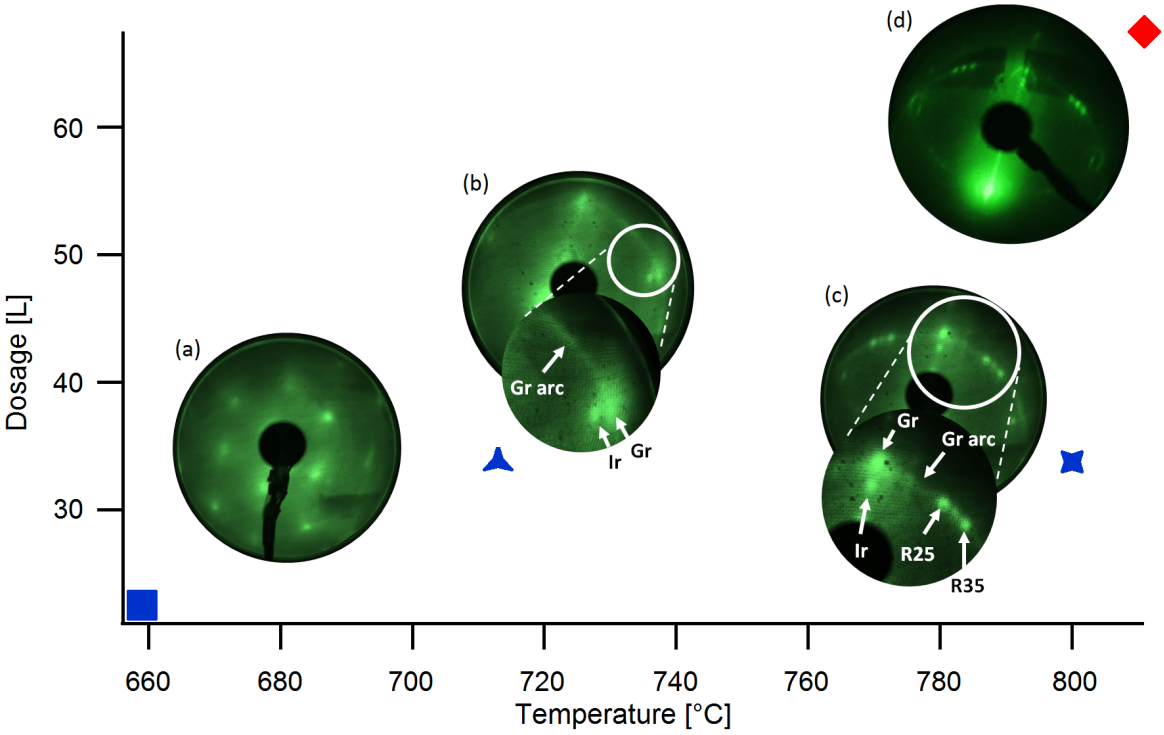

Figure 3.10: Dosage vs. temperature for different CVD preparations. Blue symbols show the evolution of the preparations, while the red rhombus shows the optimal preparation. (a)-(d) LEED of the blue square (232 eV beam energy), triangle (66 eV beam energy), star (66 eV beam energy) and red rhombus (66 eV beam energy) respectively. (a) Ir $(1x1)$ spots and a diffuse background are present, but there is no graphene signal. (b) R0 graphene spots are visible along with a diffuse arc representative of multi-domain graphene. (c) R0, R25 and R35 graphene spot are visible, in addition to a graphene arc. (d) LEED of the optimal preparation, further analyzed in fig. 3.11.

For CVD preparation of graphene on Ir(332), we chose ethylene (C_2H_4). The substrate is annealed to a given temperature (T_{cvd}) and a gas partial pressure of ethylene ($P_{C_2H_4}$) is inserted through a leak valve. The surface is kept hot for an active time (t_{act}), then cooled down to room temperature at a controlled rate of 60 $\pm$1 °C/min. Contrary

to TPG, LEED became a tool to explore the evolution of the graphene structure, since the coverage is inherently larger by CVD. This is the result of dissociation and growth occurring continuously at the hot surface. We thus optimized the preparation by maximizing the intensity and sharpness of the graphene LEED spots by varying the dosage and the temperature. We then performed STM on the optimal preparation. Therefore, the quality of the sample can be first assessed by LEED and then analyzed by STM once the optimal LEED pattern has been reached.

Fig. 3.10 shows the LEEDs of the different preparations as a function of the dosage and the annealing temperature. The details of all the preparations are presented in Table A.2 on the Appendix. Our first preparation was chosen to be about half of the dosage for CVD on Ir(111) and 150 °C below the typical temperature [131]. This is indicated by the blue square on fig. 3.10 and corresponds to $T_{cvd} = 659°C$ and a dosage of 22.5 ± 0.1 L. Panel (a) shows a LEED with an incoming electron beam of 232 eV with characteristic Ir $(1x1)$ spots and a diffuse background, but no traces of graphene. Thus, we changed the temperature, as it is the key parameter to induce the molecular dissociation and hence the graphene formation. The second preparation was performed at a slightly higher temperature of $T_{cvd} = 713°C$ and a dosage of 34 ± 2 L (fig. 3.10b). An emerging structure is appreciated around the Ir(111) spots due to graphene at 66 eV.

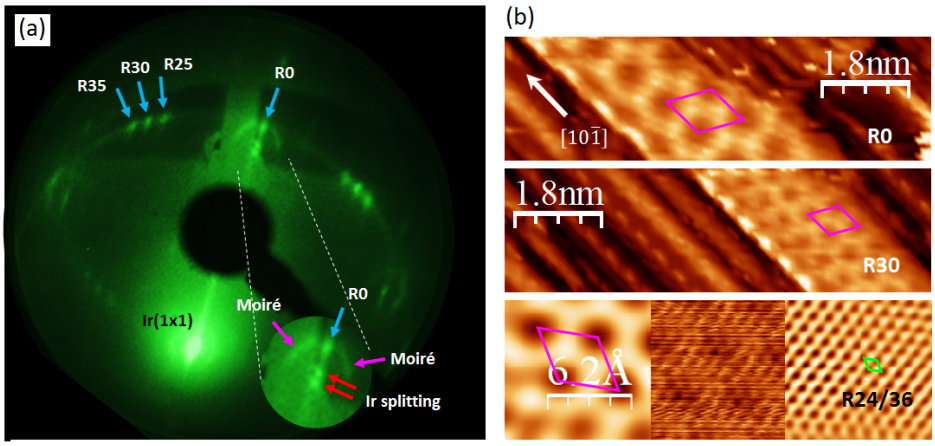

Figure 3.11: Characterization of the optimal CVD sample (810 °C and 67.5 ±0.1 L). (a) LEED image at an incoming electron beam of 63 eV. Blue/pink/red arrows represent graphene, moiré and Ir spots respectively. Inset shows the Ir splitting (due to a superperiodic structure) and the moiré. (b) STM images of the graphene domains in (a). Upper and middle panel show the R0 and R30 domains [1 V, 2 nA]. The pink rhombus indicate the unit cells of the graphene moiré aligned with the $\langle 10\bar{1} \rangle$ direction. The bottom panel is composed image for the R25/R35 domain. Center: STM image where both the graphene network and the moiré pattern are present [5 mV, 29 nA]. Left: Filtered image with moiré unit cell in pink. Right: Filtered image with graphene unit cell in green.

Graphene spots are visible now aligned with the Ir(111) spots (R0 rotation). A diffuse arc is also visible, due to multi-domain graphene. Upon increasing the temperature to 800 °C while keeping the dosage at 34 ± 2 L (fig. 3.10c), the LEED features become sharper, and we distinguish the R0 spot, plus two domains around 25° and 35° (further called R25 and R35). The faint intensity from the multi-domain graphene arc is still present. Finally, the temperature was set to 800 °C, while increasing the dosage to the optimum value of 67.5 ± 0.1 L, in agreement with that for Ir(111) (fig. 3.10d). The details of the LEED in (d) are given in fig. 3.11. The LEED of the optimal preparation is shown in fig. 3.11a. There are four different kinds of graphene LEED spots associated to different rotational domains. The first kind of spots have the same orientation than Ir(111) spots (0° rotation between the layers or R0) shown by the white arrow on fig. 3.11a and has an armchair edge termination. The other three are extra graphene spots corresponding to 25°, 30° and 35°, shown by blue arrows on fig. 3.11a as R25, R30 and R35). Since the R25 and R35 are two equivalent domains 5° around R30, they will be referenced as R25/R35. The R25/R35 domain has zigzag edge termination, while the R30 is chiral quasi-zigzag. Fig. 3.11b shows the coexistence of the four different domains observed by STM on the terraces: R0, R30 and R25/R35. Although a moiré pattern is observed in STM for all the domains (pink rhombus in fig. 3.11b), on the LEED image, there is additional intensity forming a moiré hexagonal pattern only around the R0 graphene spots, as marked by the pink arrows on the inset on fig. 3.11a. Such a behavior can be understood by analyzing the intensities of the different spots. The R0 domain has $\sim$ 60 % higher intensity than the other three domains, which accounts to higher coverage on the sample and therefore a higher intensity of the moiré signal compared to the other domains.

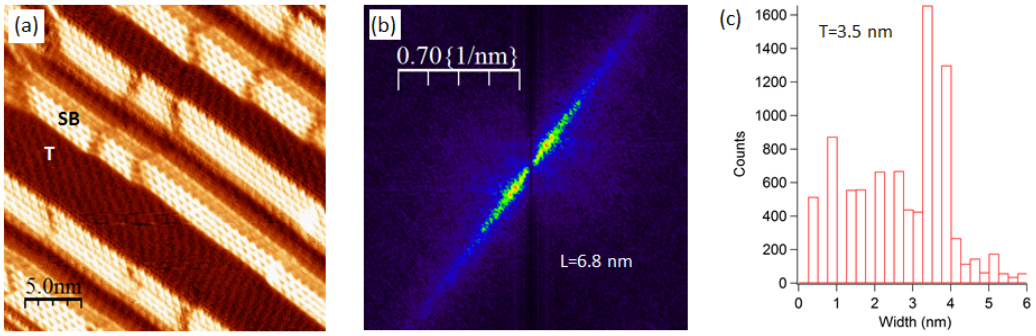

Figure 3.12: (a) STM image of the optimal CVD sample [0.9 V, 0.5 nA]. Terrace (T) and Step bunching (SB) areas indicated on the surface. (b) FFT of (a) resulting in a superperiodicity of 6.8 ± 0.6 nm. (c) Terrace width distribution histogram of the surface resulting in a terrace size of 3.5 ± 0.5 nm.

LEED also reports on the structural periodicity of the substrate. The Ir spot is splitted, as indicated by the red arrows in fig. 3.11a due to a superperiodicity on the substrate $L = 7.1 \pm 1.5$ nm. As seen in fig. 3.12, the surface is composed of terraces and step bunching areas (marked by the legends T and SB) giving rise to the superperiodicity obtained by LEED. The size of the superperiodicity calculated by FFT of this STM image is $L = 6.8 \pm 0.6$ nm, as shown by fig. 3.12b. The terrace width distribution method performs a pixel-by-pixel analysis perpendicularly to the steps on the STM images, in order to detect the step edges and determine the terrace size. The obtained terrace size is $T = 3.5 \pm 0.5$ nm (fig. 3.12c), roughly half of that obtained by LEED and FFT. Since the superperiodicity is comprised of the terrace + step-bunching and the calculated terrace size is half of the superperiodicity size, this would result in the step bunching size being roughly equal to the step bunching size.

STM also shows that graphene completely covers the Ir(332), as observed by the continuous moiré pattern on fig. 3.12a. Despite this continuity, the nicely periodic substrate (with much higher quality than that obtained by TPG), induces a periodic potential that may have an impact on the electronic properties of graphene and open band gaps, as is the case for other nanostructured systems [112, 137–139]. The modification of the properties depends on the potential strength at the step edges.

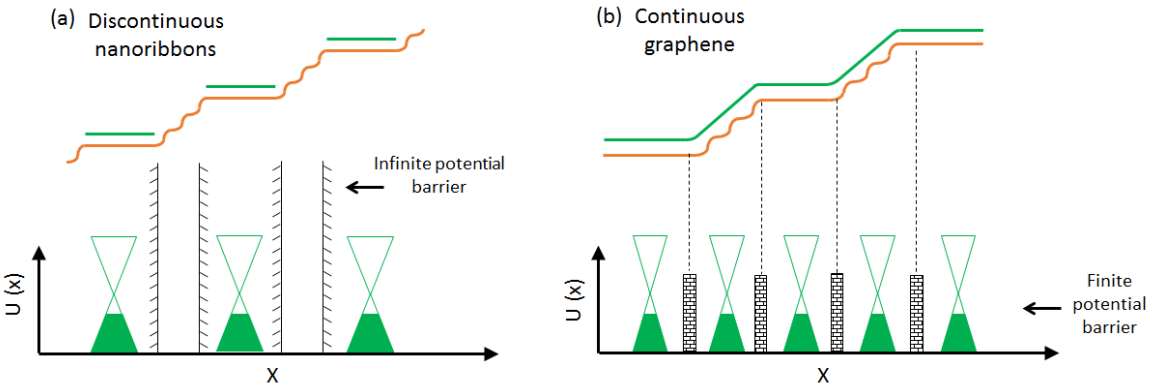

Figure 3.13: (a) Model for the infinite potential barrier between discontinuous graphene nanoribbons on the Ir(332) surface. (b) Model for the finite potential barrier created by the step bunching on a continuous carpet of graphene.

The effect can change from total confinement in discontinuous graphene nanoribbons due to infinite potential barriers (fig.3.13a), or to minigap opening in the case of continuous graphene feeling a periodic structure with finite potential barriers at the boundaries between terraces and step bunching regions (fig.3.13b). ARPES allows to

quantify the potential strength and its effects on the electronic band structure, as we will see in the next section.

3.1.4 Cu intercalation on Gr/Ir(332)

A way to further control the potential barrier at the step edges is by decorating the steps of the substrate with adatoms. It is necessary to intercalate atoms below the graphene layer. Intercalation of metals on graphene has been a successful way of investigating the metal-graphene relationship and the changes in commensurability [136,140,141], charge transfer [130, 136, 142, 143], electronic band structure [130, 136, 140, 144, 145], phonon modes [145, 146], spin-polarized effects [141], among others. In the framework of the modification of the surface potential to obtain higher confinement, we consider the intercalation of Cu on Gr/Ir(332) by following the procedure developed for Gr/Ir(111) [131].

Intercalation method

Copper adatoms can be intercalated on graphene on Ir(111) [131]. Fig. 3.14 shows the intercalation as a function of the Cu coverage. The initial Gr/Ir(111) surface is represented in stage 0 (fig. 3.14a). At stage 1, Cu intercalates in preferential sites such as the step edges and occasionally in the terraces. Further intercalation (stage 2) results in the growth of the already intercalated sites. When approaching a complete Cu monolayer below the graphene, Cu continues to be intercalated homogeneously below the graphene and also starts to form islands on top of graphene, as presented in stage 3. Panels (b)(c) and (d) show the STM images of stages 1, 2 and 3 respectively, where the insets highlight in yellow the areas where the moiré structure indicates that Cu has been intercalated.

By taking into account this mechanism, we expect that Cu decorates easily the step edges of a vicinal surface, possibly increasing the potential felt by graphene there. We have performed two different intercalations of 0.45 ML and 0.9 ML of Cu on the optimal Gr/Ir(332) obtained by CVD (fig. 3.12). The intercalation is achieved by Cu evaporation from a Knudsen cell at 850°C for 45 min. (in the case of 0.45 ML coverage). followed by an annealing at 500°C for 45 min at a base pressure $\sim 1-2\times10^{-9}$ mbar at a rate of 0.1 Å/min. These parameters are the usual ones for Gr/Ir(111) on the same preparation chamber [131]. The coverage of 0.9 ML of Cu is reached by adding 0.45 ML of Cu on the previously intercalated sample. After each intercalation, the sample

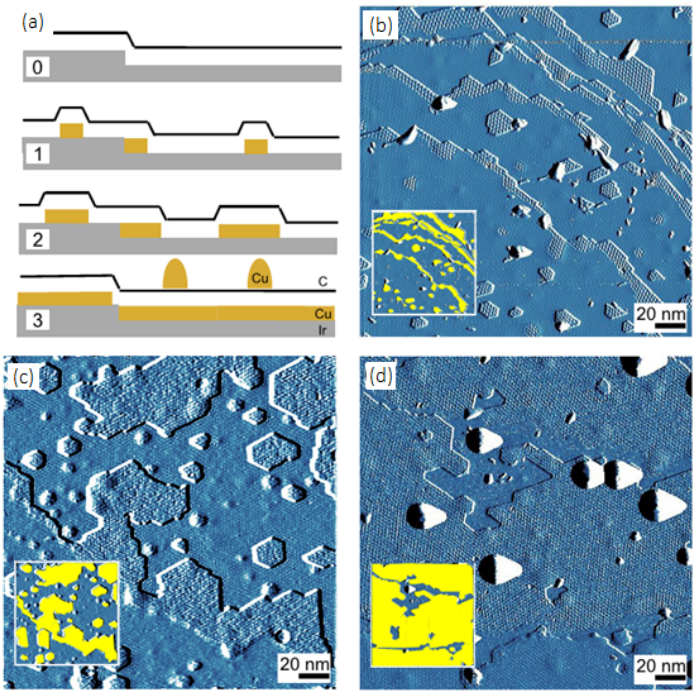

Figure 3.14: (a) Mechanism of Cu intercalation between the Gr and Ir(111) surface. Step 0 - Initial Gr/Ir(111) surface. Step 1 - Intercalation of Cu begins at step edges and terraces. Step 2 - Cu clusters grow on nucleated sites. Step 3 - Growth continues until monolayer coverage. Then, Cu in excess forms nanoislands on the Gr surface. (b)(c)(d) STM images corresponding to step 1 (0.12 ML), 2 (0.31 ML) and 3 (0.86 ML) respectively. Insets show the same STM image where it is indicated in yellow the regions where the moiré demonstrates that Cu has been intercalated [131].

is cooled down to RT and STM/STS is performed to observe the changes in the atomic and electronic structure of the surface.

Near monolayer intercalation on Gr/Ir(332)

The intercalation of 0.9 ML is presented in fig. 3.15. The surface before intercalation is shown on panel (a) as a reference, while the intercalated surface is shown on panel (b). The atomically resolved STM image shows the R0 rotation of graphene with respect to iridium (inset in fig. 3.15b). The intercalation of Cu is visible through the enhancement of the moiré on the terraces, as shown by the blue rhombus unit cell. The moiré is not visible on the step bunching, probably because it cannot be developed completely as the width of the step bunching is slightly below the size of the unit cell (2.52 nm).

However, even if the enhanced moiré is not developed on the step bunching, Cu is also intercalated there, as indicated by scanning tunneling spectroscopy (fig. 3.15c). Both STS spectra on the terraces and on the step bunching are very similar, with

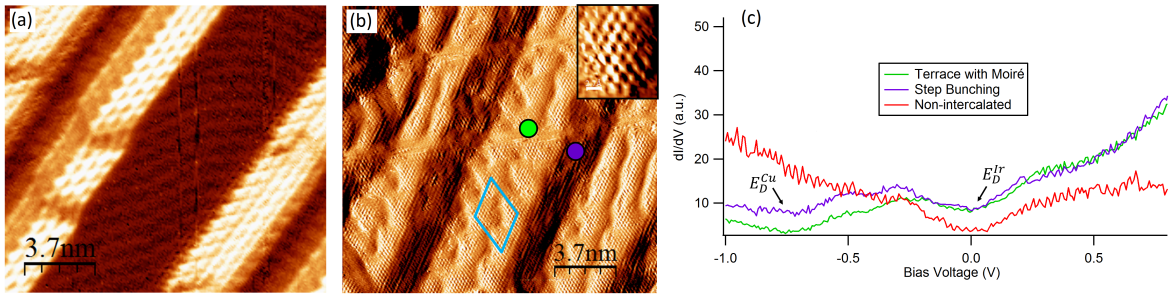

Figure 3.15: STM image of the terraces and the step-bunching areas (a) before [0.9 V, 0.5 nA] and (b) after intercalation of 0.9 ML of Cu [50 mV, 0.9 nA]. The inset shows the R0 rotation of graphene in the terrace. The blue rhombus shows the moiré unit cell of this domain. (c) STS curves performed on the areas indicated in (a) with a blue (terrace) and a green (step-bunching) circle, both indicating an n-doping of ~ -0.6 V.

the dirac point (E_D^{Cu}) at ~ -0.6 V, characteristic of n-doping and of Cu intercalation and very different from the non-intercalated spectra. This confirms that we have fully intercalated the Cu under the graphene layer, and electronic properties are therefore homogeneous. Lower coverage intercalation may give rise to a different behavior in terraces and step bunching, as we will see in the following.

Submonolayer intercalation on Gr/Ir(332)

The intercalation of 0.45 ML Cu on Gr/Ir(332) is shown on fig. 3.16. Fig. 3.16a shows the terrace/step-bunching structure, also present in the initial Gr/Ir(332) surface (fig. 3.12). The regions where Cu is intercalated could be usually identified by the enhancement of the moiré [131] when the moiré is relatively large (a few nm). However, due to the rotation of 30° between graphene and iridium (inset fig. 3.16a), the $(2x2)_{Gr}$ unit cell of the moiré (0.492 nm) is not visible on the terraces or on the step bunching. We performed scanning tunneling spectroscopy on both regions (fig. 3.16b) to identify where Cu is intercalated.

The STS curve on the terrace (fig. 3.16b) shows the characteristic behavior of Gr/Ir(322), with a state at ~ -0.25 V, marked with the blue arrow and a new dirac point (E_D^{Ir}) at $\sim +0.1$ V, indicating a slight p-doping. On the other hand, the STS curve on the step-bunching (orange) shows a shift of the dirac point (E_D^{Cu}) to ~ -0.6 V, showing a change from p- to n-doping, typical of a Gr/Cu/Ir surface due to a change in the work function of the surface [130, 147, 148]. To probe such a behavior in a large scale, we performed a conductance map at -0.6 V, shown in fig. 3.16c. The bright zones correspond to the terraces with a high intensity, while the dark areas correspond

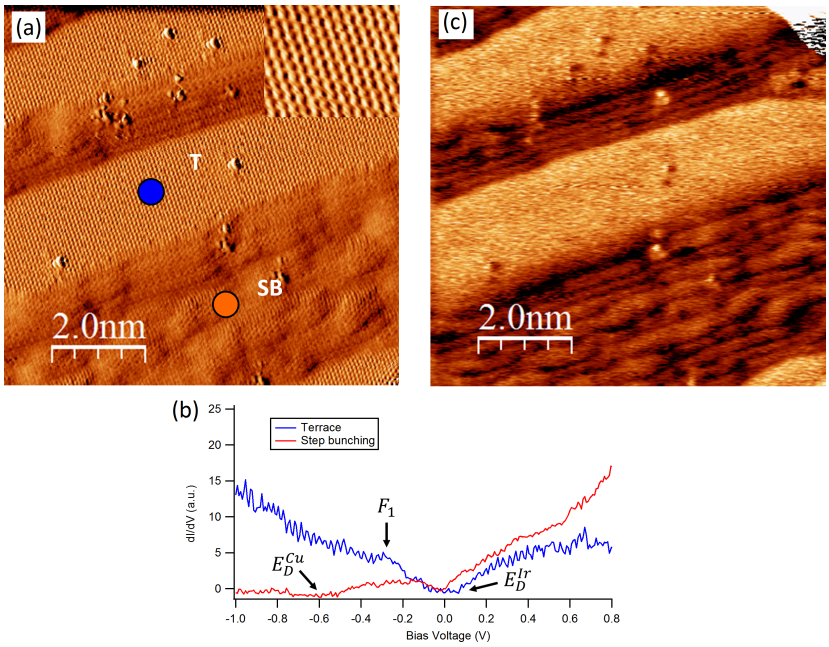

Figure 3.16: (a) 10 nm x 10 nm STM image showing the flat terraces and the step-bunching areas after intercalation of 0.45 ML of Cu [0.1 V, 2 nA]. Inset shows that graphene has a R30 orientation with respect to iridium, therefore the $(2x2)_{Gr}$ moiré unit cell of 0.492 nm is not visible neither on the terraces (T) nor on the step bunching (SB) due to its small size. The orange and blue circles indicate where spectra in (b) were acquired. (b) On the terrace we can see the F1 state at ~ -0.25 V and the dirac point is at $\sim +0.1$ V (E_D^{Ir}), typical of the p-doping of Gr/Ir(332). On the step-bunching, the dirac point is shifted to ~ -0.6 V (E_D^{Cu}), typical of the n-doping of Gr/Cu/Ir(332). (c) Conductance map (dI/dV) performed at -0.6 V (10 nm x 10 nm), showing the distinct behavior of the terraces and the step bunching areas resulting in an array of n- and p- doped nanoribbons.

to the step-bunching terraces where the Cu has been intercalated. This image proves that n- and p- doped regions are alternated on Gr/Cu/Ir(332) corresponding to the step bunching and terraces respectively. The next step would thus consist on studying the electronic properties by ARPES in order to determine the induced potential of the surface.

3.2 Superperiodic potential and band gap on Gr/Ir(332)

3.2.1 Band gap opening in periodic potentials

Nanostructuring surfaces allows to control the electronic properties of a material often by confinement effects [88, 137, 149–151]. Superperiodic potentials induced by nanostructuration are another way to control the electronic properties, where the superperio-

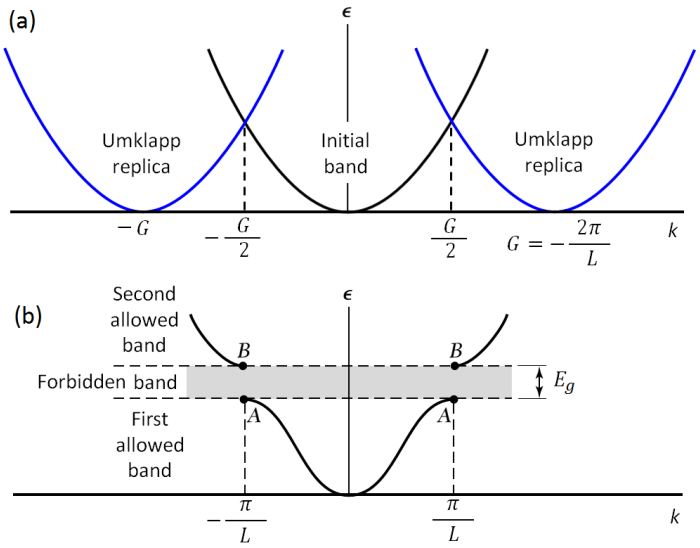

Figure 3.17: (a) E(k) scheme for a parabolic band and the Umklapp replicas due to the periodic nature of the system given by the G vector $(2\pi/L)$. (b) E(k) scheme showing the E_g band gap opening at the new Brillouin zone edges $G/2 = \pm\pi/L$ (crossing between the initial band and Umklapps).

dicities are associated to a period L in the real space that introduces a new G vector in the electronic structure $(2\pi/L)$. Fig.3.17a shows the E(k) scheme for the case of 1D superperiodicity modifying an ideal parabolic band. In black we have the initial parabolic band and in blue the Umklapp replicas associated to the G vector $(2\pi/L)$. The new periodicity induces a new Brillouin zone with edges at $\pm G/2$ (π/L), where the bands cross and therefore a band gap opening occurs, as shown on Fig.3.17b. The amplitude of the band gap (E_g) depends on the strength of the potential [152] and can modify significantly the dispersion, as shown by the flattening of the bands at points A and B (Fig.3.17b). The different scenarios for various potential strengths are shown on fig. 3.18. Finite potentials can lead to partial confinement (Fig. 3.18a), while for infinite potentials, total electronic confinement appears, leading to discrete energy levels.

The simplest model to describe the band structure of electrons in a 1D periodic potential is the Kronig-Penney model. This model consists of approximating the periodic potential to a square-well periodic potential with an analytical solution for nearly free electrons [152,153]. By adapting this model to a periodic potential induced by a stepped surface, the square potential is replaced by a Dirac barrier $U_0 b\delta(x)$ [137, 151, 154]. For the band structure of graphene, the Kronig-Penney model has been adapted by using an effective two-dimensional Dirac hamiltonian [155–157] that takes into account the pseudo-spin nature of the electrons of graphene. The periodic potential induced in this Dirac hamiltonian is sketched on fig. 3.19, where two stripes of graphene with different

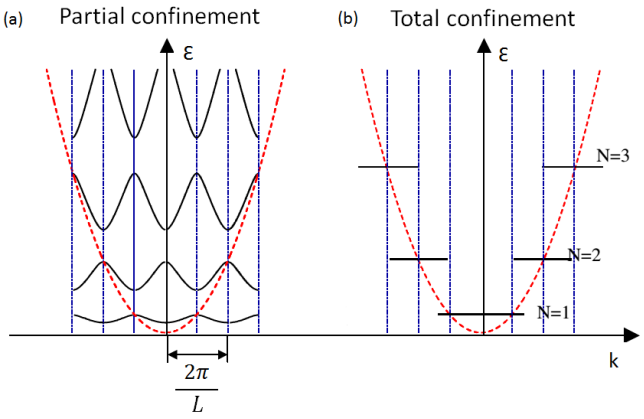

Figure 3.18: E(k) scheme showing the electronic confinement on a parabolic band (red dotted line) on a superperiodic system associated to a G vector $(2\pi/L)$. (a) Partial confinement induced by a finite periodic potential resulting in the black sinusoidal dispersing bands. (b) Total electronic confinement induced by an infinite periodic potential resulting in black flat bands.

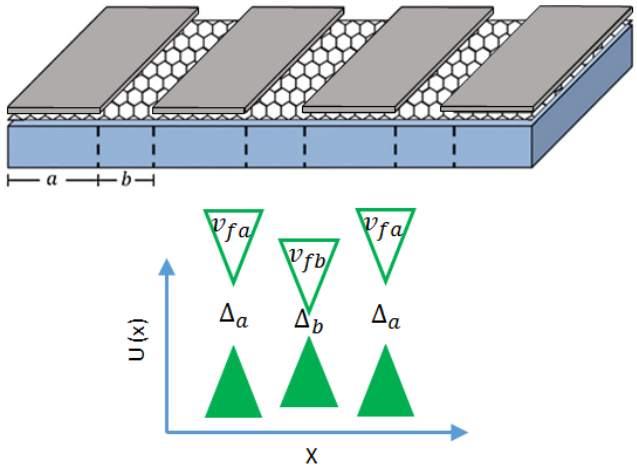

Figure 3.19: Model of a two-dimensional Dirac hamiltonian applied to graphene stripes with a periodicity $l = a + b$. The different regions are characterized by different fermi velocities (v_a and v_b) and gaps Δ_a and Δ_b.

gaps (Δ_a and Δ_b) and different fermi velocities (v_{f_a} and v_{f_b}) are repeated periodically at the surface with a period $l = a+b$ along the x axis. The Dirac hamiltonian is derived from a perturbative $\mathbf{k}\cdot\mathbf{p}$ approach that is valid around the K point of graphene. The corresponding effective Hamiltonian for massless particles with a velocity v_f is:

$$H = v_f \sigma \cdot p \tag{3.1}$$

where σ are the Pauli matrices related to the two graphene sublattices and p is the momentum operator. We consider first the direction where the potential is varying, i.e.

the x-direction. The one-dimensional hamiltonian of eq. 3.1 then reduces to:

$$H = v_f \sigma_x \frac{\hbar}{i} \frac{d}{dx} \tag{3.2}$$

If v_f depends on the x coordinate ($v_f = v_f(x)$), the problem becomes non-hermitian. It is thus necessary to find a hermitian operator for the hamiltonian that reduces to eq. 3.2 on the case that $v_f(x) = v_f$. This operator is:

$$H = \sqrt{v_f(x)} \sigma_x \frac{\hbar}{i} \frac{d}{dx} \sqrt{v_f(x)} \tag{3.3}$$

If we now include the possibility of motion along the y-direction and we include the periodic potential along x with its respective varying gaps, the two dimensional hamiltonian is:

$$H = -i\hbar \left(\sqrt{v_f(x)} \sigma_x \partial_x \sqrt{v_f(x)} + v_f(x) \sigma_y \partial_y \right) + \Delta(x) \sigma_z \tag{3.4}$$

The second term is the one dimensional operator along the y-direction as in eq. 3.2. $\Delta(x)$ is a band gap term introduced as a diagonal term in the hamiltonian through the σ_z Pauli matrix. With this hamiltonian operator, the Dirac equation is then:

$$H\psi(x,y) = E\psi(x,y) \tag{3.5}$$

where $\psi(x,y)$ is a two-component spinor that represents the two graphene sublattices. By making the variable change $\sqrt{v_f(x)}\psi(x,y) = \phi(x,y)$, the Dirac equation becomes:

$$-i\hbar v_f(x) \sigma_x \partial_x \phi(x) + [\Delta(x) \sigma_z - \hbar k_y \sigma_y] \phi(x) = E\phi(x) \tag{3.6}$$

which can be rewritten as:

$$i\frac{d\phi(x)}{dx} = M(x)\phi(x) \text{ with } M(x) = \begin{pmatrix} ik_y & \frac{-E-\Delta(x)}{\hbar v_f(x)} \\ \frac{-E+\Delta(x)}{\hbar v_f(x)} & -ik_y \end{pmatrix} \tag{3.7}$$

The solution of Eq. (3.7) is given by:

$$\phi(x) = \mathcal{P} exp\left(-i \int_x^{x_0} dx' M(x') \right) \phi(x_0) \tag{3.8}$$

where $\mathcal{P}$ is the path ordering operator, and can be simplified as:

$$\phi(x) = \Lambda(x - x_0)\phi(x_0) \tag{3.9}$$

where $\Lambda(x - x_0) = exp[-i(x - x_0)M(x)]$.

By expanding we obtain the relation:

$$det[\Lambda(a+b) - exp[ik_x \cdot (a+b)]] = 0 \tag{3.10}$$

which yields the relation $2cosk_x \cdot (a+b) = Tr[\Lambda(a+b)]$ and allows to determine the dispersion relation:

$$\cos(k_x l) = \cos(k_a a)\cos(k_b b) + \frac{k_y^2 \hbar^2 v_{fa} v_{fb} - E^2 + \Delta_a \Delta_b}{\hbar^2 v_{fa} v_{fb} k_a k_b} \sin(k_a a)\sin(k_b b) \tag{3.11}$$

with the following relations:

$$k_a = \left(\frac{\left[E^2 - {\Delta_a}^2\right]}{\hbar^2 {v_{fa}}^2} - k_y^2 \right)^{1/2} \tag{3.12}$$

$$k_b = \left(\frac{\left[E^2 - {\Delta_b}^2\right]}{\hbar^2 {v_{fb}}^2} - k_y^2 \right)^{1/2} \tag{3.13}$$

Upon comparison of this theoretical dispersion with the experimental one it should be possible to obtain Δ_a, Δ_b that will allow us to understand the strength of the surface potential.

3.2.2 Periodic potential from ARPES measurements

We have seen in the previous section that the band structure contains the information about the superperiodic potential. As ARPES is the ideal technique to determine the experimental E(k) relation, it therefore allows to study the potential strength. We have thus studied the band structure of Gr/Ir(332) by CVD by ARPES. The sample was first grown on the Cassiopée preparation chamber and immediately measured afterwards. Fig. 3.20a shows the experimental geometry, with terraces (green) and step bunching (orange) on the surface.

The bands of the terrace ($\Delta\theta_{Terr}$ in orange) and step-bunching areas ($\Delta\theta_{SB}$ in green) appear at different angular regions. Each one of these bands should be affected by the overall periodic potential. Fig. 3.20b shows the Fermi surface obtained at $h\nu = 150$ eV that allows to explore a large region of reciprocal space to identify the area of interest. The E(k) dispersion along the dotted lines on panel (b) is shown in panels (c) and (d).

In the dispersion relation, we appreciate several linear dispersing bands, corresponding to the different domains of graphene already seen in LEED (R0, R25, R30 and R35), and identified in fig. 3.20b with orange and green dots. Using the scheme of the first

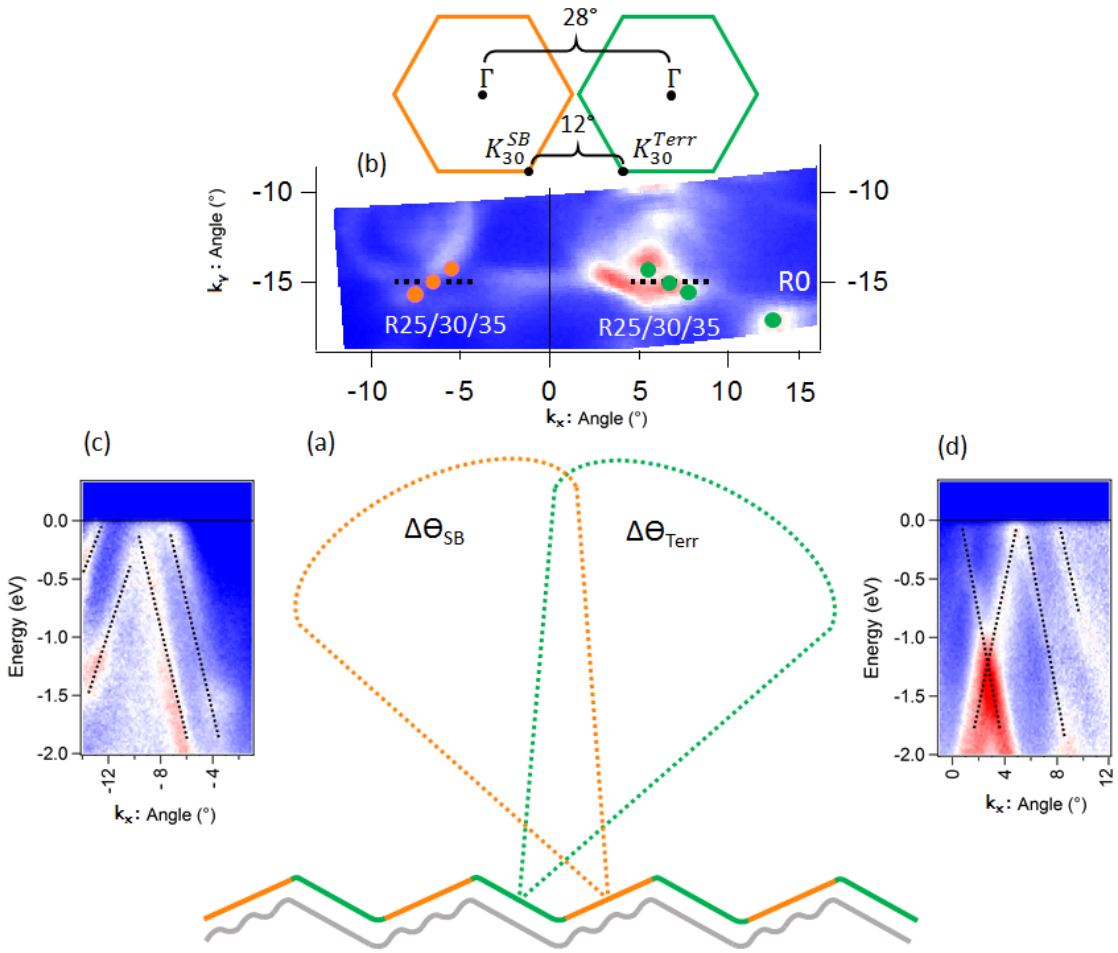

Figure 3.20: (a) Sketch of the superperiodic surface, showing the angular range of detected intensity for the terraces ($\Delta\theta_{Terr}$) and step-bunching ($\Delta\theta_{SB}$) areas. (b) k_x vs. k_y map at the Fermi Level showing the traces of the different rotational domains of graphene (R30, R25/R35) as well as R0, coming from the terrace and step bunching areas. Some bands of the substrate are also visible ($h\nu$ = 150 eV). (c)(d) E vs. k_x cut along the dotted lines in (b), where the cones of the R30 and R25/R35 domain are highlighted by dotted black lines. The reciprocal space is represented in terms of angles.

Brillouin zone for graphene from the terrace and step-bunching areas and the Fermi surface on fig. 3.20b, we find that the angular distance between the ${K_{30}}^{Terr}$ and ${K_{30}}^{SB}$ is around 12°. We also know the angular distance between Γ and the projection of either K_{30} on the horizontal axis is around 8°. This results in a Γ-Γ distance of around 28°, meaning that there is a tilt of 28° between the terrace and the step-bunching surfaces. Knowing that the width of the terrace and step bunching areas is 3.5 nm and

the local tilt angle between them is of 28°, we calculate the optical tilt angle at 14°, which is close to the 10° of the pristine Ir(332) surface. The difference on the optical tilt angle between the Ir(332) and the Gr/Ir(332) surfaces is due to the reconstruction of the steps into step-bunching that resulted in equally large terrace and step bunching areas. Once all the features at the Fermi surface are understood, we concentrate on the cone of the R0 rotation, being the most intense one. The R0 dispersion of the terrace is explored in more detail by using a lower excitation energy ($h\nu$ = 32 eV) that allows to probe roughly half of the reciprocal space measured in fig. 3.20 (in fig. 3.20 we were able to probe 3Å^{-1}, while on fig. 3.21 we probe $\sim 1.5\text{Å}^{-1}$). The black line shows the linear dispersion of the π band of the R0 domain. A doping of 330 meV is appreciated on the experimental band structure in agreement with previous results [122,125,126,134,136,158]. The blue lines correspond to the less intense R35/R25 and R30 domains. The green lines are identified as Ir states *S1*, *S2* and *I* (shown on the line profile done at 0.6 Å^{-1}). *S1* is closer to the Fermi level, and its intensity depends on the excitation energy [126]; in our case it overlaps with the graphene band at the Fermi level. The Ir band at -1 eV is the *S2* state [159]. Finally the state at ~ 1.6 eV is the *I* band, whose spectral weight is also excitation energy-dependent [159].

As we analyze the graphene band, we notice that graphene has a linear dispersion with the fermi velocity of ideal graphene (measured between the Fermi level and -1.5 eV). Along the graphene linear band there are some places on which the spectral weight decreases. To better observe this behavior, we performed the derivative of (a) (fig. 3.21b). It becomes now clear that three locations along the π band have an intensity decrease. To better appreciate this effect, we plot the Energy Distribution Curves (EDC) in fig. 3.21c every 0.58° along the $K - M$ direction. By following the maxima of the band, it is appreciated the characteristic behavior of band gap opening, that is correlated to the intensity decrease previously observed, indicated by black arrows. These three features are characterized by $E_g = 390 \pm 20$ meV, a difference between the band gaps of 0.60 ± 0.06 eV and a $G/2$ vector of 0.09 ± 0.02 Å^{-1}, corresponding to a L of 3.5 ± 0.9 nm ($G = 2\pi/L$), which is precisely the characteristic width of the terraces and step bunching. This analysis allows us to conclude that there is an effect of the nanostructuration on the electronic properties of graphene. We will now apply the model previously presented in Section 4.2.1. to the experimental band structure.

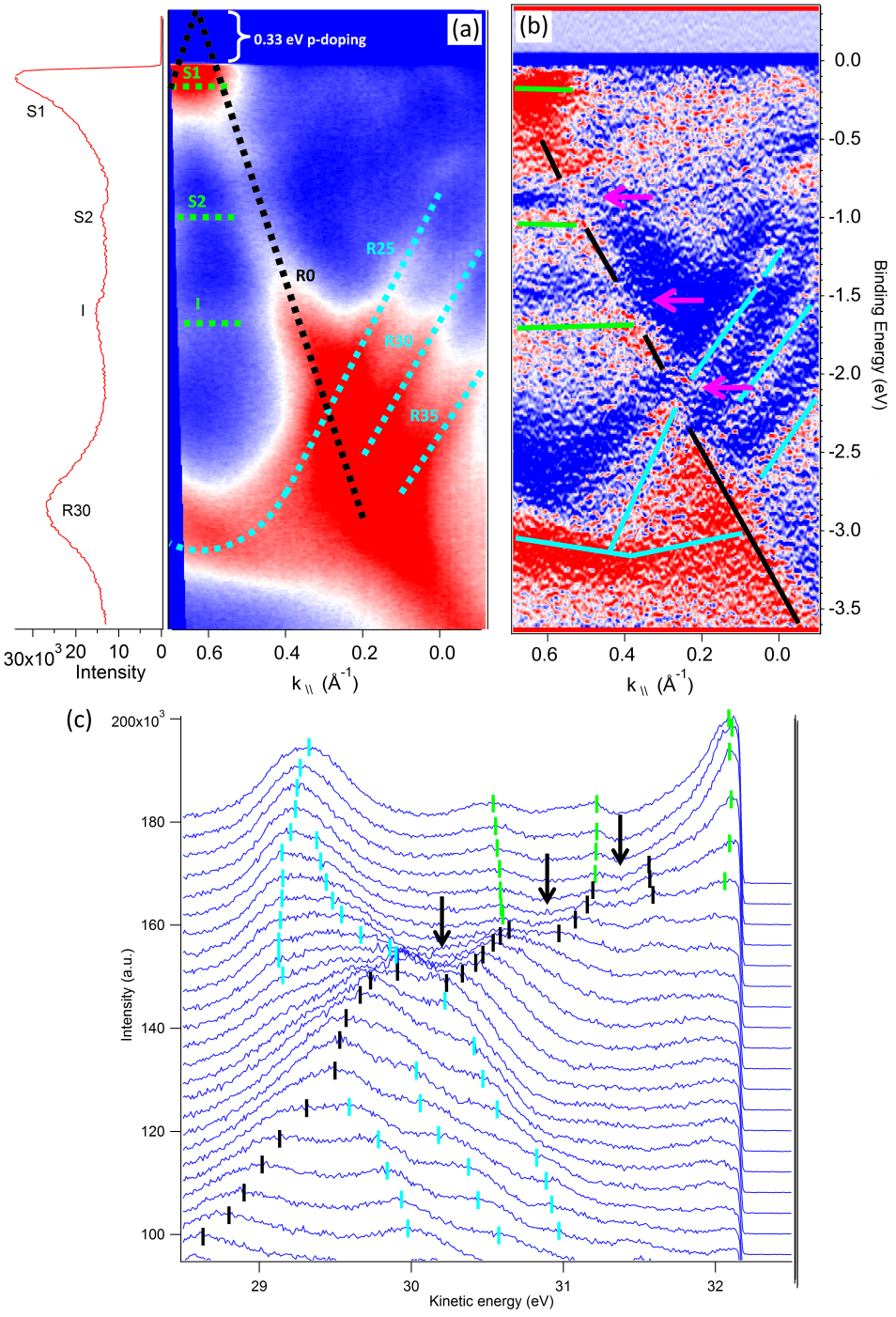

Figure 3.21: (a) E(k) map of Gr/Ir(332) at the K point of the R0 rotation coming from the terraces ($h\nu = 36$ eV of excitation photon energy). The green bands are the S1, S2 and I iridium surface states, also shown on the line profile at 0.6 Å^{-1}. The blue bands are graphene bands (R25, R35 and R30). The black line is the R0 graphene band, that allows to appreciate a doping of 330 meV in agreement with previous results [122,125,126,134,136,158]. (b) First derivative of (a). Three band gaps are marked by the pink arrows. (c) Energy distribution curves of (a) every 0.58° along the $K - M$ direction, where the maxima of the bands are followed with vertical lines. The black arrows show the location of the band gaps with $E_g = 390 \pm 20$ meV and a separation in energy between the gaps of 0.60 ± 0.06 eV and in reciprocal space by a $G/2$ vector of 0.09 ± 0.02 Å^{-1}.

3.2.3 Dirac-hamiltonian model on Gr/Ir(332)

The Dirac hamiltonian model for superperiodic graphene can be adapted to our Gr/Ir(332) system; fig. 3.22 shows the physical representation of the used parameters.

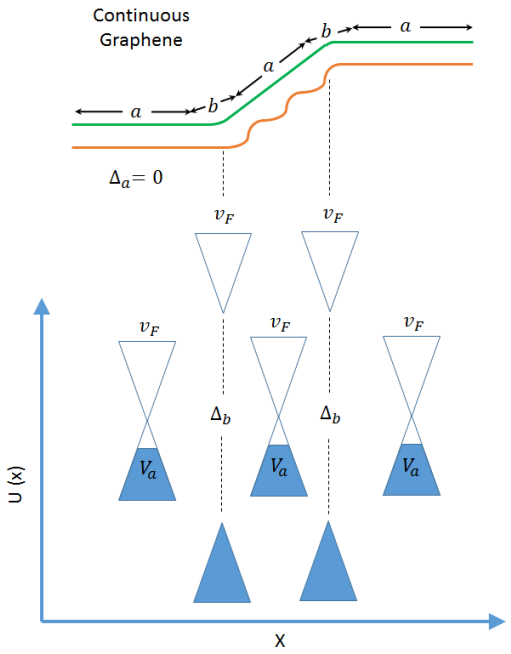

Figure 3.22: Physical representation of the parameters used on the Dirac hamiltonian model of graphene with a periodicity $a + b$, where a is the terrace/step bunching width and b is the junction of only a few Å wide. The fermi velocity and doping is identical for both regions ($v_{fa} = v_{fb} = v_f$, $V_a = V_b = 330meV$), as experimentally observed. We modelize the potential barrier on region b by introducing a sizable gap ($\Delta_b = \Delta$), while $\Delta_a = 0$.

The superperiodicity is given by $l = a + b$, where a is the terrace/step bunching width and b is the limit between these regions, usually a few angstroms. Both regions present the same ideal fermi velocity, as probed by ARPES, simplifying to $v_{f1} = v_{f2} = v_f$. In this model, the doping of graphene is modeled by V_a and V_b. As measured by ARPES, the doping of graphene is $V_a = V_b = 330meV$. Additionally, a sizable gap opening mimics the potential barrier present on region b for the Gr/Ir(332) case ($\Delta_b = \Delta$). Therefore, Eqns. (3.11), (3.12) and (3.13) are corrected for our case as following:

$$\cos(k_x l) = \cos(k_1 a)\cos(k_2 b) + \frac{k_y^2\hbar^2 v_f^2 + E\cdot(E-V)}{\hbar^2 v_f^2 k_1 k_2} \tag{3.14}$$

with the following relations:

$$k_1 = \left(\frac{[V - E]^2}{\hbar^2 v_f^2} - k_y^2 \right)^{1/2} \tag{3.15}$$

$$k_2 = \left(\frac{E^2 - \Delta^2}{\hbar^2 v_f^2} - k_y^2 \right)^{1/2} \tag{3.16}$$

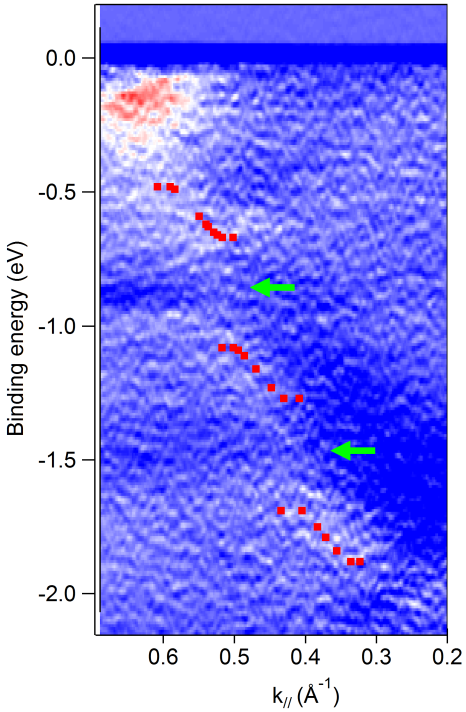

Figure 3.23: Model of the Gr/Ir(332) band structure (red dotted line) fitted with a two dimensional Dirac hamiltonian on a superlattice with parameters: $a = 3.3$ nm, $b = 0.2$ nm and $V = 0.33$ eV. The recovered strength of the potential is 4.4 eV Å, which recreates the band gap opening of 390 meV (green arrows).

To find a solution to eqns. 3.14, 3.15 and 3.16, we use a numerical method. As we are interested in the band dispersion along k_x, where the potential is varying, we consider $k_y = 0$. The dopings V_a and V_b, and the spatial lengths a and b were estimated experimentally from the results presented on figs. 3.11, 3.12 and 3.21. The fermi velocity was also determined experimentally from the photoemission results. The only free parameter is then Δ. For different values of Δ, we loop E (with a step of 0.01 eV) and k_x (with a step of 0.01 Å^{-1}) in the region of interest to compare to the experimental data around the gaps. The calculated dispersion within the Dirac hamiltonian model corresponds to the Δ, E and k_x values that satisfy eq. 3.14 to an accuracy better than 0.001. In this case, the (E, k) pair corresponds to a solution for a given Δ. The calculated dispersion is then superimposed on top of the experimental

data. If the solution set does not accurately reproduce the ARPES data, we vary Δ until an adequate Δ is found.

The comparison of calculations with the experimental band structure is shown on fig. 3.23 (a different color scale with respect to that of fig.3.21 is used here). The calculations were performed with $V = 0.33$ eV, $a = 3.3$ nm and $b = 0.2$ nm. These a and b distances are compatible with the STM observations. We found $\Delta = 2.2$ eV, resulting in a potential strength of $\Delta \cdot b = 4.4$ eV Å (comparable to other values found on noble metallic stepped surfaces [151]), which gives rise to electronic partial confinement. As the confinement may depend on the terrace width, we will in the following study graphene on a curved Pt crystal (Chapter 4) in order to explore different vicinal surfaces at the same time around the nominal Pt(111) surface.

3.3 Conclusions and perspectives

In this chapter we explored the modification of the electronic properties of graphene by nanostructuration of the substrate. We first studied the growth and morphology of graphene on the Ir(332) by two different methods: temperature programmed growth and chemical vapor deposition. We also intercalated Cu, where a periodic structure with a modulation of the electronic properties was observed by STS. ARPES measurements observed band gap openings due to the superperiodic potential that are explained with a Dirac-hamiltonian. More precisely we have understood:

- The growth and structure of graphene on Ir(332) via CVD and TPG

Graphene growth via both TPG and CVD modifies the original steps of the Ir(332) substrate and transforms the underlying surface in an array of terraces and step bunching areas where graphene later grows. The TPG technique produces graphene domains aligned with the underlying substrate that fully covers the step bunching areas. CVD allows to obtain continuous graphene on top of the whole Ir(332) surface with various coexisting rotational domains. All the graphene areas have the same spectroscopic signal than Gr/Ir(111) with a slight p-doping. On the other hand, in the sub-monolayer coverage of intercalated Cu, Cu preferentially intercalates on the step bunching area, resulting in an array of n- and p- doped nanoribbons on a single continuous layer.

- The origin of the band gap opening in the graphene electronic band structure

As the continuous graphene grown by CVD on Ir(332) presented an homogeneous periodic structure due to the periodicity of the step bunching array, its electronic structure could be modulated by the superperiodic potential. To probe these effects, its electronic structure was probed by ARPES and we observed several band gaps. Our combined study of STM and ARPES allowed us to describe the system with a Dirac hamiltonian model. We retrieved the potential strength at the edge of both terraces and step bunching of 4.4 eV Å, which produces partial confinement.

There are of course improvements to be made at the different stages of growth, electronic structure measurement and modeling, which open new perspectives for research in this field. On TPG, well ordered discontinuous nanoribbons can be probably obtained by profiting from the initial growth on the step bunching areas. Also, a combination of TPG + CVD, could be explored to produce graphene nanoribbons, where TPG could produce patches of graphene with a specific rotational domain and CVD would serve to slowly grow them. The confinement potential could also be varied by changing the nature of the intercalated element. In conclusion this study has demonstrated the possibility of modifying the electronic properties of graphene by nanostructuration. Further studies may allow to reach a better control, eventually in systems closer to real applications.

Chapter 4

Electronic structure tailoring on multivicinal Pt(111)

In this chapter we discuss the modification of the electronic properties of graphene due to its growth on a nanostructured Pt substrate. We present the growth and morphology of graphene via chemical vapor deposition at different vicinal orientations of Pt(111). We then probe the electronic band structure by ARPES and apply a Dirac-hamiltonian model to compare the surface potential to that of Gr/Ir(332).

4.1 Growth and structure of graphene on Pt

Platinum is a catalytic noble metal that has similar behavior to iridium on its interaction with graphene, as the Gr-Pt separation is 3.70 Å, again larger than the interlayer distance in graphite [160]. It has been shown that graphene on Pt(111) forms different rotational domains (R0, R30, R19, etc.) [161–164], whose signature in diffraction techniques are well-defined spots rotated with respect to those of the substrate. On the other hand, diffraction arcs also form as a result of indistinguishably close rotational domains [162, 165, 166]. The formation of sharp spots or arcs depends on the growth parameters. Fig. 4.1a shows for instance a preparation exhibiting both well-defined rotational domains and arcs. The different rotations of graphene with respect to platinum give rise to several moiré patterns that can coexist. The coexistence is appreciated on the STM image in fig. 4.1b, where two moirés appear on a single terrace, as shown by a different corrugation on the red line profile. However, different domain coexistence is not correlated to the platinum terraces, as graphene can extend across them, as shown

by the continuity of the moiré pattern across the step edge (figure 4.1b).

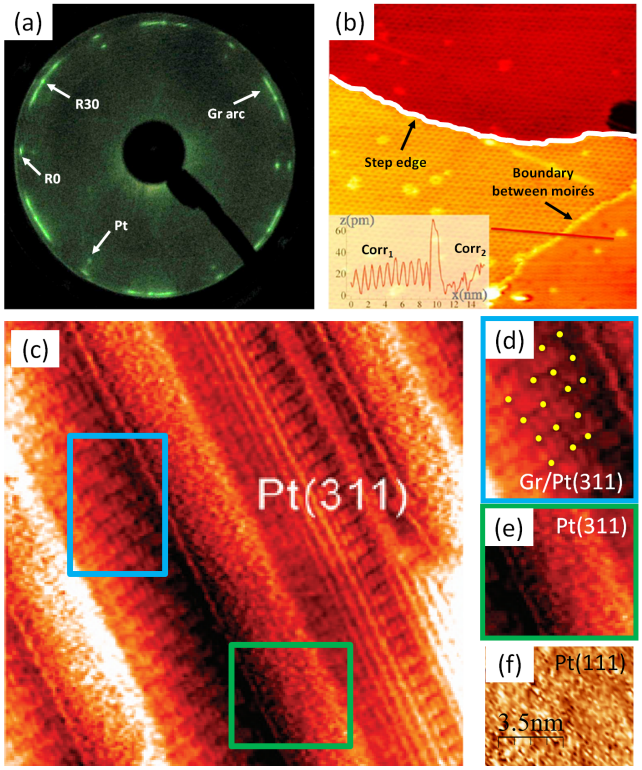

Figure 4.1: (a) LEED pattern of Gr/Pt(111) where some well defined domains (R0, R30) are present. The pattern also exhibits some arcs corresponding to rotational domains very close in angle. (b) STM image showing the continuity of graphene between two Pt(111) terraces. The moiré preserves the same orientation on both sides of the step edge. On the lower terrace, two rotational domains coexist. The profile along the red line shows the different corrugations of the two moiré ($Corr_1$ and $Corr_2$) [167]. (c) STM image showing the discontinuity of graphene grown on Pt(311). The blue and green rectangles correspond to the different facets of the surface. (d) Zoom on the blue area on panel (c), where the yellow dots highlight a periodic pattern, attributed to graphene. (e) Zoom on the green area, where no periodic features are observed, similar to bare Pt(111) on panel (f) [1 V, 0.8 nA] [168].

Although the growth within the flat platinum surface is very similar to that on Ir(111), recent studies have shown that discontinuous graphene can be obtained for certain crystallographic orientations, as on Pt(311) (fig. 4.1c-f). The surface consists of two sets of facets marked by the blue and green rectangles (fig. 4.1c). Panel (d) shows the zoom of the blue area, where the periodic structure is attributed to graphene. On the other hand, at the adjacent facet, no distinguishable features of graphene are found (panel (e)), consistently with bare Pt(111) (panel (f)).

In order to probe a wide range of vicinal surfaces of Pt(111), some of which might produce discontinuous graphene nanoribbons, we have bought a curved Pt crystal to

Bihur Crystal (San Sebastian, Spain), whose macroscopic orientation is tilted up to 16° towards the $[11\bar{2}]$ and the $[\bar{1}\bar{1}2]$ directions (fig. 4.2a-b). The 9 mm×9 mm curved Pt crystal consists of terraces of different widths, depending on the macroscopic vicinal angle, that run parallel to the $[1\bar{1}0]$ direction. The major advantage of a curved crystal is that a single graphene growth process allows to probe several vicinal surfaces at the time. By studying different sites across the red line (fig. 4.2b), each of them corresponding to various terrace sizes, we will obtain the electronic structure associated to each terrace and correlate it to the atomic structure.

4.1.1 Preparation of multivicinal Pt(111) substrate

The cleaning of the Pt(111) multivicinal substrate consists of a first sputtering cycle at RT with a 1keV Ar^+ beam at 8×10^{-6}mbar pressure at three different sample locations. The sputtering is performed along the $[1\bar{1}0]$ direction (parallel to the steps), to preserve the vicinality of the surface. The sputtering is followed by an electron bombardment annealing at 700°C for 10 min later cooled down to RT at a controlled rate of 60 ± 10 °C/min. A second cycle of sputtering is followed by an annealing under oxygen atmosphere (1×10^{-7}mbar) for 10 min. The sample is then cooled down to RT at a controlled rate of 60 ± 10 °C/min and a final flash is performed at 950°C. To accurately read the temperature along the crystal, we have measured the temperature with a pyrometer ($\epsilon = 0.1$) at the center of the sample.

After repeated cycles of sputtering/annealing, LEED and STM were performed on several positions on the sample, 1 mm apart. The negative and positive positions are associated to the A-steps and B-steps respectively that are found on either side of the crystal (fig. 4.2c). On the A-step terminated edges, the last atomic row of the upper terrace are aligned with the first atomic row of the lower terrace. On the other hand, on the B-step terminated edges, the last atomic row of the upper terrace is shifted by half a lattice parameter parallel to the step with respect to the first atomic row of the lower terrace. Seven different points were probed by STM and LEED: −3mm, −2mm, −1mm, 0mm, +1mm, +2mm, +3mm. These positions present a macroscopic vicinal angle with respect to the (111) surface of −14.5°, −11°, −7°, −3.5°, 0°, +3.5°, +7°, +11° and +14.5° respectively. In the following, we will refer to this vicinal angle to present our results. Representative regions are shown on fig. 4.2.

In the region corresponding to the Pt(111) surface (panel h), the terraces are large and without a preferential orientation, as seen in the STM image (panel j). As we move

away from the center towards the A-steps region, the LEED shows a sharp splitting of the Pt(111) spots along the $[11\bar{2}]$ direction (panels f and d). By measuring the split-

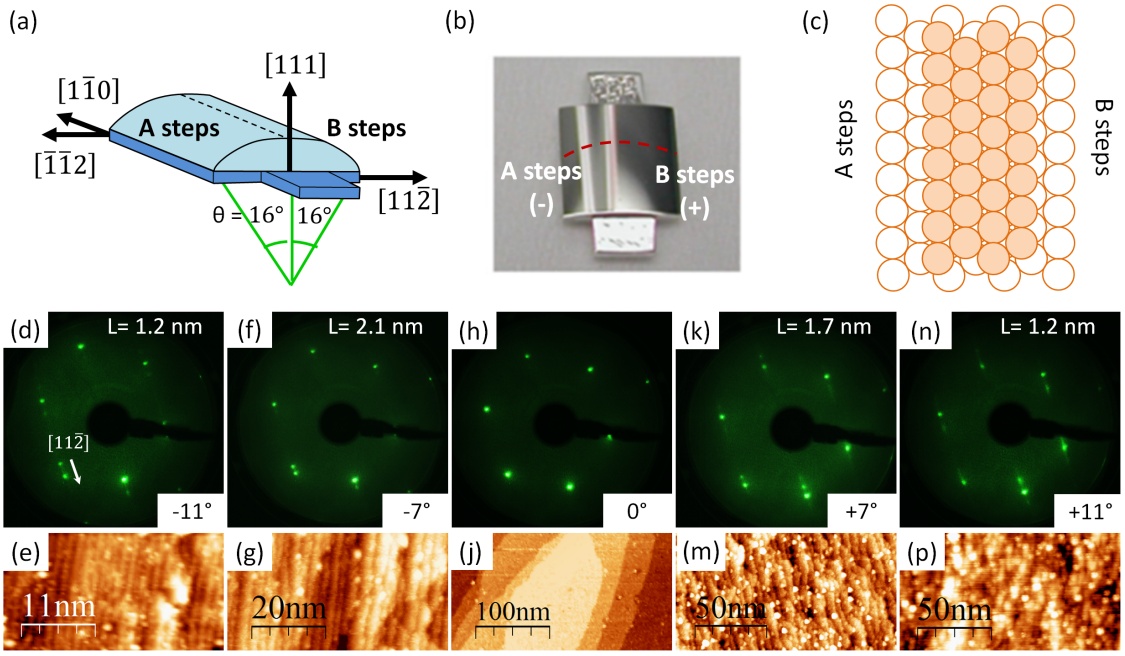

Figure 4.2: (a) Scheme of the curved Pt crystal. The Pt(111) orientation is found at the center (vicinal angle = 0°, x = 0 mm), and as we move further away from the center up to a tilt of 16° towards the $[11\bar{2}]$ or $[\bar{1}\bar{1}2]$ directions, the vicinal surfaces present A or B step edges respectively. The steps of the vicinal surfaces run along the $[1\bar{1}0]$ direction. (b) Image of the curved Pt crystal, where the center of the sample is referred as vicinal angle 0°, while the side with A-steps or B-steps are referred with negative or positive values respectively, measured in vicinal angle with respect to the [111] direction. (c) Schematic of the Pt(111) surface and the geometry of A-step and B-steps. LEED images at incoming electron beam of 128 eV as for vicinal angles (d) −11°, (f) −7°, (h) 0°, (k) +7° and (n) +11°. The terrace size decreases away from the center. The LEED splitting associated to the vicinality is sharp on the A-steps side and blurred on the B-steps side. STM images corresponding to vicinal angles (e) −11°, (g) −7°, (j) 0°, (m) +7° and (p) +11° [1 V, 0.8 nA]. At vicinal angle 0°, the Pt(111) large terraces are recovered, while at both sides of the sample, the terrace size decreases. STM also shows higher quality of terraces in the A-step side.

ting and comparing it with the distance between the Pt(111) spots, the terrace size is L = 2.1 ±0.1 nm and L = 1.2 ±0.1 nm for the −7° and −11° vicinal angles respectively, in agreement with the expected vicinal surface. The splitting spots are sharp, indicating the high quality ordering of the terraces, as seen by the well-defined periodicity observed by STM on panels g and e.

When moving from the center towards the B-steps side, the LEED shows a blurred splitting of the Pt(111) spots (panels k and n). The blurred splitting indicates a wider

distribution of terraces and a lower ordering of the surface. The quality decrease is also observed on the STM images in panels m and p. Despite this disorder observed in STM, the terrace size can be calculated by LEED reaching $L = 1.7 \pm 0.3$ nm and $L = 1.2 \pm 0.2$ nm for the $+7°$ and $+11°$ vicinal angles respectively, in agreement with the expected vicinal surface.

4.1.2 Graphene growth on curved Pt by chemical vapor deposition

The Chemical Vapor Deposition (CVD) technique was chosen since the crystal is large (9 mm×9mm), and it is desirable to grow graphene nanoribbons on the whole surface at once (in TPG, the growth is done in several stages). As we expect to have discontinuous graphene at step edges at certain vicinalities, CVD is the ideal candidate for such a growth. We chose again ethylene (C_2H_4) and similar parameters to those used for Gr/Ir(332). The substrate is annealed to 800°C for 10 min. while exposed to an ethylene partial pressure of 3×10^{-7} mbar. The sample is then cooled down to RT at a controlled rate of 60±1 °C/min. The surface is characterized by LEED (electron incoming beam at 82.3 eV to observe the (1x1) spots of Pt and the details around them) and analyzed by RT scanning tunneling microscopy at the Surface Laboratory in the Soleil Synchrotron. Fig. 4.3 shows the LEED patterns and the STM images of different vicinalities obtained as a function of the vicinal angle.

The growth at the position corresponding to Pt(111) is as expected. The LEED (panel d) shows different features of graphene on Pt: a sharp R30 domain and an arc around it. The inset shows the (1x1) spot of platinum and two graphene rotations at ±5° (R5, R5'). The intensity of these graphene orientations decreases away from the (111) surface. The STM images on vicinal angle 0° (panel d) show non-ordered large terraces. Graphene presents several rotations as demonstrated by the two different moiré structures on atomic resolved images (the moiré unit cell is indicated by the white rhombus on panel d). Graphene grows over the step edges, as demonstrated by the continuity of the honeycomb network (white hexagons) on both sides of the steps, in agreement with previous work [162–164, 167] (see also zooms in the Appendix A.3).

When exploring the A-steps side, the step array is homogeneous for the small vicinal angle $-3.5°$ (panel c). A clear splitting of the $(1x1)$ Pt spots is observed on the LEED inset, which corresponds to a periodicity of $L = 5.8 \pm 0.8$ nm. The 3D STM image shows a homogeneous periodic structure composed of (111) terraces and step bunching

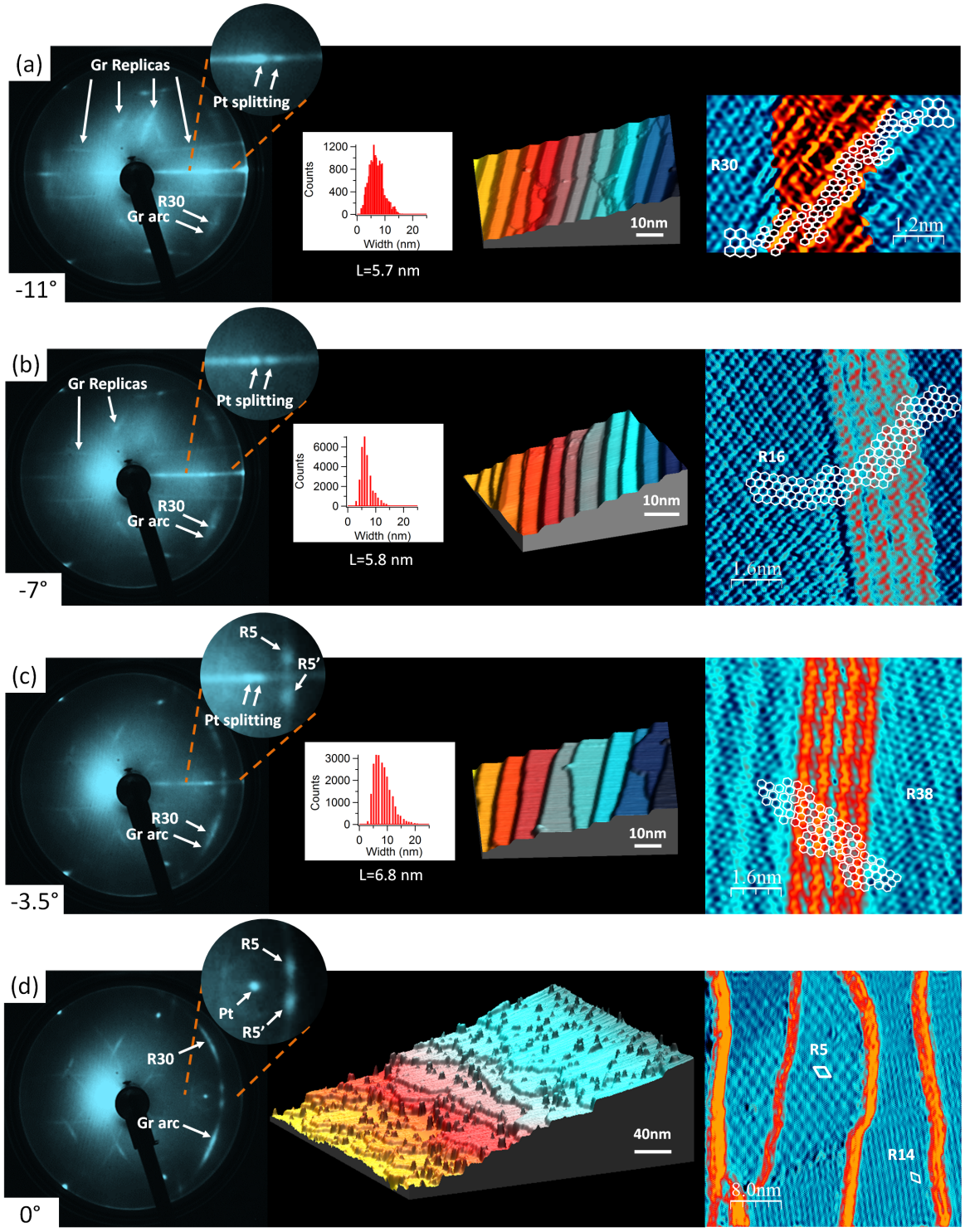
(a)
Gr Replicas
Pt splitting
R30
Gr arc
-11°
Counts
Width (nm)
L=5.7 nm
10nm
R30
1.2nm
(b)
Gr Replicas
Pt splitting
R30
Gr arc
-7°
Counts
Width (nm)
L=5.8 nm
10nm
R16
1.6nm
(c)
R5
R5'
Pt splitting
R30
Gr arc
-3.5°
Counts
Width (nm)
L=6.8 nm
10nm
R38
1.6nm
(d)
R5
Pt
R5'
R30
Gr arc
0°
40nm
R5
R14
8.0nm

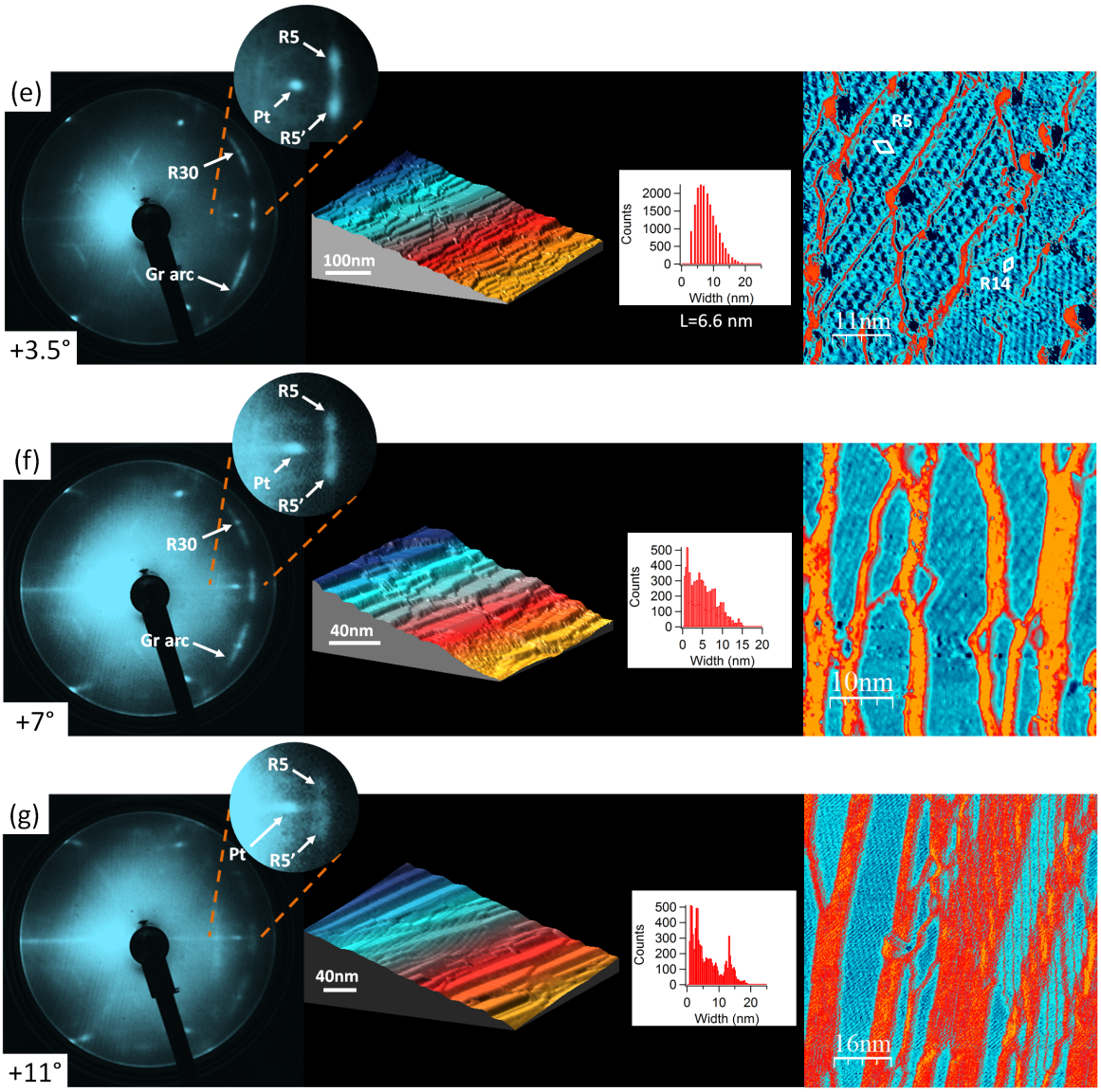

Figure 4.3: LEED (left), 3D STM (center) and details of the STM images (right) for vicinal angles (a) $-11°$ [1.14 V, 0.7 nA], (b) $-7°$ [100 mV, 2.8 nA], (c) $-3.5°$ [70 mV, 2.6 nA], (d) $0°$ [360 mV, 2.6 nA], (e) $+3.5°$ [1 V, 0.8 nA], (f) $+7°$ [1 V, 0.5 nA] and (g) $+11°$ [1 V, 0.8 nA]. Three main graphene features appear: R30, equivalent R5/R5' rotations and multidomain arcs. The A-steps side (a-c) presents a gradual splitting on the Pt spot, indicating the formation of a well ordered periodic system, whose period L (terraces + step bunching) varies from 6.8 to 5.7 ± 1.4 nm obtained by PWD histograms. The B-steps side (e-g) does not show the Pt spot splitting in LEED, although STM images and PWD histograms confirm that there is a certain degree of order. Atomic resolution images suggest the continuity of graphene, as the graphene honeycomb on the blue terraces is oriented in the same way at both sides of the orange step bunching area. The white rhombus highlights the unit cells of moirés. Appendix A.3 shows the zoom of panels a-c.

areas. A pixel-by-pixel analysis of the STM image perpendicular to the steps allows to detect the step edges and to calculate the surface periodicity L (from the terrace and the step bunching). The inset shows the sharp Periodic Width Distribution (PWD) histogram indicating a periodicity of $L = 6.8 \pm 1.8$ nm. Graphene is continuous across the terraces (blue in the right panel) and step bunching (orange), as shown by the honeycomb structure on both sides of the step bunching, indicating the absence of discontinuous graphene ribbons.

For a vicinal angle of $-7°$, we find the best ordered surfaces (panel b). For the first time, we observe replicas of the graphene arcs, resulting from the high ordered periodic structure. The periodicity here is smaller, $L = 5.8 \pm 1.5$ nm as calculated from the LEED spots and observed in STM images, showing narrower terraces as the result of a wider step bunching. The inset shows the PWD histograms with a periodicity of $L = 5.8 \pm 0.5$ nm. Here, graphene is also continuous, as suggested by the honeycomb on the blue terraces at both sides of the orange step bunching areas.

Finally, the highest vicinal angle that we studied is $-11°$. Pt spot splitting in LEED is similar to that observed for $\theta = -7°$, corresponding to $L = 4.8 \pm 1.5$ nm. The 3D STM image shows straight-edged terraces, while the PWD histogram indicates a periodicity of $L = 5.7 \pm 1.8$ nm. The large error bar is in agreement with the broad Pt splitting spot in LEED, reflecting a less homogeneous surface.

On the contrary, as we move towards the B-steps side, the LEED of the vicinal angle $+3.5°$ is initially very similar to that of the flat surface. STM images show the apparition of a preferential orientation for steps and the development of step bunching areas (panel e: gray areas on the 3D image and orange on the atomic resolution image), leading to smaller terraces. The inset shows the PWD histogram that gives $L = 6.6 \pm 2.7$ nm. The atomically resolved STM images show that the terraces are only partially homogeneous, as their edges wiggle, giving rise to widths between 4.6 and 6.6 nm. Such an observation explains why the spot splitting is observed on the LEED. Despite the inhomogeneous terrace width, graphene rotational domains (R5 and R14) are continuous across the steps, as highlighted by the continuity of the moiré unit cell on both domains (white rhombus on panel e) in the STM image.

When moving even further away along the B-steps side to the vicinal angles $+7°$ and $+11°$ (panels f and g), the platinum spots lose intensity in the LEED pattern, and the splitting is less defined, indicating the weakening of the ordering of the step array. Graphene is still observed in atomically resolved images, but STM images show the disorder of the step array. The PWD histograms show the inhomogeneity in a broad

histogram of widths, ranging from 2 to 15 nm for $\theta = +7°$ and from 2.5 nm to 13 nm for $\theta = +11°$. These areas will be discarded from the electronic structure analysis due to the structural inhomogeneity.

In conclusion, we observe that graphene grows more ordered in vicinal surfaces on the A-steps side, as seen by the splitting of the Pt spot. The quality of the step periodicity decreases at the edges of the sample, namely for vicinal angles $+11°$ and $-11°$ with respect to intermediate sites. Graphene grows continuously across the sample between the terraces and step bunching areas. With the obtained continuous graphene, we expect a modification of the electronic properties similarly to Gr/Ir(332) via the nanostructuration and the appearance of a superperiodic potential.

4.2 Band gap tailoring on graphene on multivicinal Pt(111)

As indicated in chapter 3, information about superperiodic potentials is contained in the band structure. We will thus use ARPES to determine the experimental E(k) relation and measure the potential strength induced in graphene by the periodic nanostructuration. We will compare the effect of nanostructuring on different vicinal surfaces.

Fig. 4.4a-c shows the E(k) maps obtained at the K point of graphene along a direction perpendicular to the steps as a function of the vicinal angle. The first striking feature is that the linear dispersion of graphene is discontinuous, as the intensity decreases at certain energies and its E(k) location depends on the vicinal surface, as we will see. Panels d-f have superimposed lines to better understand the electronic structure. Two different Dirac cones are observed, corresponding to R5 and R5' rotational domains (green lines). Depending on the vicinality or maybe on the surface quality, the doping of graphene varies from 320 meV to 250 meV, which also happens for Pt(111) [163]. In addition to the graphene cones of R5 and R5' domains, a cyan band is appreciated around 2.5 eV. This band corresponds to the saddle point of the π band of the R30 rotational domain that is superimposed with the R5 and R5' graphene bands. Close to the fermi level there is a Pt(111) bulk band indicated by a black line, that also superimposes with the graphene bands.

If we now focus on the discontinuities of the graphene band structure at the locations with no interference with other spectral features, we must concentrate on the discontinuity labeled "2nd gap" on fig. 4.4d-f. This region is shown in the Energy Dis-

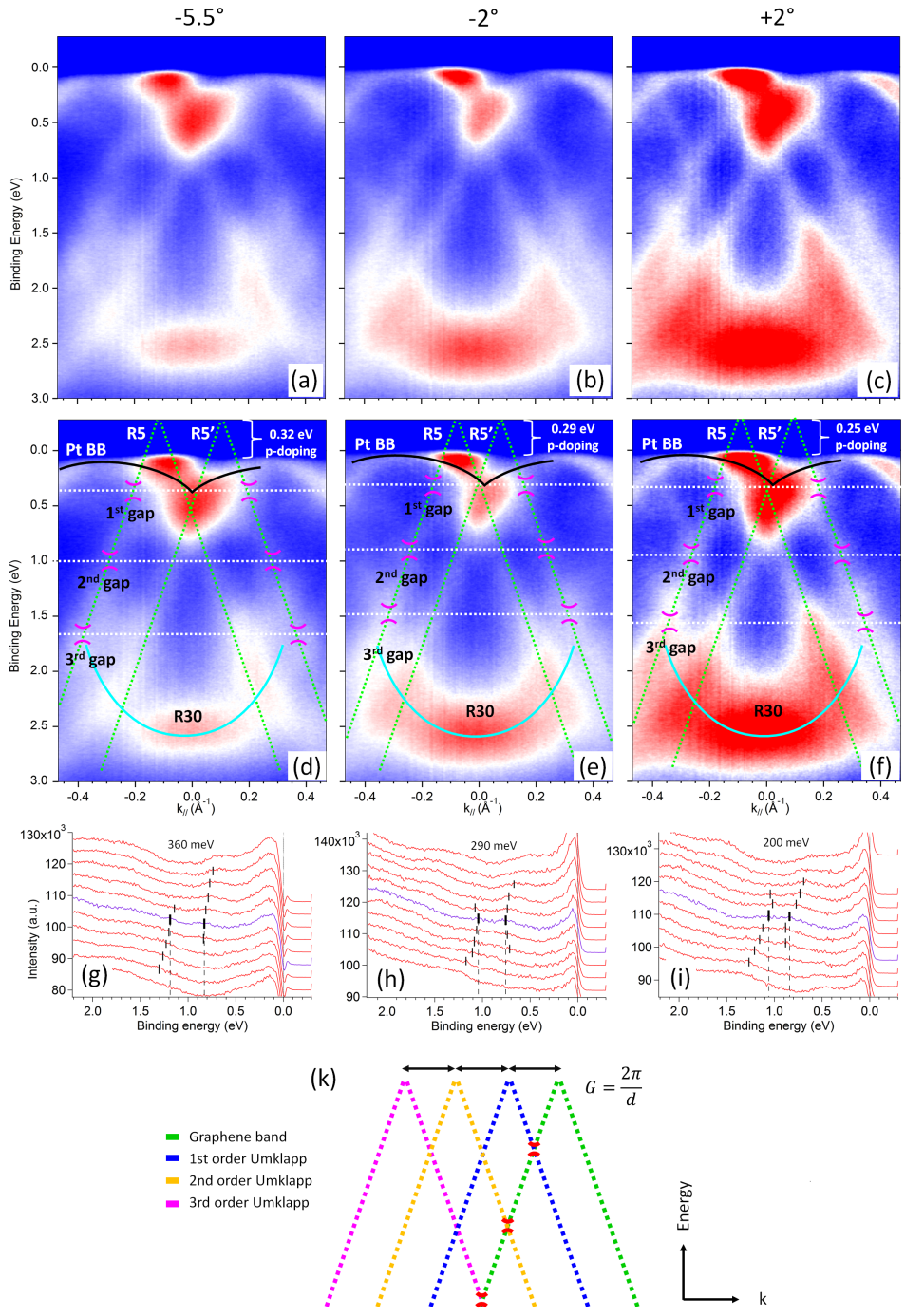

Figure 4.4: E(k) maps of graphene for the vicinal angles (a) $-5.5°$, (b) $-2°$ and (c) $+2°$. The same data with indications of the different spectral features are shown for vicinal angles (d) $-5.5°$, (e) $-2°$ and (f) $+2°$. The green bands show the R5/R5' rotational domains with a different p-doping at every vicinal angle. The cyan band at 2.5 eV is the saddle point of the π band from the R30 domain. The black band is a Pt(111) bulk band. The pink features mark the three gaps due to the crossing between the main band and the Umklapps. (g)-(i) EDC curves showing the gap opening of the second band gap. (k) Scheme of Umklapps bands due to the superperiodicity induced by the step arrays.

tribution Curves (EDC) in panels g-i. The black lines follow the maxima of the bands, showing the folding of the bands and consequently, a band gap opening (360 meV, 290 meV and 200 meV). Fig. 4.4k presents a scheme showing the origin of this band gap. Due to the superperiodicity introduced by the nanostructured substrate, a first order Umklapp band (or replica band) appears shifted by $G = 2\pi/L$, being L the spatial periodicity of the system. The same process occurs for the second and third order Umklapp bands, that are shifted by $2G$ and $3G$ respectively. The band gaps are originated at the crossing between the main graphene band and the Umklapp band. The 2nd bandgap corresponds to the crossing between the 2nd order Umklapp and the main graphene band. Other gaps are expected for crossings with the first and third order Umklapp, as indicated in fig. 4.4d-f. They are however less visible due to the proximity to platinum bulk bands or to the R30 graphene band. The E and k location of this gap changes with the vicinality. If we trace a line through the band gap energy, there is a shift from one surface to the other. There is also a shift in the k position where the band gap appears, meaning that the G vector depends on the vicinal angle. Indeed, the periodicities associated to the G vector observed in ARPES are 3.8 ± 0.9 nm ($-5.5°$), 3.9 ± 0.9 nm ($-2°$) and 4.5 ± 0.9 nm ($+2°$). These values correspond roughly to half of the periodicity found by LEED and STM, as also observed for Gr/Ir(332) and in the magnetic properties of faceted systems [169].

4.3 Dirac-hamiltonian model on Gr/multivicinal Pt(111)

The Dirac-Hamiltonian model can be applied to graphene on curved Pt as for Gr/Ir(332), allowing to reproduce the experimental ARPES bands and to calculate the potential barrier strength at the different vicinal arrays. Fig. 4.5a shows the main parameters used in the Dirac-hamiltonian model for continuous graphene under a periodic potential. The periodicity is given by $l = a + b$, where a is the width of the main facets at the surface, either the (111) terraces or the step-bunched facets and b is the limit between these two regions (of usually a few angstroms wide) and is where the potential barrier is found. The fermi velocity in all the vicinalities should correspond to the theoretical one, so $v_a = v_b = v_f$. The doping V_a and V_b for regions a and b changes with the vicinal angle (320 meV, 290 meV and 250 meV for $-5.5°$, $-2°$ and $+2°$ respectively). A sizable gap opening in the boundary between the terraces and the step bunching (b) mimics the potential barrier, therefore $\Delta_b = \Delta$, while everywhere else $\Delta_a = 0$. We again find the numerical solution of eqns. 3.14, 3.15 and 3.16 in the region of interest around the

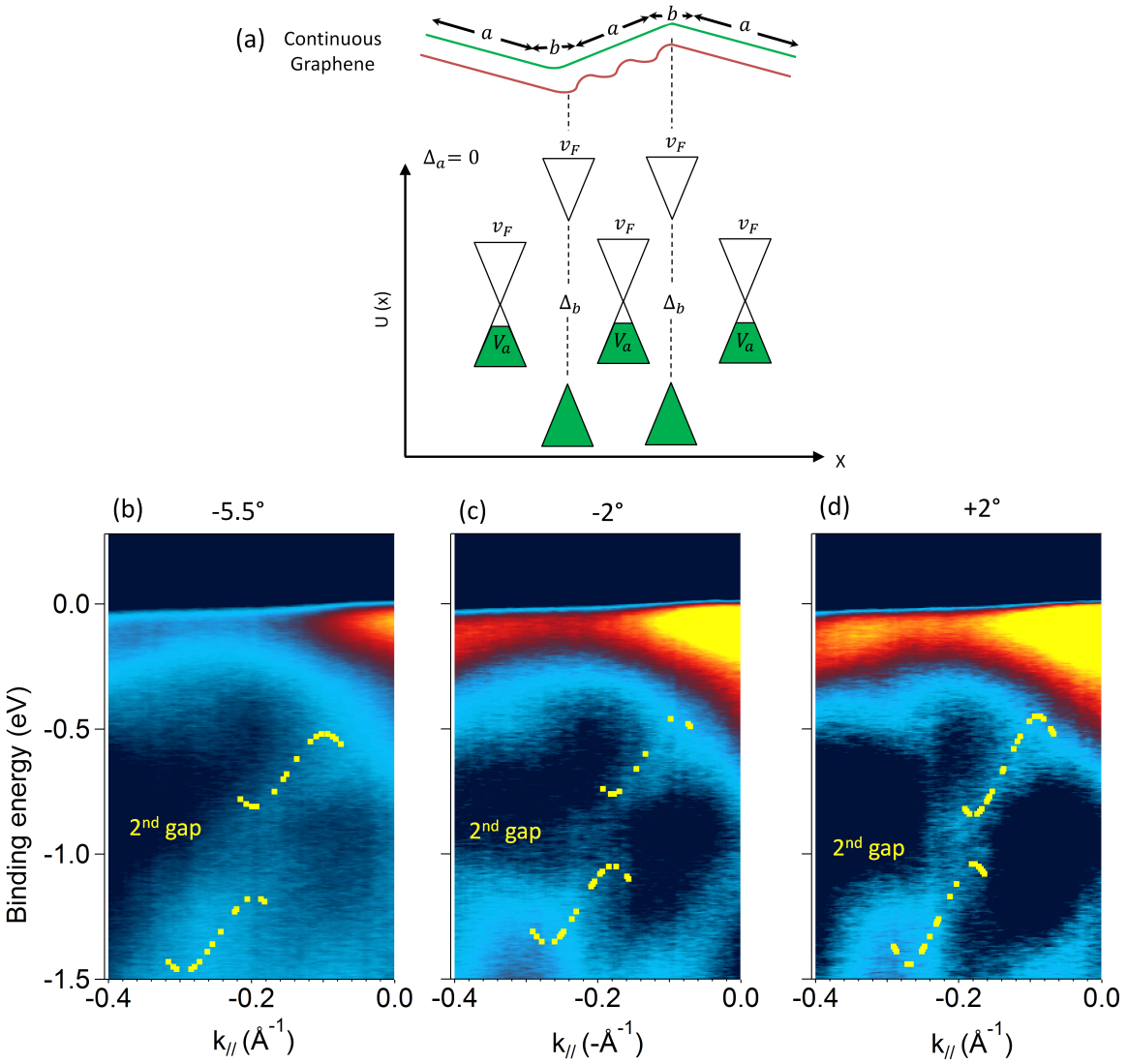

Figure 4.5: (a) Physical representation of the parameters on the two-dimensional Dirac-hamiltonian model for graphene under a periodicity $l = a + b$, where a is the average width of the (111) terrace or the step bunching facet and b is the junction of a few Å wide. The fermi velocity is preserved on both regions ($v_a = v_b = v_f$). The doping on regions a and b is 320 meV, 290 meV and 250 meV for vicinal angles $-5.5°$, $-2°$ and $+2°$ respectively. A gap in region b mimics the potential barrier at the limit between terraces and step bunching ($\Delta_b = \Delta$), while no gap is present in region a ($\Delta_a = 0$). Superimposed yellow bands obtained from the Dirac-hamiltonian model on top of the ARPES map for vicinal angles (b) $-5.5°$, (c) $-2°$ and (d) $+2°$. The calculated bands correspond to the parameters: (b) $a = 3.0$ nm, $b = 0.2$ nm and a potential of 3.35 eV Å; (c) $a = 3.3$ nm, $b = 0.2$ nm and a potential of 2.8 eV Å; (d) $a = 3.3$ nm, $b = 0.2$ nm and a potential of 1.8 eV Å, that reproduce the gap openings of 360 meV, 290 meV and 200 meV respectively.

second gap opening. We are then able to reproduce the ARPES dispersions, as shown on fig. 4.5b-d with a different color scale than fig. 4.4. The model is shown in yellow, where the gap is reproduced with 3.2 nm and 3.2 eV Å for −5.5° (panel b), 3.5 nm and 2.8 eV Å for −2° (panel c), and 3.5 nm and 1.8 eV Å for +2° (panel d).

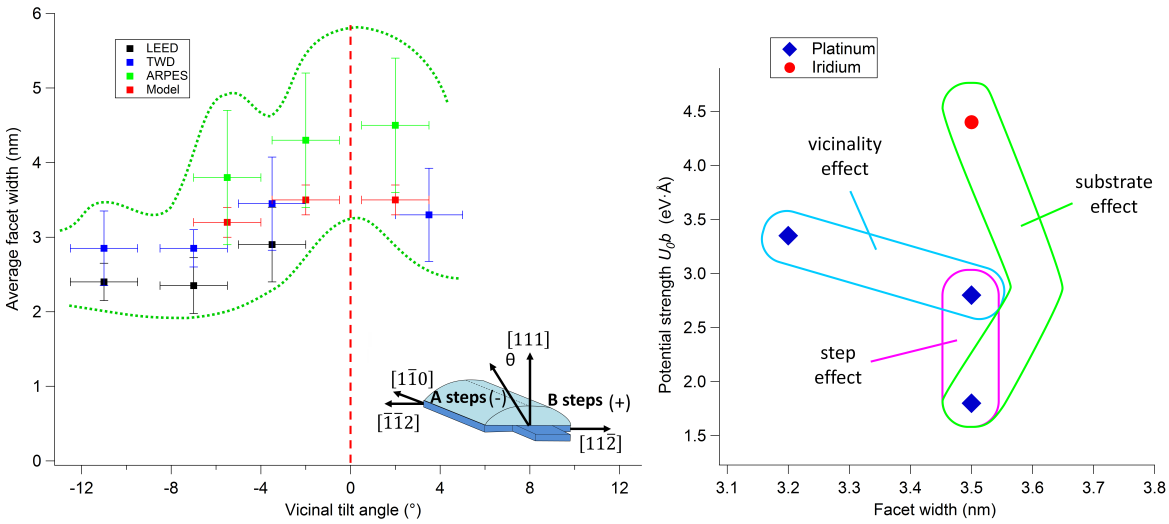

Figure 4.6: (a) Periodicity vs. vicinal angle (see the inset for the angle reference) as calculated by various techniques (LEED, TWD in STM, ARPES) and the Dirac-hamiltonian model. The trend is highlighted by the two enveloping green curves. The periodicity at the Pt(111) surface is not shown due to the absence of preferential orientation. (b) Calculated potential strength ($U_0 b$) vs. vicinal angle for the three angles on the multivicinal platinum crystal and on Ir(332). The pink enclosing corresponds to periodicities of 3.5 nm on A- and B-step side (−2° and +2° respectively). The green enclosing corresponds to periodicities of 3.5 nm on B-steps side on platinum (+2°) and iridium (+11°). The blue enclosing corresponds to periodicities 3.5 nm and 3.2 nm (−5.5° and −2° respectively) on the A-steps side.

Fig. 4.6a summarizes the results. The experimental periodicity as a function of the vicinality are shown, both those obtained experimentally (black, blue, green) and via the Dirac-hamiltonian model (red). The average facet width decreases when increasing the vicinal angle as we move away from the Pt(111) surface, as represented by the green enveloping lines. The potential strength as a function of the average terrace width for platinum is plotted on fig. 4.6b (blue diamonds). The results of Ir(332) are also included (B-steps, vicinal angle of +11°, represented by the red circle). By comparing two different terrace widths on platinum with the same step termination (blue enclosing on fig. 4.6b), it can be appreciated that the potential strength increases for smaller terrace widths, suggesting the possibility of reaching total confinement for smaller terraces, as observed in vicinal surfaces of Au [151]. If we now compare to the potential

induced for the same terrace width but different step type (pink enclosing on fig. 4.6b), we notice almost a doubling of the potential strength for A steps, probably favoring a higher coupling between the graphene and the substrate. Finally, if we compare the potential as a function of the substrate with same average terrace width and B-step edge (green enclosing on fig. 4.6b), we see that the potential strength greatly increases on iridium, probably due to the smaller graphene-substrate distance.

4.4 Conclusions and perspectives

We have modified the electronic properties of graphene by growing it on a nanostructured vicinal substrate. We have explored the effect of both A-steps and B-steps at vicinal angles between $+16°$ to $-16°$ with respect to the [111] surface normal. We have performed a study of the influence of the vicinality on the potential barrier strength both experimentally and by modelization. In detail, with this study we have understood:

- The growth and the structure of graphene via CVD on a curved Pt crystal:

In our growth conditions, for coverages close to the monolayer, we have grown a continuous layer of graphene. There are four main graphene rotational domains, namely R30, R5 and R5' as well as other domains corresponding to rotations between 15° and 45°, as indicated by arcs in LEED. It has been observed that the quality of the step array decreases far away from the [111] direction. Moreover, the side with A-steps results in more homogeneous step arrays, while most of the side with B-steps presents wiggly edges, giving rise to non-homogeneous structures.

- The effects of the structured substrate on the graphene electronic band structure:

We studied the electronic properties of graphene in different vicinal surfaces by ARPES. We observed there band gaps differing in their amplitude and their (E,k) position. By combining STM and ARPES results as an input for a Dirac-hamiltonian model, we explain the observed band gaps. The origin of the gaps comes from the superperiodicity induced by the step array. The modeling allows to retrieve the potential strength at the junctions between the (111) terraces and step bunching that leads to partial confinement on graphene and a band gap opening. The study of the confinement as a function of the vicinal angle allows to relate the structure to the confining potential.

The potential strength increases roughly as a function of the vicinal angle. Moreover, we observe a different behavior depending on the step edge, as there is a difference in the potential between A- and B-steps. Additionally, the potential strength greatly changes in iridium or platinum, indicating an important contribution from the interaction between graphene and the substrate. Finally, we observe how it is possible to control the potential by changing the periodicity of the nanostructuration.

Exciting perspectives appear from our study. Discontinuous graphene nanoribbons could probably be achieved with lower ethylene dosages. Also, the stability of B-steps could be improved by changing the growth parameters leading to higher confining potentials. Finally, other surfaces with different vicinal angles and orientations deserve to be explored, such as the (311) (vicinal angle of 18.43° towards the $[\bar{1}10]$ direction with respect to the [111] direction), where discontinuous growth of graphene is expected to happen.

Chapter 5

Gap opening on graphene nanoribbons on SiC

We have previously considered the tailoring of the electronic properties of graphene on a noble metal surface via the nanostructured substrate consisting of a regular step array. In this chapter, we will focus on the engineering of the electronic properties of graphene on SiC on an artificially induced nanostructure. Artificial graphene nanoribbons produced from a procedure combining lithography and annealing-induced growth will be studied. While the lithographic procedure allows to locate the nanostructure at will, the subsequent annealings allow to grow graphene at the selected locations with edges in their minimum energy configuration [170]. The so formed graphene nanoribbons system have been demonstrated to exhibit metal-semiconducting-metal junctions [89], and although it was stated that the origin of the wide semiconducting behavior was curved graphene, this remains to be clarified. With this goal, we combined Scanning Tunneling Microscopy (STM) with high-resolution Scanning Transmission Electron Microscopy (STEM) in different modes (Bright-Field (BF), Low- and High-Angle Annular Dark-Field (LAADF, HAADF)) as well as local Electron Energy Loss Spectroscopy (EELS). The STEM analysis required the development of a thinning method for the delicate sample with a nanoribbon array, where the main information is located in the few last atomic layers. This work is a collaboration between the Université Paris Sud, Georgia Tech, the Université de Lorraine and the Soleil Synchrotron.

5.1 Graphene sidewall nanoribbons and band gap

Tailoring graphene's shape to nanometric distances should open a band gap [29,31,49, 61,82]. However, the experimental realization of a graphene nanoribbon that possesses high mobility of a graphene layer is a challenge, as rough edges act as scattering centers, inducing localization and transport gap [72, 73, 171–173]. Previous studies have suggested that graphene nanoribbons grown on lithographically pre-structured SiC substrate [170] should allow to obtain smooth edges. Graphene grown on SiC has the advantage of lying on a technological substrate that can easily be implemented in existing devices. In order to open a band gap here, a solution is to rely on quantum confinement [12, 13].

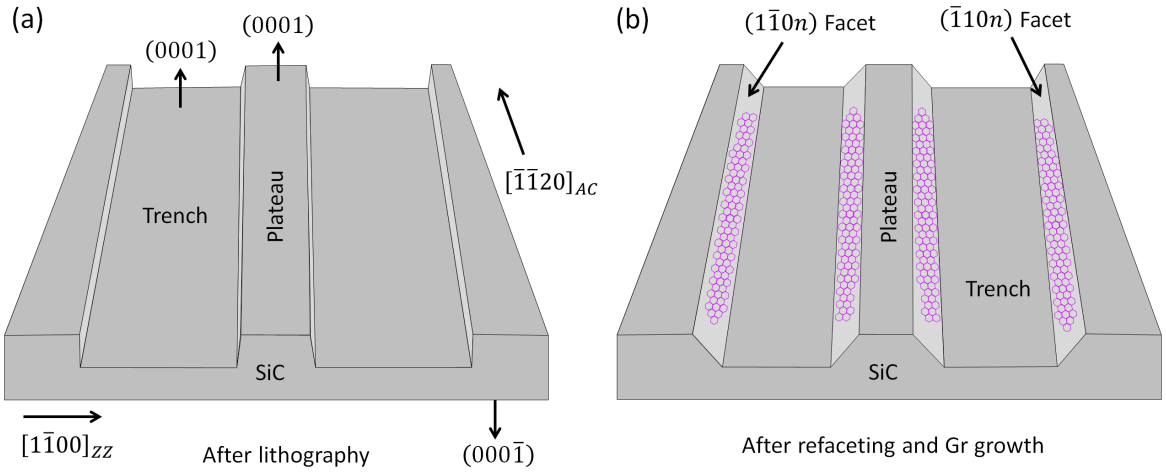

Figure 5.1: (a) 4H-SiC(0001) wafer after lithography of deep trenches parallel to the $[\overline{11}20]$ direction of SiC to produce armchair nanoribbons. The perpendicular $[1\bar{1}00]$ direction of SiC that produces zigzag nanoribbons is also shown. (b) Array of graphene nanoribbons through the stabilization of the vertical $(1\bar{1}00)$ and $(\bar{1}100)$ walls into the stable $(1\bar{1}0n)$ and $(\bar{1}10n)$ sidewalls after a first annealing. A second annealing promotes the nanoribbon growth on the sidewalls.

The group of Walt de Heer (Georgia Tech) has developed an original approach to grow ribbons that should present smooth edges. The procedure is sketched in fig. 5.1. Lithography first creates trenches that are the seeds for nanoribbon formation. In our case we need a ribbon array to easily measure in photoemission (to average over a large number of nanoribbons) or to easily locate the regions of interest on the microscopies. Panel (a) shows the lithographed array of trenches etched in 4H-SiC (0001) parallel to the direction $[\overline{11}20]$ of SiC for armchair nanoribbons (or the perpendicular $[1\bar{1}00]$ SiC direction for zigzag nanoribbons). The patterned substrate is annealed at 1100°C for

30 min, followed by a second annealing at 1525°C for a few minutes in a confinement controlled sublimation furnace [89, 170, 174]. The first annealing step recrystallizes the vertical $(1\bar{1}00)$ and $(\bar{1}100)$ walls into the stable $(1\bar{1}0n)$ and $(\bar{1}10n)$ facets, respectively. The final high-temperature growth step produces graphene, as the graphene growth rate is slower on the SiC(0001) facet than on the $(1\bar{1}0n)$ and $(\bar{1}10n)$ facets. Graphene appears in these sidewall facets and therefore ribbons grown here are called "sidewall nanoribbons". The resulting sample consists of an array of faceted mesa shapes, as shown in panel (b). Both the (0001) plateaus and trench bottom widths can be varied independently and the height difference between plateaus and trenches can be also tailored at will. The height difference depends on the initial lithographic process and controls the width of the graphene nanoribbon that lies on the sidewall between the plateau and the trench. Because of the orientational epitaxy of graphene grown on SiC(0001), the edge of the ribbons can be tuned. This ability to tailor the width and edge of the ribbons opens up the possibility of tuning their electronic properties in a way that is compatible with mass production. In this study, we mainly focus on graphene nanoribbons with trench walls etched parallel to the $(1\bar{1}00)$ orientation, that is, armchair edge graphene ribbons. In our case, the trenches are 30 to 35 nm deep and produce 40 nm wide nanoribbons that exhibit exceptional ballistic transport up to 15μm at room temperature and also present a wide bandgap at a location to be discussed [86, 89].

Within the framework of the collaboration with Edward Conrad at Georgia Tech and the Cassiopée beamline at Soleil Synchrotron, the arrays of sidewall nanoribbons have been studied by ARPES to identify the location and band structure of these objects. The angular resolution of this technique allows to differentiate regions with different surface normal. Fig. 5.2 shows three different regions, their respective surface normal and band structure [89]. The normal of the flat SiC(0001) is taken as the reference normal (0°). Due to the geometry of the system and preliminary AFM studies performed before the ARPES measurements, it was estimated that the sidewall nanoribbons are found with a normal at $\sim 30°$. Between these two regions, there is a transition region with normals between 10°-25°, whose origin was proposed to be at the highlighted yellow areas both above or below the sidewall nanoribbon [89]. The band structure at every region can be probed at the graphene K-point associated to every surface normal. In order to probe correctly the angular range for every feature, the sidewall nanoribbon array was slightly overgrown, so that graphene would grow on SiC(0001) to serve as the reference for the measurements. Panel (a) shows the metallic

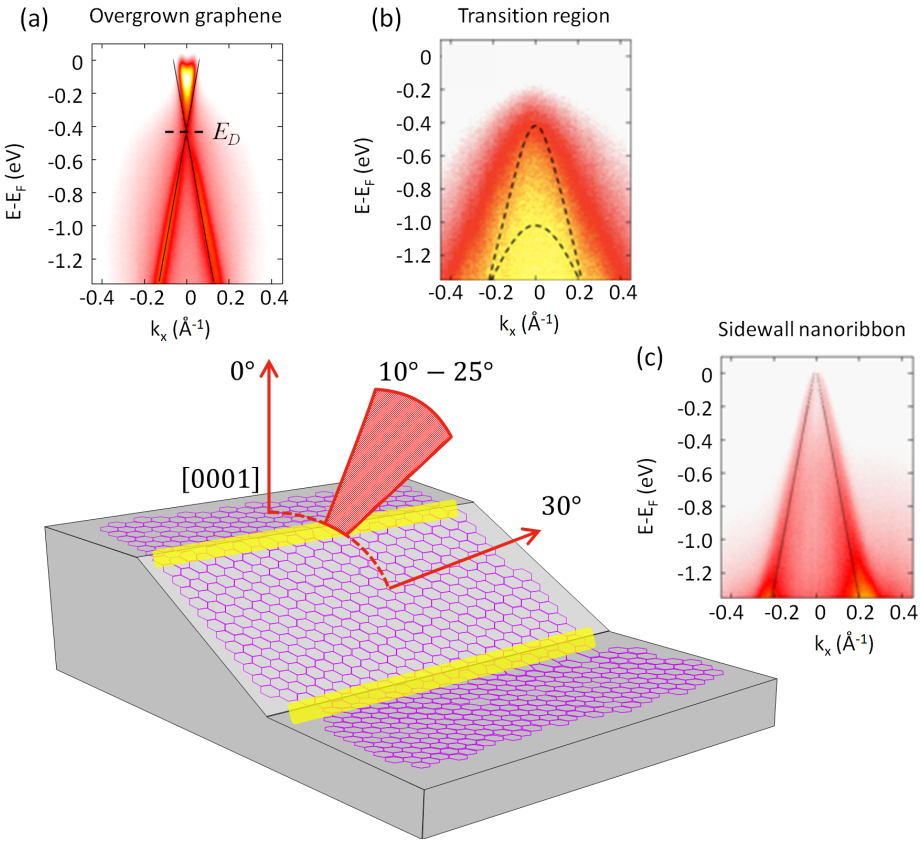

Figure 5.2: Array of slightly overgrown graphene armchair nanoribbons probed by ARPES. Three regions with different surface normal are shown: SiC(0001) (0°), sidewalls nanoribbons ($\sim 30°$) and a transition region (10°-25°) whose orientation is compatible with curved areas at the top or bottom of the sidewall nanoribbons (highlighted in yellow). (a) Metallic n-doped overgrown graphene on SiC(0001). (b) Transition region exhibiting a band gap of at least 500 meV. (c) Neutral metallic graphene indicative of decoupled graphene at the sidewalls [89].

n-doped graphene band, typical of a graphene layer on SiC(0001) [175]. When moving $\sim 30°$ from the reference, a neutral charged metallic graphene band is obtained (panel c). This neutrality suggests a decoupling between the sidewall nanoribbon and the substrate, contrarily to the n-doped graphene on SiC(0001), and may be due to the appearance of multilayers. On the other hand, when looking at the electronic structure of the transition region, a gapped band of at least 500 meV is obtained perpendicular to the trenches (panel b), whose origin was suggested to be located at the curved region (Fig. A.4 on the Appendix shows a cut parallel to the trenches). In order to understand why and where this large bandgap comes from, we need a detailed understanding of the nanoribbon structure. We have thus explored the atomic structure of epitaxial graphene sidewall nanoribbons firstly by STM.

5.2 Sidewalls: graphene location, edge quality and doping

As it was the first time that sidewall nanoribbon arrays were studied by scanning tunneling microscopy, we first looked at both armchair and zigzag sidewall nanoribbons, as a way to corroborate the structure orientation and the expected quality of the ribbons measured by ARPES. Fig. 5.3a-b show a 3D STM image of a sidewall nanoribbon out of an array of armchair and zigzag ribbons respectively. It is immediately noticeable that the sidewall facet on the armchair ribbon has straight edges, while the zigzag ribbon has wiggling edges. Studies on cylindrical SiC pillars relaxed by annealings show indeed that armchair edges are more favorable to be obtained than zigzag edges, specially for small pillars [174] (fig. 5.3c). For both cases, it seems that armchair edges are favored energetically and are thus more stable and easily obtainable than zigzag edges. In our case, it has been recently observed that for zigzag sidewall nanoribbons array, the sidewall presents a supplementary faceting into more stable armchair facets [176], consistent with the wiggling observed at the edges of zigzag sidewalls by STM.

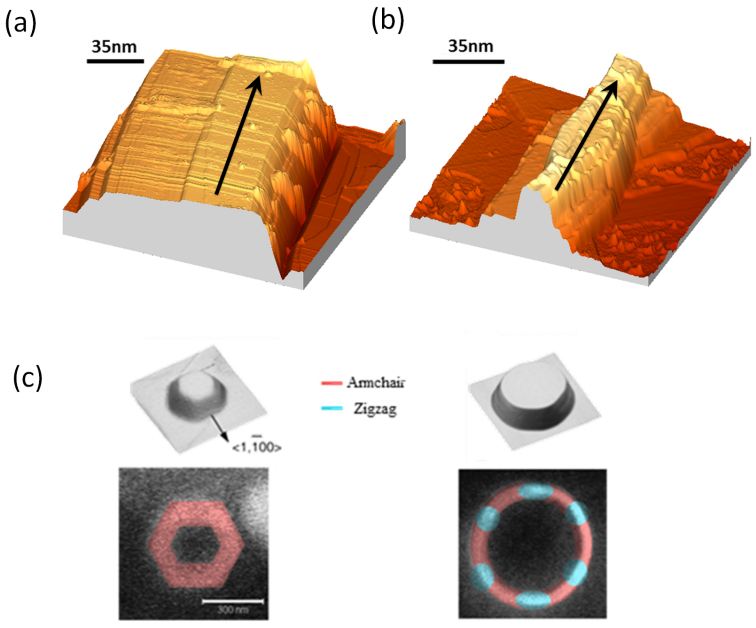

Figure 5.3: 3D STM images for (a) armchair [1.1 V, 0.7 nA] and (b) zigzag [-1.5 V, 0.25 nA] sidewall nanoribbons at large scale. The edge of the armchair sidewall nanoribbons is straight, while the zigzag refacets into more stable armchair directions. (c) Cylindrical SiC pillars of different sizes after an annealing that refacets the edges of the pillars. For the smaller pillar, armchair edges are preferred. For larger pillars, zigzag edges can be obtained mixed with armchair edges [174].

Further detailed scanning tunneling microscopy and spectroscopy performed on higher quality zigzag sidewall nanoribbons allow to compare and distinguish their electronic structure versus the bands obtained in ARPES for armchair sidewall nanoribbons. The STM data were acquired in collaboration with Muriel Sicot and Daniel Malterre at the Institut Jean Lamour, and analyzed with former post-doc Irene Palacio at Soleil Synchrotron. First, we identify and label all the interest areas, namely the SiC(0001) plateau (yellow) and trench (blue), the sidewall nanoribbon (green) and the upper (red) and lower (purple) transition areas (fig. 5.4). The atomically resolved images show a perfect graphene lattice on the sidewall region (panel d), whose orientation is zigzag, as shown by the superposed graphene lattice in panels (a) and (b).

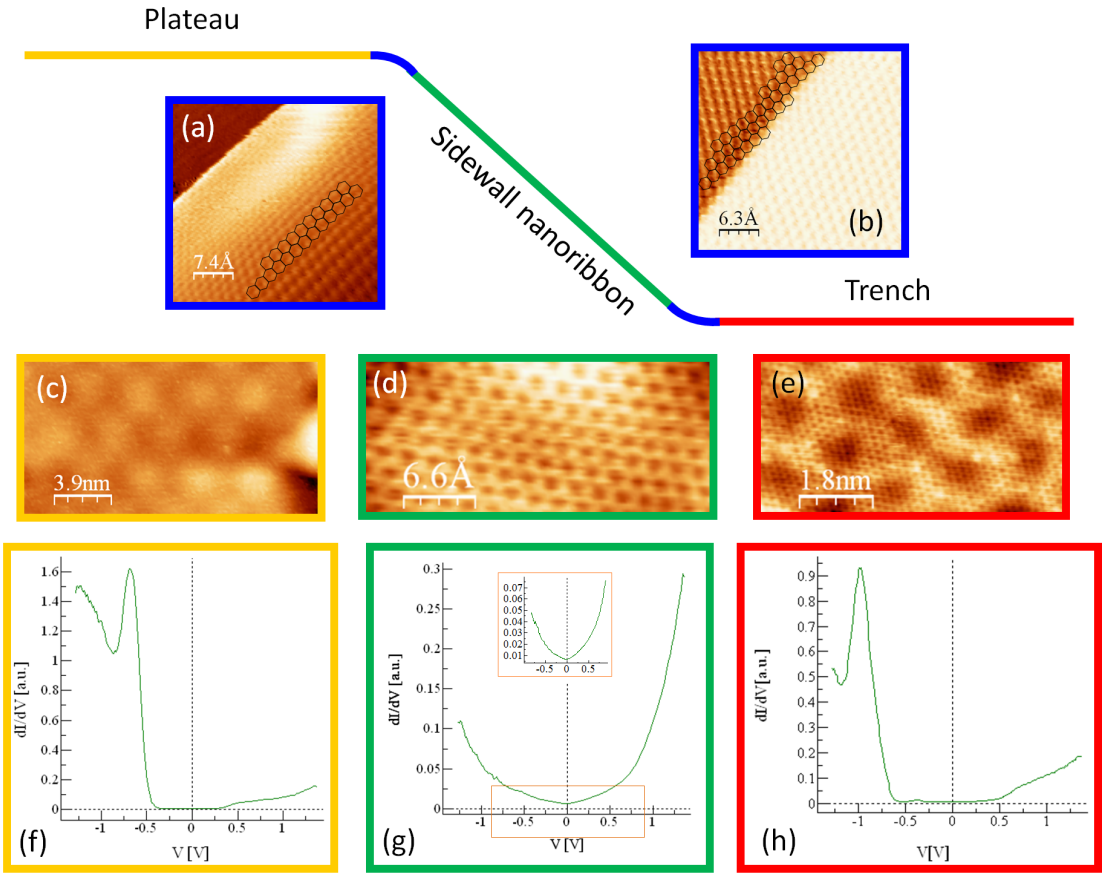

Figure 5.4: STM and STS performed on zigzag sidewall nanoribbons. Atomic resolution on the (a) upper [-1.5 V, 0.25 nA] and (b) lower [-1.5 V, 0.25 nA] edges. Moiré structures corresponding to a buffer layer on SiC(0001) on the (c) plateau [1 V, 0.25 nA] and (e) trench [-1.5 V, 0.25 nA]. The spectroscopic signal for the (f) plateau and (h) trench show the typical semiconducting behavior of the buffer layer. (d) Atomic resolved image on the zigzag sidewall nanoribbon [-1.5 V, 0.25 nA], whose orientation is preserved from edge to edge. (g) STS showing the characteristic spectrum of undoped graphene [86].

Panels c and e show a moiré structure typical of a single carbon layer on top of SiC(0001), known as the buffer layer that is semiconducting. Finally, a spectroscopic cartography was done at every 0.68 nm on a 70 nm by 67 nm STM image to obtain the local density of states. Panels f-h show the averaged spectroscopic signal corresponding to the plateau, sidewall nanoribbon and trench, where no band gap opening associated to graphene was found. The zigzag sidewall nanoribbon shows a neutral charged metallic behavior typical of decoupled graphene, similar to the previously observed behavior on armchair sidewall nanoribbons by ARPES. The plateau and trench display semiconducting behavior associated to the buffer layer.

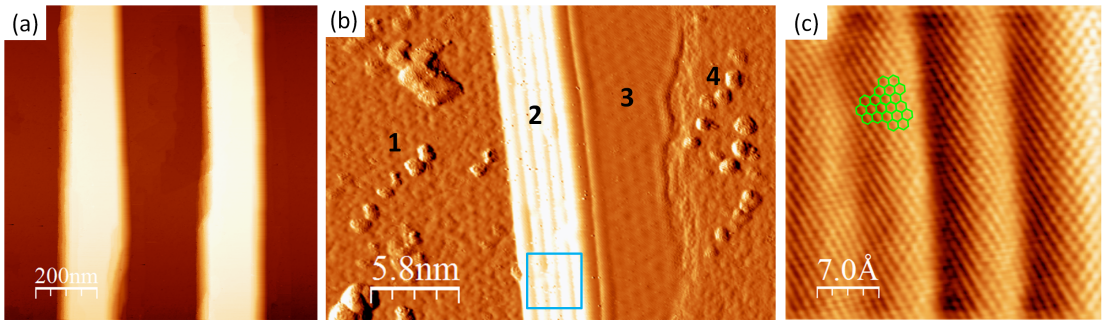

Figure 5.5: (a) STM large scale image showing the array of plateaus (bright areas), facets, and trenches (dark areas) [1 V, 0.5 nA]. (b) Zoom on a small $(1\bar{1}0n)$ step on constant current mode [1.1 V, 0.7 nA]. Four regions are distinguishable: Region (1) corresponds to the trench bottom where the graphene honeycomb is not well resolved (precursor region of the graphene growth). Region (2) is graphene growing along the facet up to the plateau and consists of multiple curves parallel to the facet. In region (3), graphene overgrows the facet onto the SiC(0001) plateau. The overgrown graphene extends to a boundary with the region (4), where another precursor state of graphene is observed. (c) Inset on the blue square on (b), where the ripple-like structure with a curvature of ~ 1 nm presents atomic resolution of armchair graphene.

We have also studied in detail armchair sidewall nanoribbons. Large scale topographic images show the coherence of the array composed of plateaus, facets and trenches (fig. 5.5a), where the edges are smooth and straight. As we zoom on the $(1\bar{1}0n)$ sidewall and in order to observe simultaneously the honeycomb corrugation and the strong topographic variations, we use constant current imaging (fig. 5.5b). The first region (1) corresponds to the trench bottom where the graphene honeycomb is not well resolved but the moiré periodicity is that of a buffer layer. The second region (2) is graphene growing along the facet up to the plateau and consists of multiple curves parallel to the facet. In region (3), due to the specific annealing temperature used in this sample, graphene overgrows the facet onto the SiC(0001) plateau. The

overgrown graphene extends to a boundary with the fourth region, where the buffer layer is observed again (4). The atomic resolution STM image on the transition region between the facet and the plateau (blue rectangle) confirms unambiguously the orientation of the edge. As shown by the superimposed honeycomb lattice on panel (c), it corresponds to an armchair ribbon. In region 2, a corrugation of $\sim$ 1 nm that forms a ripple-like structure that was unexpected and therefore was not considered on previous studies [89]. These results open the door to a better understanding of the origin of the observed band gap in ARPES.

5.3 Faceting at the boundaries of sidewall nanoribbons

STM has already identified an unexpected ripple-like structure, whose surface normal could be compatible with the gap observed in ARPES. In order to better understand these structures and their role in the eventual gap opening, it is necessary to study their bonding to the substrate. An ideal technique is STEM, provided that it is possible to study a sample where the structural information is contained in the fragile last atomic layer. To extract this information is necessary to perform a transversal side view of the atomic arrangement of graphene nanoribbons. It is thus necessary to thin the sample down to a 100 nm in order that electrons can go through. Fig. 5.6 shows the mechanism that allows the images to be obtained for the case of an $LaAlO_3/SrTiO_3$ interface [177].

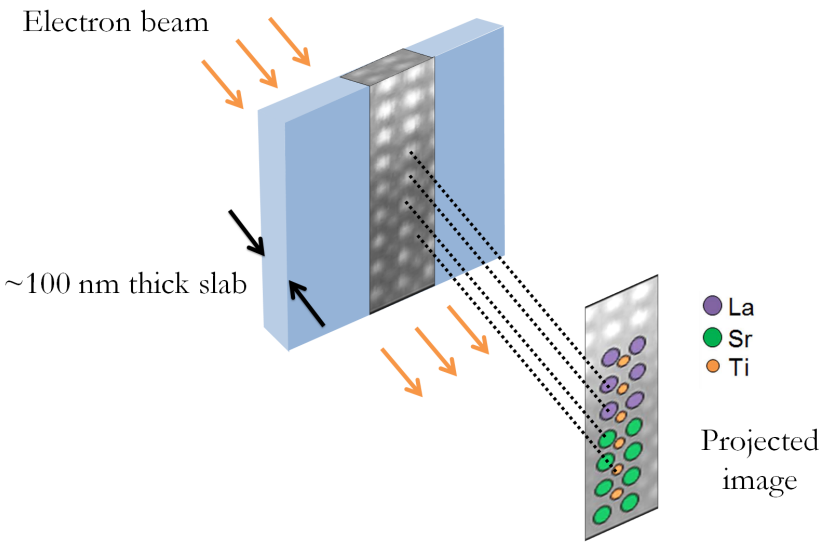

Figure 5.6: Ideal slab of some hundreds of nm thick obtained by the standard thinning procedure for a $LaAlO_3/SrTiO_3$ interface. The electrons pass through the sample and a projected image of atomic resolution is recovered on the CCD camera [177].

As the high voltage electron beam (orange arrows) passes through the sample, electrons are focused and interact with every atom along the slab. By projecting the outcoming electrons onto a CCD camera, we obtain an image showing the atomic positions of all the planes within the slab.

It was a real duty to perform such a sample preparation without destroying or modifying the last atomic layers. In collaboration with Alexandre Gloter and following a standard thinning procedure taught to me by the doctoral student Xiaoyan Li, I have developed a modified procedure to thin graphene nanoribbon samples at the Laboratoire de Physique des Solides at the Université de Paris Sud. The thinning process consists of three stages: resizing (fig. 5.7), mechanical polishing (fig. 5.8) and ion bombardment (fig. 5.9). At the resizing stage, the sample is cut in two halves to be glued together to enclose the graphene nanoribbons in the middle to protect them for further processing. Subsequently, the sample is further reduced in size to fit the STEM sample holders. Several stages of mechanical polishing with diamond grinding papers are performed until reaching some hundreds of nm width. Finally, the sample is bombarded with argon ions to gently erode the surface until reaching the final thickness of ~ 100 nm. The following gives a detailed description of each stage.

Resizing

A special sample holder for cutting samples is heated at 100°C. A drop of crystal silicon glue is deposited on it until it melts and the Gr/SiC sample is glued on it, lying on the SiC$(000\bar{1})$ surface, where no ribbons are present. The sample is then cut in two halves in the direction perpendicular to the trenches on the middle of the sidewall region containing the ribbons, as shown on fig. 5.7a. The two pieces are then removed from the cutting sample holder by melting most of the crystal silicon glue; the remaining glue is removed with ethanol. This process requires previous careful identification of the SiC facets and the direction along the trenches, as the samples are almost transparent. Next, epoxy is deposited on the SiC(0001) facets (where the ribbons are found) to glue the two pieces together to form a sandwich, as shown by the arrow on fig. 5.7a. The sandwich will protect the graphene nanoribbons during the thinning process. The sandwich is then kept under constant pressure at both ends by the arms of a spring press to eliminate any air bubbles inside the glue, while being heated for 1 hr on an oven at 100°C to finally let it slowly cool down overnight at the natural cooling rate of the oven. The sandwich is then cut perpendicularly to the trenches in slabs of 1 mm

by 1 mm by 2 mm, as shown on fig. 5.7b, which is a suitable size for STEM sample holders. We will obtain as many samples as slabs are cut.

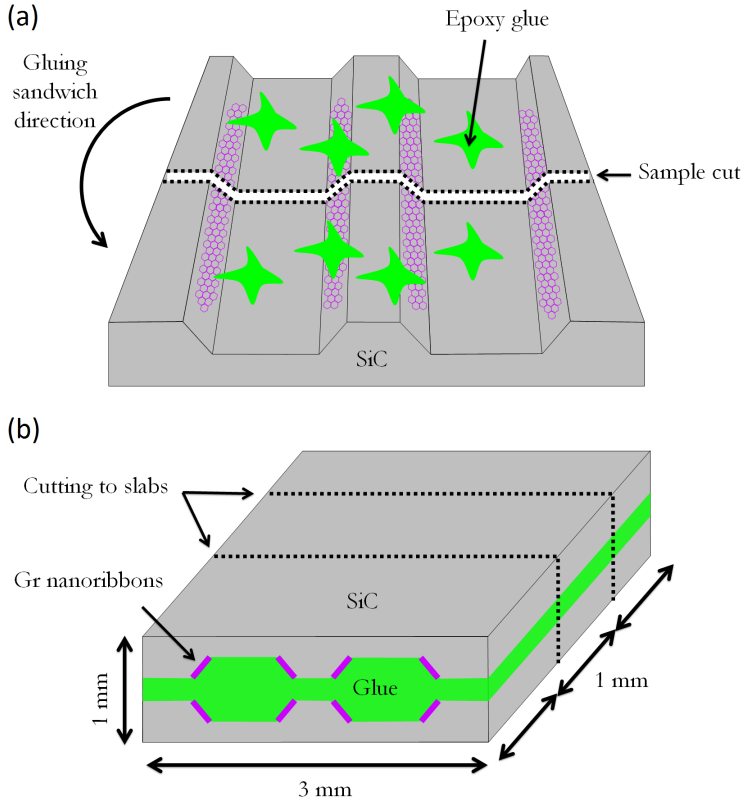

Figure 5.7: (a) The sample with graphene nanoribbons is cut in two pieces perpendicularly to the nanoribbons long direction. The two pieces are later glued together with epoxy (green patches). (b) The sample is further resized by cutting out slabs of 3mm × 1mm × 1mm from the previously formed sandwich, as shown by the dotted lines.

Mechanical polishing

It is necessary to polish the two surfaces of 1 mm by 3 mm until reaching a few hundreds of nm thickness. Fig. 5.8a shows a scheme of the initial slab and identifies the two faces to polish (A and B). The polishing is divided in two steps: (1) polishing and smoothing of face B to ensure that this face will remain glued to the support and (2), polishing face A until reaching a few hundreds of nm thickness.

On the first step, face A will be glued to the polishing support with crystal silicon. Face B will be polished with decreasing diamond grinding papers (15, 6, and 3 μm) at decreasing speeds from 30 to 20 rpm to avoid cracking of the surface. The polishing ends when the surface is visibly smooth at an optical microscope. The slab is then unglued

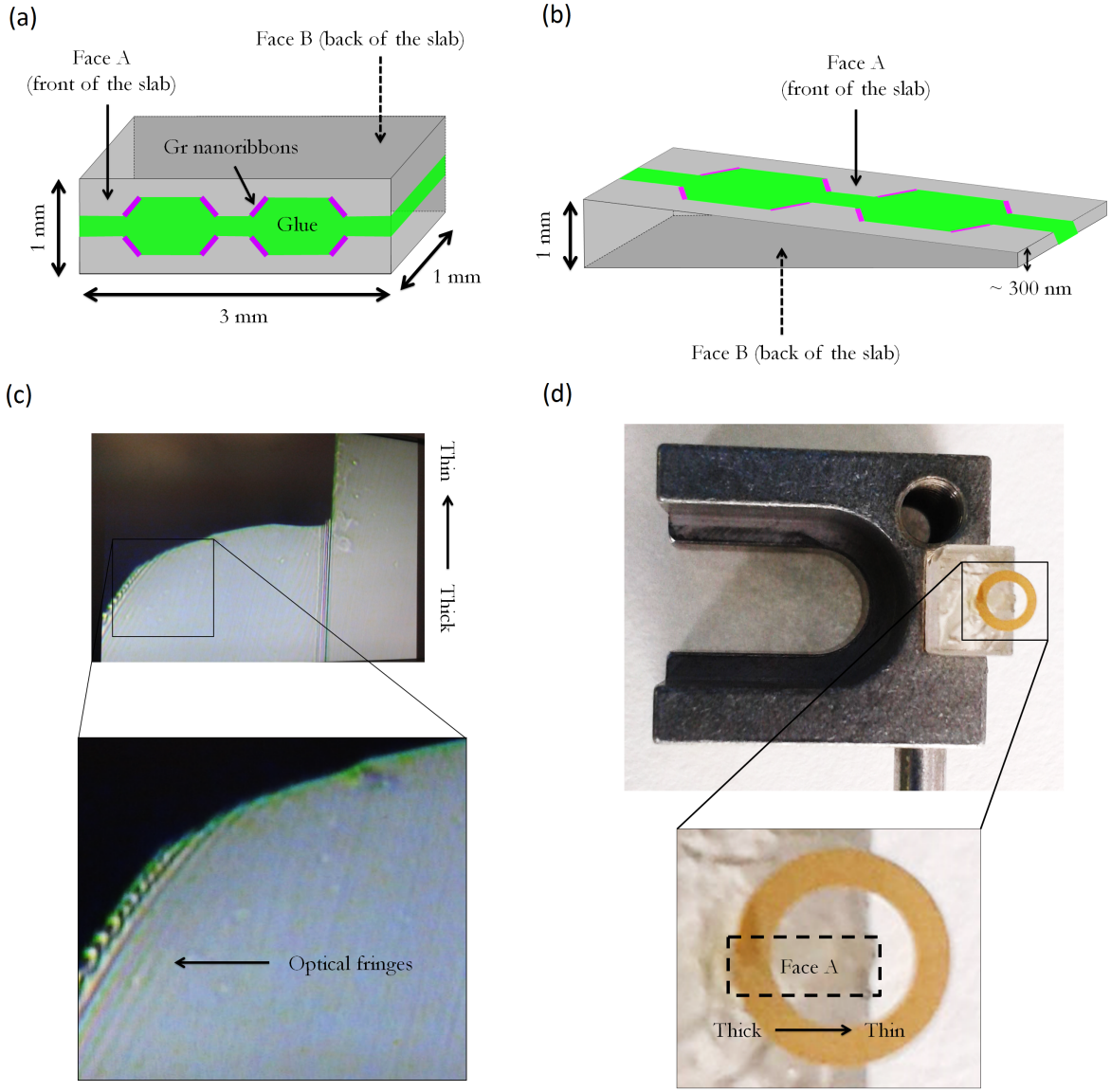

Figure 5.8: (a) Single slab where faces A and B are identified in order to perform further mechanical polishing. (b) Slab after thinning by different diamond grinding papers, where a 1° angle allows to obtain a wedge shape. The thicker end of the wedge is 1 mm thick, while the thin end of the wedge is ∼ 300 nm in width. (c) Optical microscope image of the obtained wedge sample, where a portion of the sandwich has been taken away by the mechanical polishing, however we can appreciate the ∼ 300 nm thick end of the wedge by the appearance of optical fringes (inset). (d) Thinned wedge nanoribbons sample glued to the Cu STEM grid. The thick part is glued to the edge of the grid, while the thin part will be suspended in the middle of the grid.

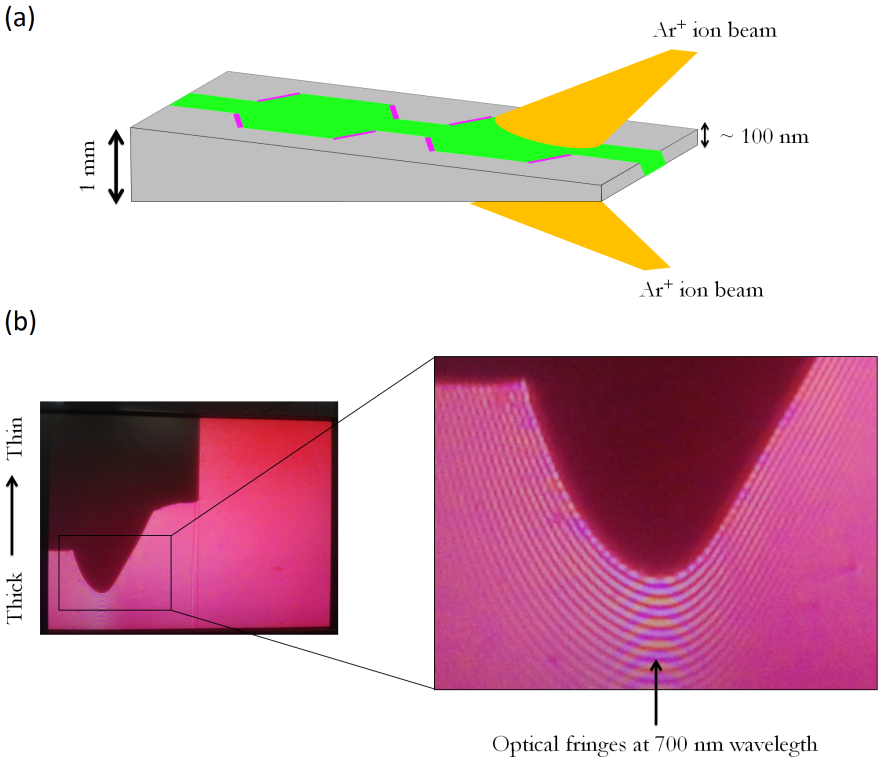

Figure 5.9: Graphene nanoribbons sample (3 mm × 1mm × ∼ 100 nm) is further thinned by ion bombardment, as shown by the further appearance of optical fringes monitored with a pink filter. The ion bombardment process is stopped when interference fringes appear on the nanoribbon area.

and turned to glue face B to the polishing sample holder. Face A is then polished with decreasing diamond grinding papers (15, 6, 3, 1 and 0.1 μm) at speeds decreasing from 30 to 10 rpm. A 1° angle between the sample surface and the grinding papers is introduced to induce a thickness gradient on the sample. The thickness gradient allows to thin just one end of the sample, while the other end remains thick enough to be glued to the TEM grid. The process is stopped when interference fringes appear on the thinnest part of the sample, indicating that the sample produces interference with visible light, i.e. it has a thickness of around a few hundreds of nm (fig. 5.8c).

At this stage, the sample is ready for ion bombardment. The sample is then glued to a Cu TEM grid with a diameter of 3.05 mm, as shown on fig. 5.8d. A drop of liquid glue is poured on the thicker part of the sample, and the grid is positioned to suspend the thinner part on the center of the grid. The sample is then dried 24 hours under a lamp. A bath of acetone is used to dissolve the crystal silicon glue to detach the slab/grid system from the quartz support and transfer it to the ion bombardment machine.

Ion bombardment

Ion bombardment is performed on a precision ion polishing system at −174°C. Two ion guns focused at the sample center with a grazing angle of 6°, as shown on fig. 5.9a. We monitor the thinning by the appearance of interference fringes with a pink filter. In the case shown in fig. 5.9b, fringes appear first on the outer part of the slab, spreading to the center of the sample towards the glue and graphene nanoribbon area. At this point the sample is thin enough to be studied by STEM. A scheme of the sample after the thinning process is shown in fig. 5.10. The slab of ∼ 100 nm width is composed of a sandwich of graphene nanoribbons surfaces contacted by a glue that protects them. The electron beam of the STEM (orange arrows) is sent and the projection of the atoms is recovered on the CCD camera.

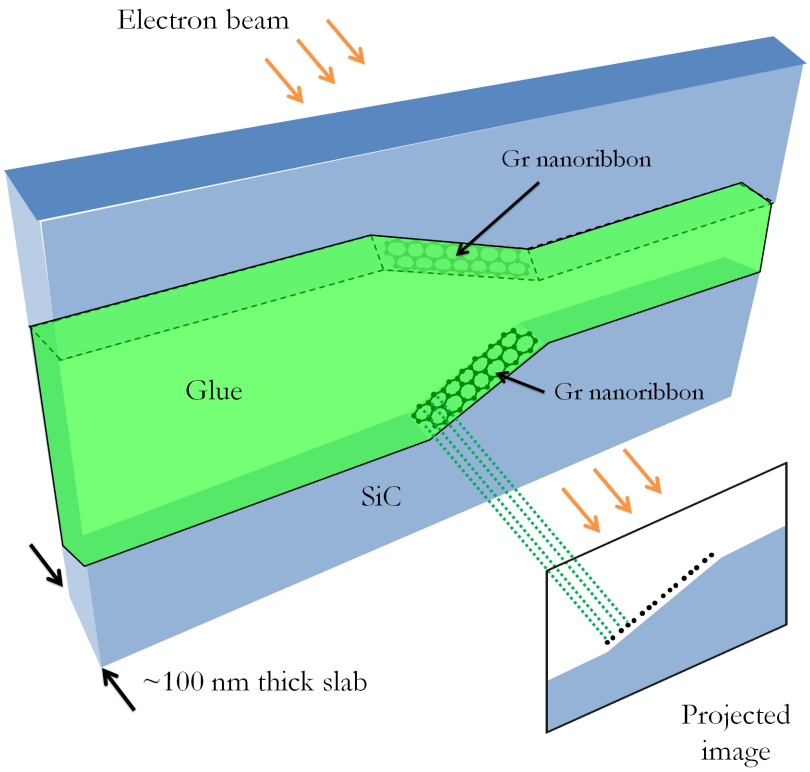

Figure 5.10: Graphene nanoribbons/SiC after the thinning process. Two portions of graphene nanoribbon areas are sandwiched together by a glue layer. Once the STEM electron beam (orange arrows) crosses the slab, the lateral projection of the atoms is recovered on the CCD camera.

The following STEM measurements were carried out in collaboration with Alexandre Gloter at the Laboratoire de Physique des Solides at the Université Paris Sud. Depending on the required information, HAADF, LAADF or BF modes may be more

suitable. The STEM-HAADF imaging mode is more sensitive to the atomic structure of the SiC substrate. The STEM-LAADF is more sensitive to carbon based material thus enhancing the contrast of the graphene ribbons and showing the presence of a single graphene layer. The BF-mode uses absorption of the sample to give a contrasted image.

A cross sectional STEM image of the sidewall ribbon array is shown on fig. 5.11a, where we can identify the substrate [0001] and $[1\bar{1}00]$ directions as well as the $(1\bar{1}0n)$ sidewall facet. Panel (b) shows an atomically resolved STEM-BF image with a large field of view of the sidewall where two main families of facets are observed. The central part of the sidewall (tens of nanometers wide) has a normal rotated ca. 30° with respect to the SiC (0001) plane (corresponding to a $(1\bar{1}07)$ surface). The top and the bottom part of the sidewall are composed of facets tilted ∼20° from the (0001) plane, i.e. to the $(1\bar{1}0n)_{n=9,10}$ facet, consistent with the ripple-like structure observed by STM.

A close up on the ripples of the $(1\bar{1}0n)_{n=9,10}$ facet is shown in panels c-d. The detail shows that the substrate presents small SiC(0001) miniterraces and minifacets due to the stabilization of the initial SiC facet during graphene growth [178]. The minifacets typically have a $(1\bar{1}05)$ orientation extending over 4 SiC bilayers along the [0001] direction, that is, the unit cell of the 4H-SiC polytype. Graphene grows continuously over the miniterraces and minifacets, but the distance to the substrate changes. The distance of the graphene layer to the miniterraces is 2.3 Å, a distance similar to the tightly bound buffer layer on the Si (0001) face (referred as coupled graphene in blue on panels (c) and (d)). On the other hand, a curved "floating" graphene layer is found on the minifacets (referred as decoupled miniribbon in green on panels (c) and (d)). Its distance to the substrate is extremely high (4.0 Å), which could cause an electronic decoupling from the SiC, and forms a narrow armchair-edge miniribbon running parallel to the SiC step edge.

While analyzing the entire $(1\bar{1}0n)_{n=9,10}$ facet (panel (e)), we can see that graphene in green runs continuously from the sidewall to the ripple-like structure until arriving to the SiC(0001). At the $(1\bar{1}07)$ sidewall we find a large armchair nanoribbon larger than 20 nm with an average distance to the substrate of ca. 3.5 Å, which is much larger than the 2.3 Å distance for the tightly bonded buffer layer [179–181]. This clearly indicates that the sidewall nanoribbon is essentially decoupled from the substrate (or delaminated [182]), apart from sparse more or less regularly spaced anchored points. Note that the $(1\bar{1}07)$ and $(\bar{1}107)$ surfaces are nonpolar [183], which may explain why the nanoribbons are charge neutral on ARPES [86, 89]. On the other hand, at the

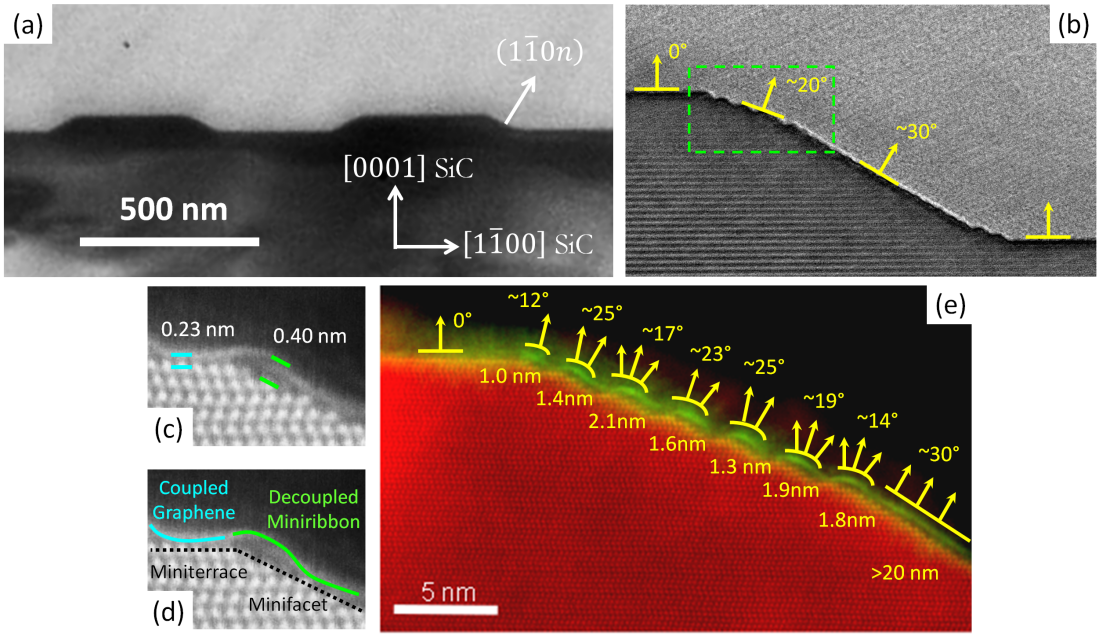

Figure 5.11: (a) Cross sectional TEM image of the array of ribbons with a distance between plateaus of 300 nm. (b) Zoom on the (1$\bar{1}$0n) facet, showing two families of facets. The first is the extended (1$\bar{1}$07) surface where the armchair sidewall nanoribbon is grown at a normal rotated $\sim$ 30° from the SiC normal, and the second is a ripple-like structure in the upper and lower part of the extended facet at normals rotated $\sim$ 12-25° from the SiC normal. (c)(d) A zoom on one of the ripple structures shows a faceting of the SiC substrate into miniterraces and minifacets. The distance of coupled graphene to the miniterrace is 0.23 nm, similar to the buffer layer on SiC(0001). The distance between the decoupled miniribbon and the minifacet is 0.40 nm, larger than on graphite, so a decoupling from the substrate is expected. (e) A zoom on the green square on panel (b) shows a colorized image where graphene is in green and SiC in red. A large armchair nanoribbon larger than 20 nm extends over the sidewall facet, continues upwards following the supplementary faceting of SiC (minifacets and miniterraces) until arriving to the (0001) SiC surface. The given angles and distances were calculated for the decoupled miniribbons. In average their normals vary from $\sim$ 12 to 25 ° and their width is between 1-2 nm.

$(1\bar{1}0n)_{n=9,10}$ facet the decoupled miniribbons have normals that vary from ~ 12 to 25°, corresponding to the normals observed in ARPES. Their width is between 1-2 nm.

These structural studies confirm the orientation of the sidewall facets that was determined by angle-resolved photoemission, as well as the presence of a sub-structure on the transition regions. Angle-resolved photoemission has observed a linear dispersion at the $(1\bar{1}07)$ extended facet. This is consistent with the STEM observation for the large central ribbon electronically decoupled from the substrate and whose width will not produce an observable gap. We also know that the transition regions with normal between [0001] and $[1\bar{1}07]$ exhibit a band gap of at least 500 meV, corresponding to the normals of the decoupled miniribbons. There are several possibilities for a band gap opening in these miniribbons. Uniaxial strain can open a gap in armchair ribbons when the strain is perpendicular to the edge [1,2] but in order to explain the experimental gap, bonds should be strained by an unphysical large value of more than 20%. Nevertheless, STEM images show that graphene in the miniribbons "floats" on the minifacets, that is, the graphene layer is able to relax any residual strain, which rules out a strain-induced gap. A more realistic possibility is quantum confinement, where the narrow 1-2 nm miniribbons could produce band gaps of 0.5 to 1 eV [15].

In order to confirm that the band gap observed by ARPES is effectively spatially located in the curved graphene miniribbons, we performed STEM-EELS measurements. We focus on the carbon K-edge corresponding to transitions between the C-1s core electron to the unoccupied states just above the Fermi level (fig. 5.12). The boundary between the plateau and the sidewall covered by a single continuous graphene layer is shown in panel (a). The buffer layer at the SiC top surface and three miniribbons are observed. Panel (b) is a zoomed image of the area boxed in panel (a) where spectromicroscopy measurements were performed. EELS spectra were collected with a spatial step of 0.04 nm and an acquisition time of several milliseconds. Spectra integrated in the boxes of panel (b) are characteristic of different regions (panel (c)): the buffer layer (1), the first miniribbon (2), graphene on the miniterrace (3) and bulk SiC (4). The spectrum from the miniribbon shows the π^* and σ^* peaks characteristic of graphene or graphite-like materials [182]. A similarity is observed on the spectra from the buffer layer and the graphene on the miniterrace, as these two regions have noticeable additional spectral intensity in between the π^* and σ^* peaks located ca. 1.3 eV higher in energy than the π^* (indicated by an arrow in spectrum 1 in panel (c)).

To isolate the additional features in the buffer and graphene on miniterrace, we have analyzed the main spectral components in the EELS spectra by using spectral unmixing

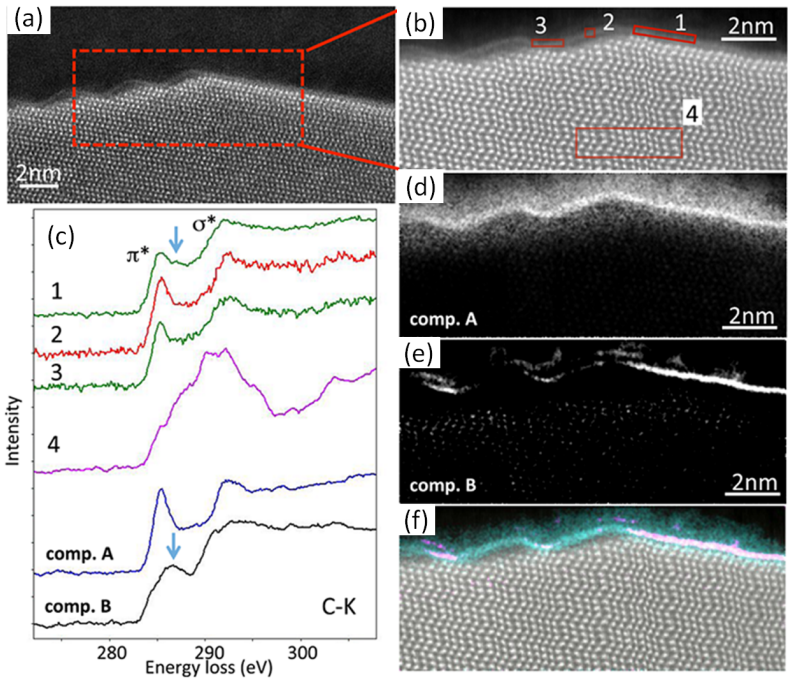

Figure 5.12: (a) STEM image of the region studied by EELS at the carbon K-edge. The region exhibits a graphene monolayer at the boundary between the plateau and sidewall. (b) Zoom of the red rectangle in (a) indicating the four regions chosen for STEM-EELS spectromicroscopy measurements in (c). (c) Raw spectra extracted from (1) the buffer layer, (2) the first miniribbon, (3) graphene on the miniterrace and (4) bulk SiC. Component A and B spectra represent the main spectral components related to the carbon layer at the surface of SiC. Spectra 1-3 show the features of component A (graphite-like), while only spectrum 1 and 3 show an additional feature marked by the blue arrow corresponding to component B (highly coupled graphene). (d) Spatial location of component A present on the single carbon layer. (e) Spatial location of component B, present on the semiconducting buffer layer and coupled graphene on the miniterraces. (f) Pseudocolor image where gray enhances the SiC and cyan highlights the decoupled miniribbons.

based on a Vertex component analysis [184], resulting in two spectral components A and B, shown in panel (c). Panel (d),(e) show the spatial distribution of components A and B respectively. Component A is observed all along the carbon atomic layer, and it is thus associated with graphene/graphite. On the other hand, the additional component B is only present when the carbon layer is strongly bounded to the SiC surface (i.e., either at the buffer layer or at the graphene on the miniterraces). ARPES measurements have indicated that the buffer layer has a small band gap with the presence of additional spatially localized in-gap states associated with the complex hybridization between the buffer layer and the SiC surface [185]. These peculiar electronic structures might be the origin of the additional spectral component B found in the buffer layer and

also on graphene at the miniterraces. Whatever the exact origin of this EELS spectral component B, it confirms that the electronic structure at both sides of miniribbons is different from that of pure graphene/graphite. To better visualize the difference in electronic structure, panel (f) shows a pseudocolor image where gray enhances the SiC, cyan highlights the decoupled miniribbons and white shows the buffer layer and graphene on the miniterraces.

5.4 Atomic origin of the band gap

In order to further explore the electronic structure of the miniribbons, we have investigated EELS spectra at higher resolution. Fig. 5.13a shows an STEM image on a bilayer graphene sample. Region 5 corresponds to the second layer on SiC(0001), clearly distinguished above the buffer layer and known to be metallic [180]. Region 6 corresponds to the miniribbons on a bilayer. The comparative EELS spectrum at both positions shows a different shape of the π^* and exhibits an energy shift of around 0.25 eV (Fig. 5.13b).

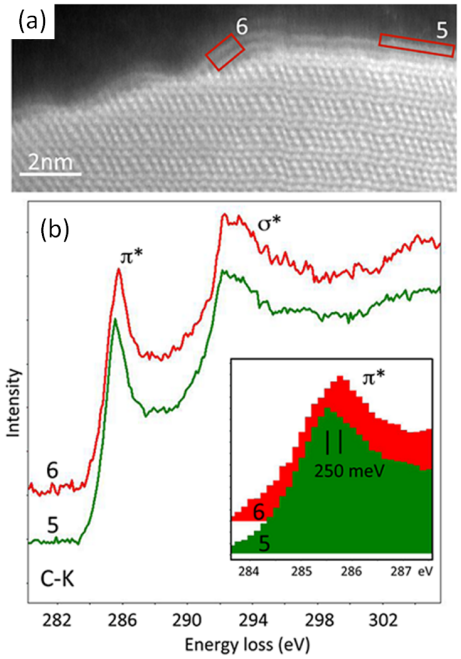

Figure 5.13: (a) STEM image use in EELS analysis at the carbon K-edge for bilayer graphene at the boundary between the plateau and sidewall. Boxes 5-6 indicate the regions where spectra have been extracted, namely the first metallic graphene layer on SiC and the decoupled miniribbons, respectively. (b) EELS spectra showing an energy shift to higher energy of ca. 250 meV of the π^* excitation for the decoupled miniribbon with respect to the metallic graphene.

A similar difference in π^* excitations has been reported between semiconducting and metallic nanotubes by XAS and EELS spectroscopy [186]. The observed energy shift thus confirms that the electronically decoupled miniribbons exhibit a band gap.

All these results demonstrate that the electronic properties of the sidewall graphene are significantly modified near the top and bottom edges of the facet. At these regions, a continuous layer of graphene follows the sub-faceted SiC structure (miniterraces and minifacets). The miniribbons on top of the minifacets are detached from the SiC while graphene on top of the minifacets is highly bonded to the substrate, behaving similarly to a normal buffer layer on SiC(0001). These buffer layer strips isolate the miniribbons in between, creating electronic confinement that could open a significant bandgap in the 1 - 2 nm miniribbons of $\sim$ 500 meV to 1 eV.

5.5 Band gap on the miniribbons by ab initio calculations

The band gap opening in the miniribbons that we have previously identified is further confirmed by the ab initio calculations performed by Alberto Zobelli at the Laboratoire de Physique des Solides. The surface corresponding to $[1, \overline{1}, 0, 10]$ at the top and bottom region of the sidewall have been modeled by a 1.7 nm thick SiC slab where the lower surface has been saturated by hydrogen atoms. The supercell periodicity has been chosen along the $[\overline{1}, \overline{1}, 0, 10]$ step edge direction in order to minimize the strain on the graphene ribbons. Three armchair graphene periods are accommodated over four SiC step periods leading to a graphene compression as low as 3.6%. This compression relaxes through a slight out-of-plane rippling of the miniribbons. A 2.9 nm wide graphene sheet is considered for the model, where 1.1 nm is located on top of the SiC miniterraces (buffer layer) and 1.8 nm is freestanding (miniribbons). The fully relaxed 806 atoms model is displayed in fig. 5.14b.

The projected density of states of the system is presented in fig. 5.14c. The buffer layer at the miniterraces has a projected density of states shifted with respect to the free-standing ribbons, which is in agreement with previous results on extended buffer layers [187,188]. The free-standing graphene region presents a local density approximation of the electronic gap of about 1 eV (panel (c)). This energy gap is of the order of magnitude of the expected gap for free-standing armchair ribbons with similar widths. The electronic behavior of the complex SiC/graphene heterostructure can be linked to

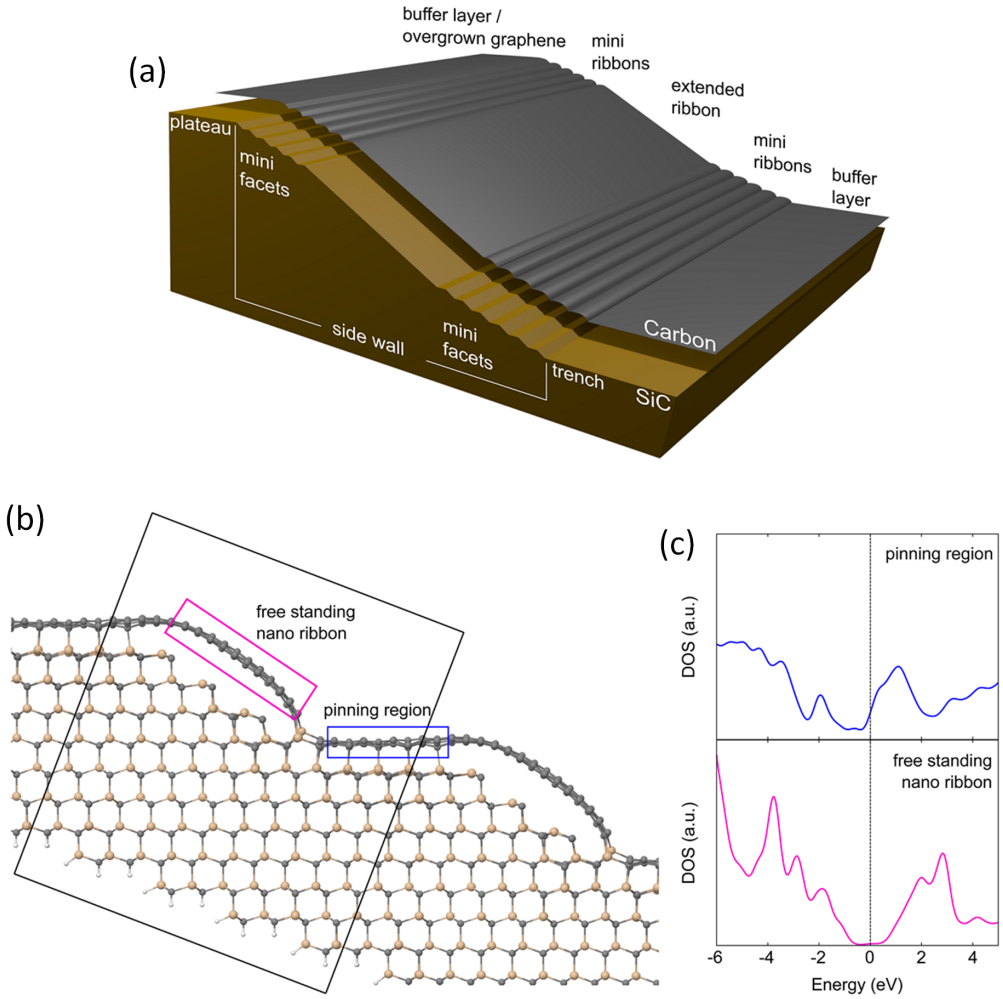

Figure 5.14: Modelization of the atomic structure and density of states. (a) Schematics of the model proposed for the general structure of armchair graphene ribbons grown on SiC(0001). The sidewall nanoribbon is found on the $(1\bar{1}07)$ extended facet at 30° off normal with respect to the SiC (0001) plane. Above and below the sidewall, a series of regions composed of minifacets and miniterraces exhibiting normals tilted $\sim 20°$ from the (0001) plane are found. In the graphene on the minifacets, graphene is bonded to the substrate, while graphene on the miniterraces is floating without any strain and exhibits a band gap. The band gap is due to the quantum confinement in the miniribbon. (b) Relaxed atomic positions of single-layer graphene miniribbons at SiC facet with [0001] and $[1\bar{1}05]$ normals. (c) Density of states at the positions indicated in (b). Top panel: gapped and doped buffer layer with some interface states in the gap. Bottom panel: floating graphene in the electronically decoupled miniribbon.

the simpler case of quantum confinement in free-standing ribbons with specific edge functionalizations. The 0.25 eV energy shift observed for the π^* carbon edge in the graphene miniribbon is almost certainly related to these quantum confinement effects. In fact, quantum confinement also induces strong width-dependent excitonic effects with respect to ground-state electronic structures, strongly decreasing the onset of optical measurements and EELS core edges [189, 190]. This explains the observed energy shift in EELS spectra, which is much smaller than the band gap opening expected for few nanometer width ribbons.

5.6 Conclusions and perspectives

Motivated by the appearance of an unknown band gap opening observed by ARPES, we performed a thorough complementary study of sidewall nanoribbon arrays to understand the link between the atomic and electronic structure. In detail, we have understood:

- Structure of the sidewall nanoribbon

We have performed the first structural studies with atomic resolution on the original sidewall nanoribbon array samples grown by our collaborators in Georgia Tech. Our STM measurements allowed to observe for the first time the high quality of the smooth edges and the ordered structure for armchair sidewall nanoribbons with respect to zigzag sidewall nanoribbons. Relying on STEM measurements, we were able to observe a cross section of the sidewall nanoribbon array. We observed the sidewall nanoribbon on the $(1\bar{1}07)$ and $(\bar{1}107)$ facets, whose distance to the substrate is 3.5 Å, suggesting a high decoupling from the substrate and agreeing with ARPES measurements showing an undoped metallic band structure.

- Sub-structure on armchair sidewall nanoribbons and origin of the band gap

By probing the last graphene layer on armchair sidewall nanoribbons we studied the origin of the band gap observed by ARPES. STM allowed to observe a ripple-like sub-structure that had not been observed before, whose width is of a few nm per ripple. Further cross section STEM measurements confirmed the presence of ripple-like structures on the transition regions below and above the sidewall nanoribbon. The ripple regions have a normal of $\sim 20°$, close to the expected one for the region where

a band gap appears. Graphene extends continuously across all the aforementioned regions. Each transition region presents a sub-faceting on the SiC substrate composed of minifacets (12°-25° normal) and miniterraces (0° normal). The subfaceting occurs at every four SiC bilayers, which corresponds to the unit cell of the 4H-SiC polytype. Graphene on top of the miniterraces is found 2.3 Å away from the substrate, typical of a semiconducting buffer layer on SiC(0001), further confirmed by EELS measurements. On the other hand, graphene on top of the minifacets (miniribbon) is found 4.0 Å away from the substrate, decoupling it from the substrate. Despite this decoupling, a gap appears. The origin of the gap observed by ARPES and locally by STEM-EELS, is due to electronic confinement on the miniribbons of 1-2 nm width. Ab-initio calculations confirm the presence of this gap.

- Adaptation of the thinning process for sidewall nanoribbon samples

To obtain information from STEM measurements, I have adapted the standard thinning process to sidewall nanoribbon samples. Although the three stages of the thinning process are time consuming and very delicate, we succeeded to obtain suitable samples.

These observations open an interesting perspective in terms of tailoring the graphene band gap. Changing the SiC polytype and therefore the c-axis periodicity could result in a different nanofaceting, leading to different miniribbon widths to control the band gap. For example, with the 3C polytype a gap of ~ 1.33 eV can be reached. Improvements are also required for zigzag sidewall nanoribbons, that have been less extensively studied due to nanofaceting of the sidewalls into more stable armchair facets. In conclusion, the sidewall ribbon geometry offers many new architectures, ensuring to stimulate new graphene device structures.

Conclusions and perspectives

The major challenge for graphene-based applications is the absence of a band gap, as it is the key factor to switch between the on and off logic states of electronic devices. Graphene nanoribbons provide a route to open a band gap, although tailoring is often challenging due to the difficulty of controlling the nanoribbon width at the atomic level and obtaining well-ordered edges. We have studied different ways to tailor band gaps on graphene by controlled growth on pre-structured substrates. We have used two different approaches: the introduction of a superperiodic potential on a continuous graphene layer to open mini-gaps in the band structure, and the electronic confinement approach in nanometric ribbons to induce large band-gap openings.

Conclusions

We induced a superperiodic potential on graphene by growing it in two different substrates, a vicinal Ir(332) surface and a multivicinal Pt(111) surface. Those two substrates are catalysts and allow to grow graphene by the decomposition of ethylene. On Ir(332) we found that graphene modifies the original steps of the Ir(332) substrate and transforms the underlying surface in an array of terraces and step bunching areas. We have used two different procedures to grow graphene. The temperature programmed growth technique produces graphene domains aligned with the underlying substrate that fully cover the step bunching areas. This is a promising route for graphene nanoribbons growth, and the method should be revisited with lower dosages, which is an interesting perspective of this research, but not accomplished due to limited time. On the other hand, chemical vapor deposition allows to obtain slightly p-doped graphene covering the whole Ir(332) surface with various coexisting rotational domains. This continuous graphene layer feels the periodic nanostructuration of the underlying substrate, as we have observed by angle-resolved photoemission spectroscopy. The graphene π band presents several minigaps due to the superperiodic potential. These

minigaps are consistent with the structural periodicity probed by LEED and STM, and can be satisfactorily explained by a Dirac-hamiltonian model. The modelization of the photoemission results has allowed us to retrieve the potential strength at the junctions between the terraces and step bunching. We have also tried to increase the surface potential by intercalating Cu, which is known to be adsorbed at the step edges. Cu preferentially intercalates on the step bunching area, producing there n-doped ribbons, while the non-intercalated areas remain p-doped. This results in an array of n- and p-doped nanoribbons on a single continuous layer, an array to be explored in the future.

We have also tailored the surface potential by changing the nanostructuration of the surface. For this, we have chosen a curved multivicinal Pt(111) substrate. The growth of graphene again modifies the substrate, with the transformation of the surface into (111) terraces and step bunching regions. With our growth conditions, the A-steps promote more homogeneous terrace arrays and step bunching areas, while B-type steps present wiggly edges and non-homogeneous step arrays. The homogeneous step arrays allowed us to tailor different minigaps as a function of the vicinality. As in the case of Ir(332), the combined study of ARPES, LEED, STM and modelization allowed us to retrieve the potential strength at the junctions between terraces and step bunching. Our study shows that it is possible to control the surface potential and therefore the induced minigaps in different ways. The potential strength increases as a function of the vicinal angle, as a function of the step type (A or B), and as a function of the substrate.

The second way to control the gap that I have studied is the electronic confinement in graphene nanoribbons grown on SiC. These ribbons are grown on an array of artificially lithographed trenches stabilized into sidewalls by further annealing on the SiC(0001) facet. Here, a band gap opening with unclear atomic origin had been observed by ARPES. We have performed the first atomically resolved study in these nanostructures, demonstrating by STM the smoothness and chirality of the edges, and precisely locating the graphene on the facets. We have also discovered some unexpected nanoribbons of 1 - 2 nm wide. To analyze the role of these structures on the band gap opening, we have studied them by cross-sectional STEM study, so we adapted a standard thinning process to sidewall nanoribbon samples. We observed that the miniribbons observed by STM border the extended $(1\bar{1}0n)$ and $(\bar{1}10n)$ facets of the sidewall ribbons, where photoemission and STS indicate the presence of metallic graphene. STEM has allowed to observe the coupling of these miniribbons to the substrate. Here, graphene extends continuously on the sub-faceted SiC substrate both on the $(1\bar{1}05)$ minifacets and (0001) miniterraces. Graphene on top of the (0001) miniterraces is cou-

pled to the substrate and is semiconducting, confirmed by local EELS measurements. On the other hand, graphene on top of the $(1\bar{1}05)$ minifacets is decoupled from the substrate. Despite this, EELS shows a gap on these decoupled miniribbons of 1 - 2 nm width that have an orientation compatible with the gap observed in photoemission. All these results together have allowed us to conclude that the band gap is due to electronic confinement.

Perspectives

This PhD work has opened many interesting perspectives. We have focused on the role of superperiodic potentials on continuous graphene layers, and the natural evolution of this work is to develop discontinuous graphene ribbons to promote total confinement, as in the case of ribbons on SiC. On the case of graphene on Ir(332), we have shown that the growth starts on the step bunching areas, so discontinuous nanoribbons can be probably obtained by performing only a partial coverage of the surface. On the case of graphene on vicinal Pt(111), an interesting perspective is to exploit the higher surface potential of B-type steps. However, these step arrays were more irregular with the explored conditions than the ones with A-type, suggesting the need of a detailed growth study. Also, discontinuous graphene nanoribbons should be achieved with lower ethylene dosages for certain vicinal surfaces with high misorientation angles, as Pt(311).

With respect to the confinement gap in the graphene miniribbons on SiC, we expect that it can be controlled by changing the SiC polytype. In this way, the c-axis periodicity should induce a different nanofaceting, leading to other miniribbon widths and new band gap values. For example, with the 3C polytype, a gap of ~ 1.33 eV could be reached. In conclusion, the different studied geometries and growth methods offer a wide playground to reach customized properties, whose detailed understanding may be useful for technological goals.

Appendix A

Supplementary material

A.1 Temperature programmed growth on Gr/Ir(332)

Table A.1: Different growth conditions of graphene by TPG explored in this thesis

Sample	Dosage (Langmuir)	T_{tpg} (°C)	t_{act} (°C)	Cooling rate (°C/min)
1	0.45	600/679	15	22.6
2	0.45	600/671	5	22.3
3	1.35	600/679	5	22.6
4	1.35	650/717	5	21.7
5	1.35	650/716	15	21.6
6	4.05	650/745	15	22.5
7	6.75	650/723	15	21.9
8	6.75	700/774	15	22.1
9	0.45	730/819	15	22.7
10	6.75	730/823	15	22.8
11	33.8	730/823	15	22.8
11B	371	730/794	15	22.0
11C	1050	730/800	15	22.2
12	1130	730/800	15	22.2
13	1080	730/788	15	23.9
14	6.75	724/820	15	22.8
14B	33.8	730/810	15	22.5
14C	338	744/790	15	23.2
14D	338	750/795	15	22.7
14E	338	750/795	15	22.7
15	338	753/759	15	19.9
15B	338	760/791	15	20.3
15C	338	753/800	15	20.2

Note: The letters indicate cumulative graphene doses on the same sample.

A.2 Chemical vapor deposition on Gr/Ir(332)

Table A.2: Different growth conditions of graphene by CVD explored in this thesis

Sample	T_{cvd} (Langmuir)	Dosage (°C)	Cooling rate (°C/min)
1	22.50	600/659	60
2	33.75	650/713	60
3	33.75	715/800	60
4	67.50	715/811	60

A.3 STM images of graphene on multivicinal curved Pt(111)

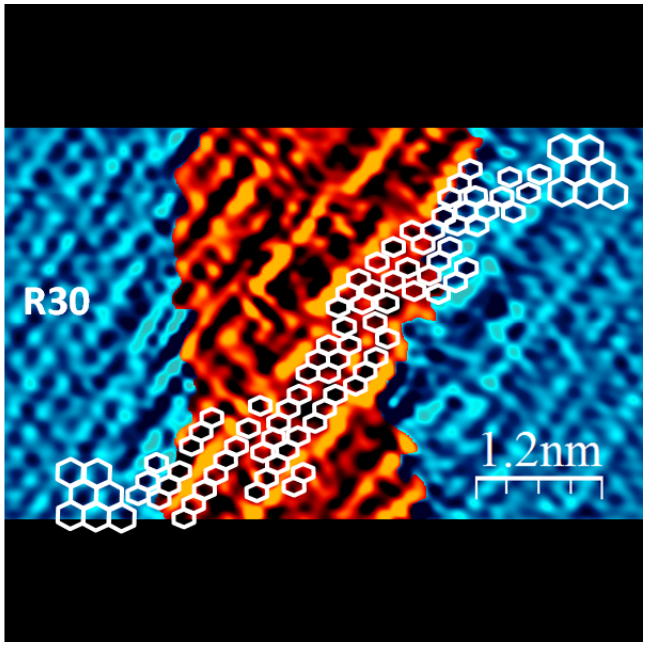

Figure A.1: STM detail for the vicinal angle −11°. The red (blue) color denotes the step bunching (terraces) [1.14 V, 0.7 nA].

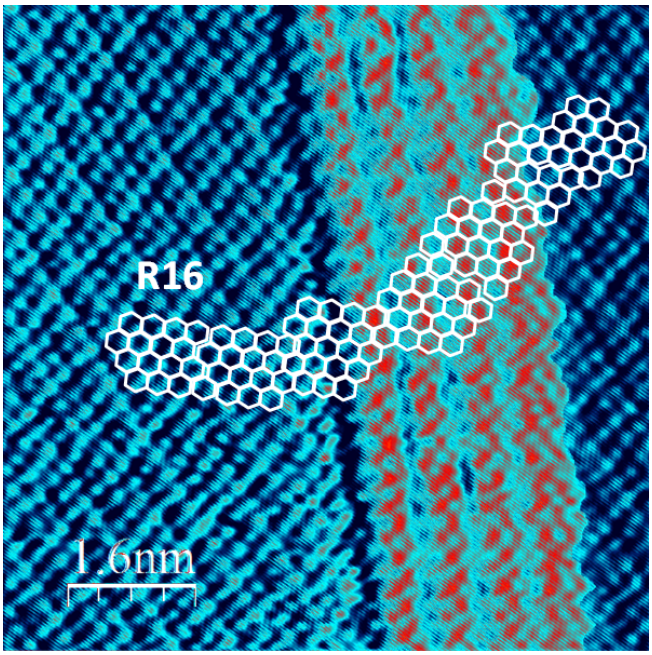

Figure A.2: STM detail for the vicinal angle $-7°$. The red (blue) color denotes the step bunching (terraces) [100 mV, 2.8 nA].

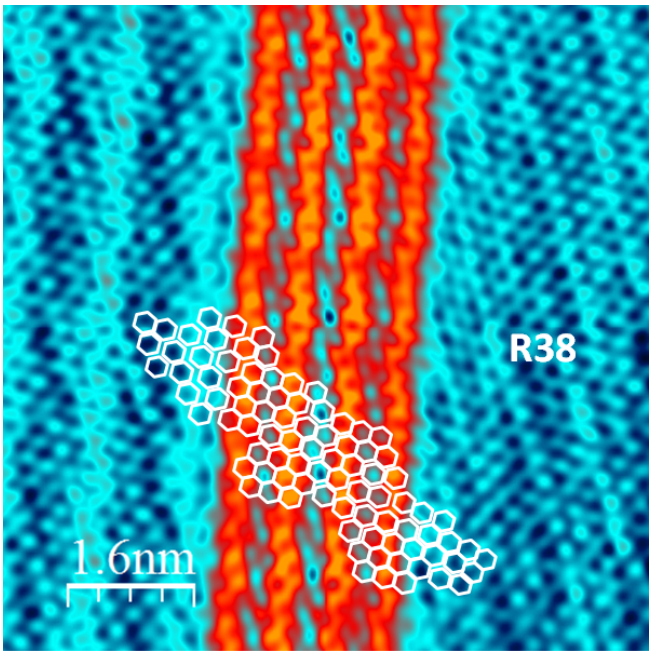

Figure A.3: STM detail for the vicinal angle $-3.5°$. The red (blue) color denotes the step bunching (terraces) [70 mV, 2.6 nA].

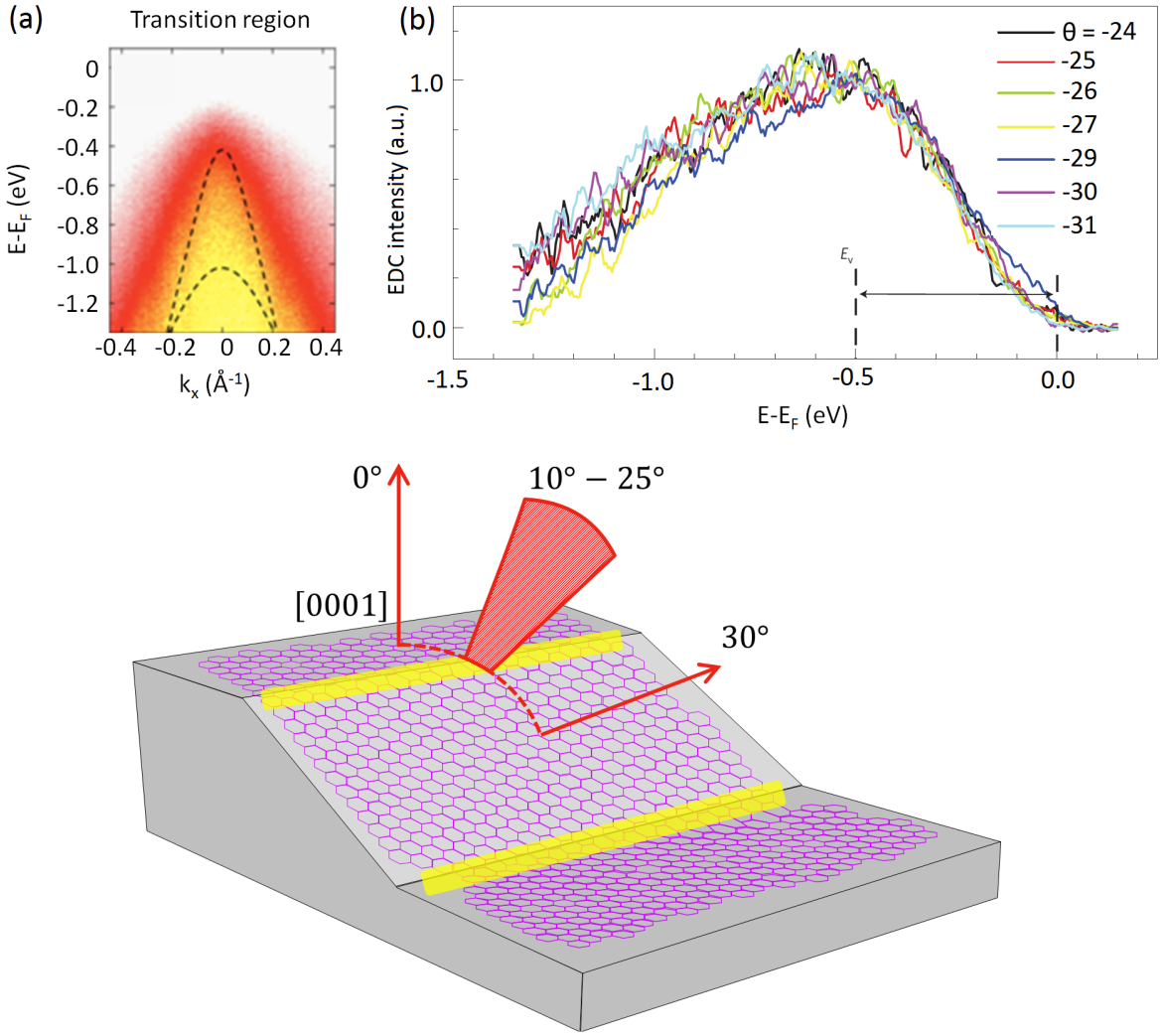

Figure A.4: Array of slightly overgrown armchair nanoribbons probed by ARPES. (a) Transition region exhibiting a band gap of at least 500 meV obtained perpendicular to the long axis of the ribbons. (b) Normalized EDCs ($k_x = 0$) of the cones in the transition region for different θ rotations. All cones in the transition region have the same profile, demonstrating the 1D nature of the region [89].

Appendix B

Résumé en français

La miniaturisation extrême des dispositifs électroniques leur a permis de devenir nos compagnons du quotidien grâce à leur portabilité. Le graphène est apparu dans ce contexte, avec d'excellentes propriétés pour encore pousser la miniaturisation, comme sa capacité de dissipation de la chaleur, sa haute capacité de transport du courant ou son transport balistique qui favorise la propagation du courant sans dissipation.

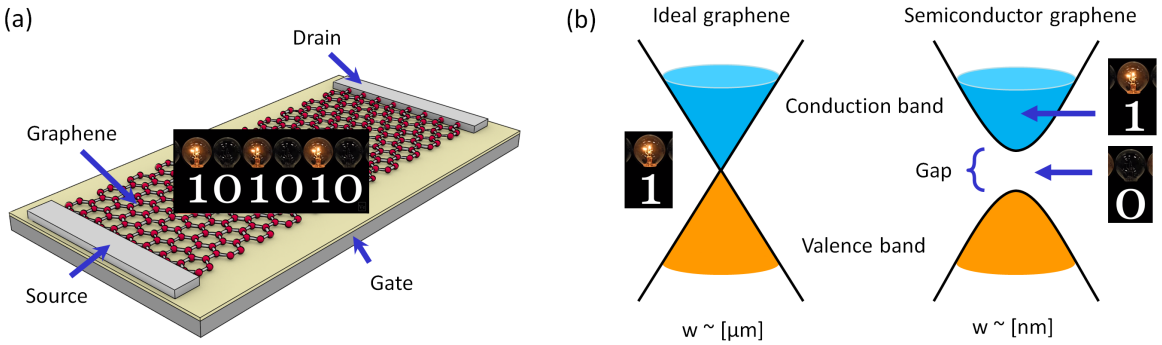

Figure B.1: (a) Schéma d'un transistor qui commute entre les états "allumé"/"éteint" représentés par 1-0, où le graphène est le canal de conduction. (b) Diagramme de la structure de bandes du graphène idéal et du graphène avec une bande interdite. Le graphène idéal ne permet pas d'accéder à l'état logique 0, puisque les électrons peuvent toujours passer de la bande de valence à la bande de conduction. En revanche, en ouvrant une bande interdite dans le graphène, il est possible de commuter entre les états logiques 0 et 1.

Toutefois, si on veut utiliser le graphène comme le canal de conduction d'un transistor, il est nécessaire de pouvoir commuter entre les états logiques 1 et 0 (fig. B.1a). Cependant le graphène idéal n'a pas de bande interdite et par conséquent ne permet pas d'obtenir un état logique 0. Pour pouvoir obtenir cet état 0 de non conduction, il faut ouvrir une bande interdite dans le graphène (fig. B.1b). Un des axes de recherche actuel

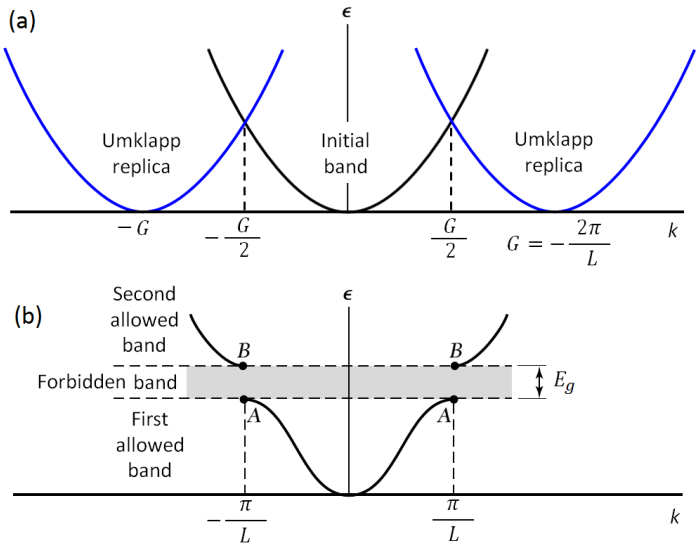

Figure B.2: (a) Schéma montrant la dispersion E(k) parabolique d'électrons libres (en noir) ainsi que des Umklapp (en bleu) dus à une superpériodicité L correspondant au vecteur de l'espace réciproque $G = (2\pi/L)$. (b) Schéma montrant la dispersion E(k) près du nouveau bord de zone à $G/2 = \pm(\pi/L)$ (au croisement entre la bande parabolique initiale et les Umklapps).

dans le graphène est précisément l'ouverture d'une bande interdite dans le graphène sans affecter la mobilité des électrons.

La nanostructuration des surfaces permet le contrôle de ses propriétés électroniques soit à cause d'un confinement total [88, 137, 149–151] soit à cause d'un confinement partiel dans des systèmes superpériodiques, où la superpériodicité L induit l'ouverture de gaps à des endroits précis de l'espace réciproque, en relation avec le vecteur de l'espace réciproque $G = 2\pi/L$. La fig. B.2 a montre un schéma de superperiodicité 1D. La bande parabolique initiale est montrée en noir, tandis que les Umklapps associées au vecteur $G = 2\pi/L$ sont montrés en bleu. La fig. B.2b montre la nouvelle périodicité qui induit une nouvelle zone de Brillouin, où des bandes interdites sont ouvertes en bord de zone à $G/2 = \pm(\pi/L)$. La largeur de la bande interdite (E_g) dépend de la force du potentiel [152] et peut modifier significativement la dispersion de bandes.

Ce travail de thèse a été dédié précisément à l'ouverture de bandes interdites dans la structure électronique du graphène par nanostructuration. Nous nous sommes focalisés sur l'obtention de nanorubans de graphène en utilisant des substrats pre-structurés et des méthodes de croissance adaptés. Nous avons suivis deux approches : l'introduction d'un potentiel superpériodique sur le graphène par des substrats vicinaux de métaux nobles et le confinement électronique dans des nanorubans sur des facettes artificielles du SiC.

Structure électronique du graphène sur Ir(332) et sur un cristal multivicinal de Pt(111)

Les substrats vicinaux de métaux nobles utilisés ont été l'Ir(332) et un cristal courbé multivicinal de Pt(111). La surface parfaite d'Ir(332) est composée de marches d'Ir(111) de 1.25 nm. Ces marches s'étendent le long de la direction $[10\bar{1}]$ et introduisent une périodicité dans la direction $[1\bar{2}1]$ (fig. B.3a). Le cristal multivicinal de Pt(111) permet d'étudier une large gamme des surfaces vicinales de Pt(111), certaines pouvant a priori produire des nanorubans de graphène discontinus. L'orientation macroscopique du cristal multivicinal va de 0° pour la normale (111) jusqu'à 16° dans les directions $[11\bar{2}]$ et $[\bar{1}\bar{1}2]$ (fig. B.3b). Les valeurs positives et négatives sont associés aux bords de marche du type A et B de chaque côté du cristal (fig. B.3c).

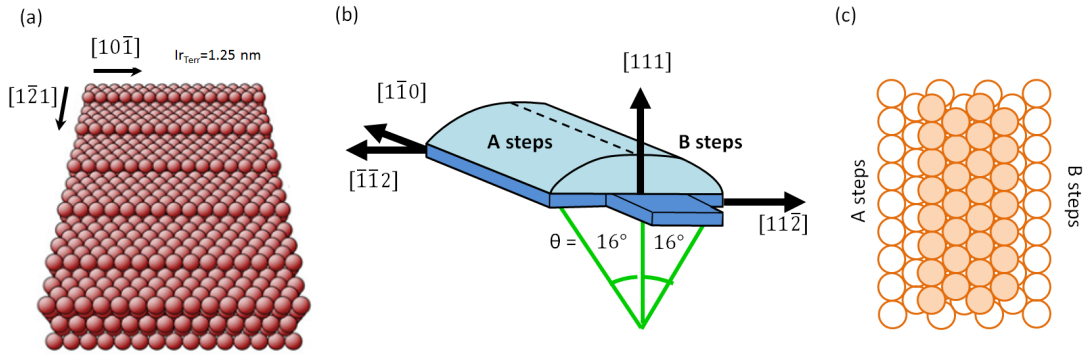

Figure B.3: : (a) Schéma de la surface idéale d'Ir(332) avec des marches de 1.25 nm qui s'étendent le long de la direction $[10\bar{1}]$ et qui introduisent une périodicité dans la direction $[1\bar{2}1]$ [114]. (b) Schéma du cristal multivicinal Pt(111). On trouve l'orientation (111) au centre du cristal (angle vicinal = 0°). Lorsqu'on s'éloigne du centre vers les directions $[11\bar{2}]$ ou $[\bar{1}\bar{1}2]$, la surface présente des bords de marche de type A ou B. Les marches s'étendent le long de la direction $[1\bar{1}0]$. (c) Schéma de la surface de Pt(111) et de la géométrie des bords de marches de type A et B.

Sur ces substrats, nous avons utilisé deux différentes méthodes de croissance du graphène, notamment la croissance programmée en température (temperature programmed growth - TPG en anglais) et le dépôt chimique en phase vapeur (chemical vapor deposition - CVD en anglais). La méthode TPG consiste à faire un dépôt d'une molécule riche en carbone (éthylène dans notre cas) sur un métal catalytique à température ambiante. Après ce dépôt, la surface est recuite au-dessus de 600°C, ce qui décompose les molécules d'éthylène et favorise la mobilité du carbone dans la surface du métal pour commencer la nucléation, croissance et/ou fusion d'îlots de

graphène. La méthode CVD consiste à exposer la molécule riche en carbone à une surface chaude. Contrairement à la méthode TPG, la dissociation des molécules d'éthylène et la formation de graphène se produisent en une seule étape. Selon la dynamique de refroidissement, le graphène résultant peut avoir un seul ou plusieurs orientations différentes [117–121, 126]. Les deux méthodes sont auto-limitantes, c'est-à-dire une fois que le graphène recouvre la surface, la croissance du graphène s'arrête car le processus catalytique de croissance ne peut plus avoir lieu [129].

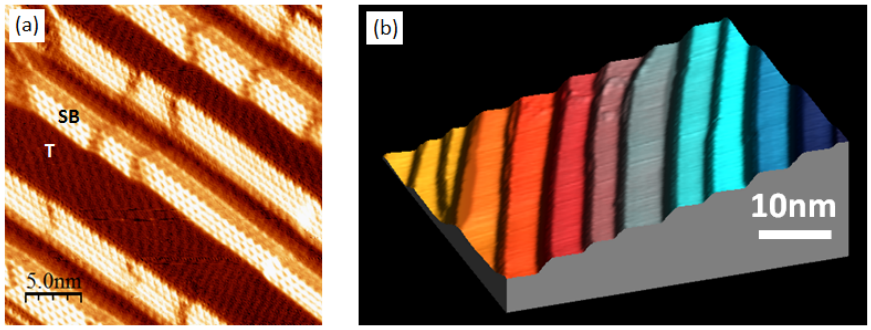

Figure B.4: (a) Image de microscopie à effet tunnel de graphène sur Ir(332) produit par CVD [0.9 V, 0.5 nA]. La surface est reconstruite avec des zones de marches (111) (T - terrasses) et des accumulations de marches (SB – Step Bunching), indiqués sur l'image. (b) Image STM 3D du cristal multivicinal de Pt(111) pour un angle vicinal $\sim -7°$. La surface présente aussi une reconstruction périodique avec des zones de terrasses (111) et des accumulations de marches.

Le résultat de la croissance de graphène sur Ir(332) par CVD est une couche continue de graphène sur des zones du substrat avec de terrasses (111) et des régions d'accumulation de marches (indiqués par T et SB sur la fig. B.4a). Sur la surface multivicinale de Pt (111), le graphène produit une structure similaire des deux côtés du cristal. La fig. B.4b montre une image STM représentative de la surface. Une fois que le graphène repose sur une surface avec une superpériodicité bien définie, la structure électronique a été étudiée par photoémission résolue en angle (ARPES). Sur les deux systèmes étudiés nous retrouvons la dispersion linéaire du graphène avec des bandes interdites aux endroits de l'espace réciproque correspondant au bord de zone de la superpériodicité, dont la période a été préalablement mesurée par STM. La fig. B.5 montre la structure de bandes et l'emplacement des bandes interdites pour le système Gr/Ir(332) (panneau a) et pour trois endroits différents pour le système Gr/multivicinal Pt(111). Pour modéliser la structure de bandes, nous avons utilisé un hamiltonien de Dirac à deux dimensions. Avec cet hamiltonien on peut décrire les dispersions et déduire le potentiel responsable de la superpériodicité à partir de la résolution numérique

des équations suivantes:

$$\cos(k_x l) = \cos(k_1 a)\cos(k_2 b) + \frac{k_y^2\hbar^2 v_f^2 + E\cdot(E-V)}{\hbar^2 v_f^2 k_1 k_2} \tag{1}$$

avec les relations:

$$k_1 = \left(\frac{[V-E]^2}{\hbar^2 v_f^2} - k_y^2\right)^{1/2} \tag{2}$$

$$k_2 = \left(\frac{E^2-\Delta^2}{\hbar^2 v_f^2} - k_y^2\right)^{1/2} \tag{3}$$

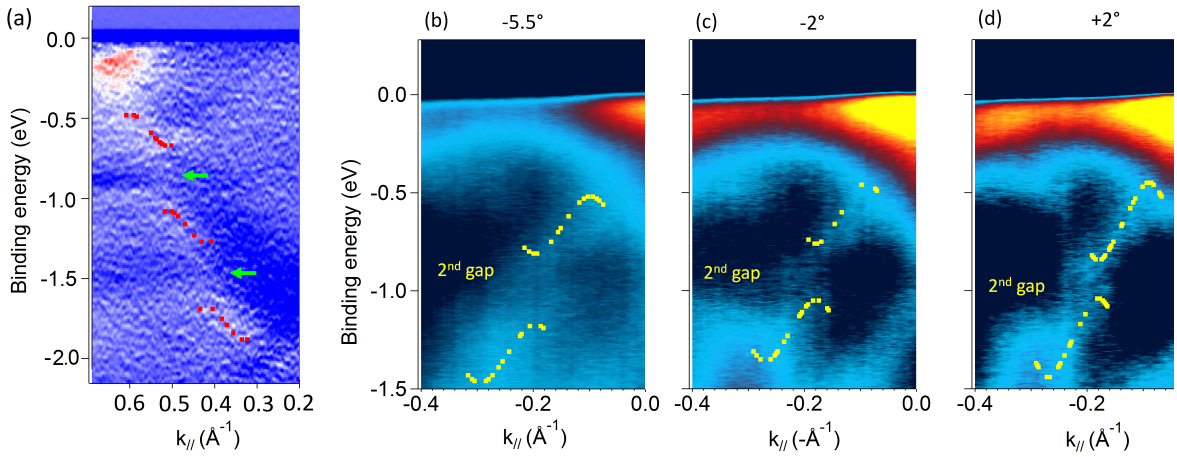

Figure B.5: (a) Structure électronique étudiée par ARPES pour le système Gr/Ir(332). La courbe obtenue par l' hamiltonien de Dirac (ligne pointillé rouge) est superposée. Le potentiel associé à la superpériodicité correspondante est 4.4 eV Å. La structure électronique étudiée par ARPES pour graphène sur Pt(111) multivicinal est montrée pour trois angles d'orientations différentes par rapport à la direction (111) : (b) -5.5°, (c) -2° et (d) +2°. Les courbes obtenues avec l'hamiltonien de Dirac sont superposées (lignes pointillées jaunes) et correspondent à des barrières de potentiel de (b) 3.35 eV Å, (c) 2.8 eV Å et (d) 1.8 eV Å.

Les dispersions de bandes calculées avec l'hamiltonien de Dirac sont superposées sur les données expérimentales, montré dans la fig. B.5 (rouge sur panneau a, et jaune sur panneaux b-d). La fig. B.6 fait le bilan des différents résultats. Nous observons que la force du potentiel augmente lorsque la périodicité diminue (ensemble bleue sur la fig. B.6), ce qui suggère que le régime de confinement total pourrait être atteint avec une taille de marches encore plus faible. Nous avons aussi étudié le potentiel induit par le bord de marche. Pour cela, nous avons comparé des périodicités identiques mais avec des bords de marche différents (ensemble rose sur la fig. B.6). Le potentiel associé au bord de marche du type A est plus grand, probablement à cause d'un couplage

plus fort entre le graphène et le substrat. Finalement nous avons aussi comparé le potentiel en fonction du substrat sur des systèmes avec la même périodicité et le même bord de marche. Nous avons ainsi observé que le potentiel est plus fort dans l'iridium, probablement à cause d'une distance graphène-substrat plus faible (ensemble verte sur la fig. B.6). L'ensemble de nos résultats montre donc différentes manières de contrôler la force du potentiel qu'induisent des minigaps dans la structure de bandes de graphène.

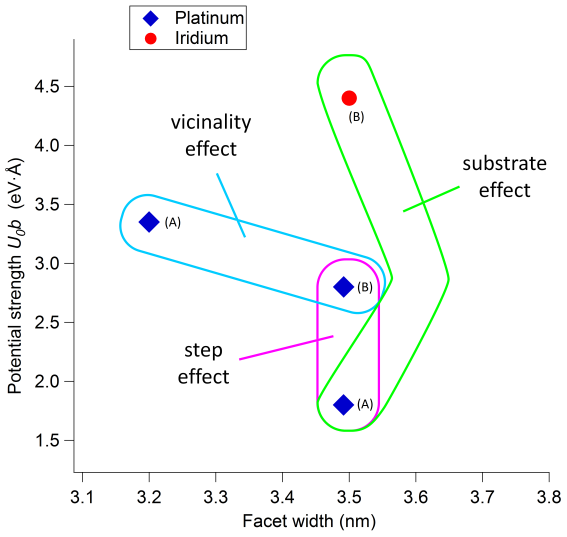

Figure B.6: Force du potentiel U_0b calculée versus l'angle vicinale pour trois vicinalités différentes du cristal multivicinal de Pt(111) et pour Ir(332). L'enceinte rose correspond aux périodicités de 3.5 nm sur des bords de marches de type A et B (angle vicinal -2° et +2°). L'enceinte verte correspond aux périodicités de 3.5 nm sur des bords de marche de type B sur le platine (+2°) et iridium (+11°). L'enceinte bleue correspond aux périodicités 3.5 nm et 3.2 nm (-5.5° et -2°) sur des bords de marche du type A.

Ouverture de bande interdite sur des nanorubans de graphène sur SiC

Il est a priori possible d'ouvrir une bande interdite dans le graphène dans des rubans nanométriques [29,31,49,61,82]. Néanmoins, l'obtention de rubans de graphène à haute mobilité et avec des bords non rugueux est difficile [72,73,171–173]. Le groupe de Walt de Heer (Georgia Tech) a développé une approche originale pour faire la croissance de nanorubans de graphène à bords lisses. Par lithographie suivi de recuits, des nanorubans de graphène sont obtenus sur des facettes "sidewalls" de SiC. L'échantillon est une

assemblée de "sidewalls", montré sur la fig. B.7. Ce type de croissance permet d'adapter la taille et les bords des rubans, permettant le control des propriétés électroniques avec une méthode qui peut être transférée à l'échelle industrielle.

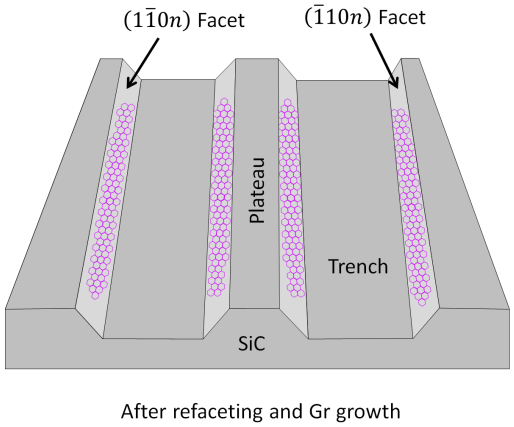

Figure B.7: 4H-SiC(0001) substrat après le processus de lithographie et recuit pour stabiliser les facettes "sidewalls" $(1\bar{1}0n)$ et $(\bar{1}10n)$ pour promouvoir la croissance de nanorubans de graphène.

Dans le cadre de notre collaboration avec Georgia Tech, l'assemblée de nanorubans de graphène a été étudiée par ARPES. La fig. B.8 montre le bilan de ces études, où trois régions électroniquement différentes sont présentes sur ces rubans [89]. Le graphène dont la normale à la surface est (0001) est métallique et dopé n, comme attendu [175]. Par contre, le graphène qui croît sur le sidewall (avec une normale de $\sim 30°$) est métallique et neutre (panneau c), ce qui indique qu'il est découplé du substrat. En revanche, le graphène qui a des normales intermédiaires a une bande interdite d'au moins 500 meV (panneau b). L'origine de ce gap a été suggérée d'être dans le graphène qui croit sur la région courbé (en jaune). Afin de comprendre l'origine structurale de cette bande interdite aussi large, nous avons contrasté des études spectroscopiques à des études structurales.

Nous avons d'abord étudié la structure du système par STM. Les images à large échelle montrent l'assemblée composée de plateaux, facettes et tranchées (fig. B.9a) ; les rubans se localisent principalement sur les facettes et ont des bords lisses et droits. Lorsqu'on fait un zoom sur la facette $(1\bar{1}0n)$, on observe la structure de nid d'abeille du graphène et des variations topographiques forts (fig. B.9b). La région (1) correspond à la partie basse de la tranchée, où on observe la présence d'un précurseur de graphène (buffer layer). La région (2) montre du graphène qui s'étend de la facette jusqu'au plateau. La région (3) montre du graphène qui s'étale sur le plateau (0001).

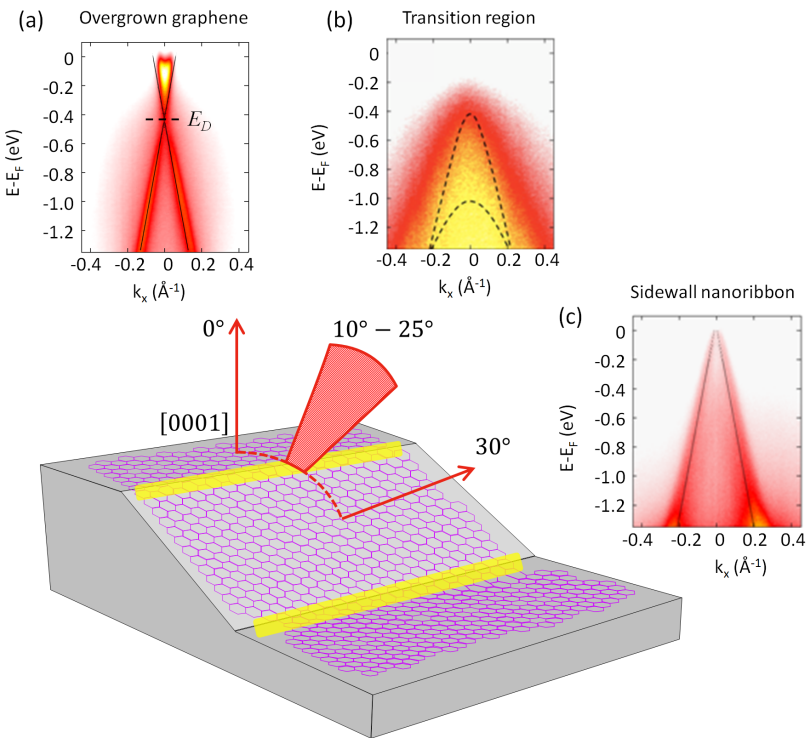

Figure B.8: Nanorubans de graphène de type armchair étudiés par ARPES. Trois régions avec des propriétés différentes du graphène sont observées : le graphène sur le SiC(0001) (normal à 0°), graphène sur les "sidewalls" (normal à $\sim 30°$) et une région de transition (avec normal entre 10°-25°). (a) Dispersion du graphène mesurée dans la région de normale 0°. Le graphène ici est métallique, dopé n. (b) Dispersion du graphène mesurée dans la région de transition. Le graphène ici a une bande interdite d'au moins 500 meV. (c) Dispersion du graphène mesurée sur les "sidewalls". Le graphène ici est métallique et neutre, ce qui indique un découplage du substrat [89].

Ce graphène va jusqu'à la frontière avec la région (4), où on trouve à nouveau un stade précurseur à la croissance du graphène. La résolution atomique dans le rectangle bleu confirme l'orientation armchair du bord (fig. B.9c). Dans la région (2) on observe des corrugations avec une taille caractéristique de $\sim$ 1 nm, qui n'étaient pas attendues et n'avait donc pas été considérées lors des études précédentes [89]. Cette observation ouvre une porte vers une meilleure compréhension de l'origine de la bande interdite observée par ARPES, car elle pourrait être due au confinement électronique dans ces nanostructures s'il s'avérait que les rubans nanométriques sont découplés du substrat.

La technique idéale pour étudier le couplage du graphène au substrat est la microscopie électronique à transmission, à condition qu'on puisse amincir l'échantillon à quelques centaines de nm, de manière à ce que le faisceau d'électrons puisse traverser l'échantillon. Pour amincir l'échantillon, nous avons utilisé trois étapes: redimension-

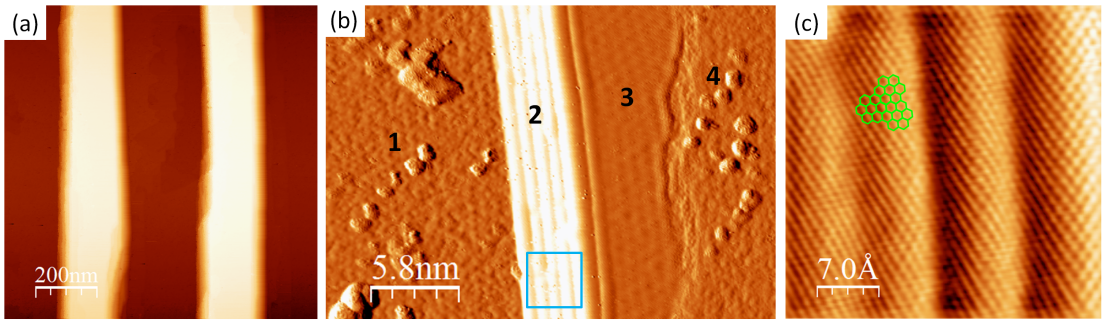

Figure B.9: (a) Image à grande échelle montrant l'assemblée de nanorubans de graphène (la couleur la plus intense correspond aux plateaux, alors que la couleur plus foncée correspond aux tranchées) [1 V, 0.5 nA]. (b) Zoom sur une facette $(1\bar{1}0n)$ [1.1 V, 0.7 nA]. Quatre régions sont montrées: La région (1) correspond à la partie basse de la tranchée, où on trouve un stade précurseur de la croissance du graphène. La région (2) montre le graphène sur la facette $(1\bar{1}0n)$, avec des corrugations d'une taille nanométrique. La région (3) montre le graphène qui s'étend sur le plateau (0001). Ce graphène s'arrête à la frontière avec la région (4), où on trouve à nouveau un précurseur de graphène. (c) Zoom du rectangle bleu sur (b), où on observe la corrugation avec une largeur de $\sim$ 1 nm.

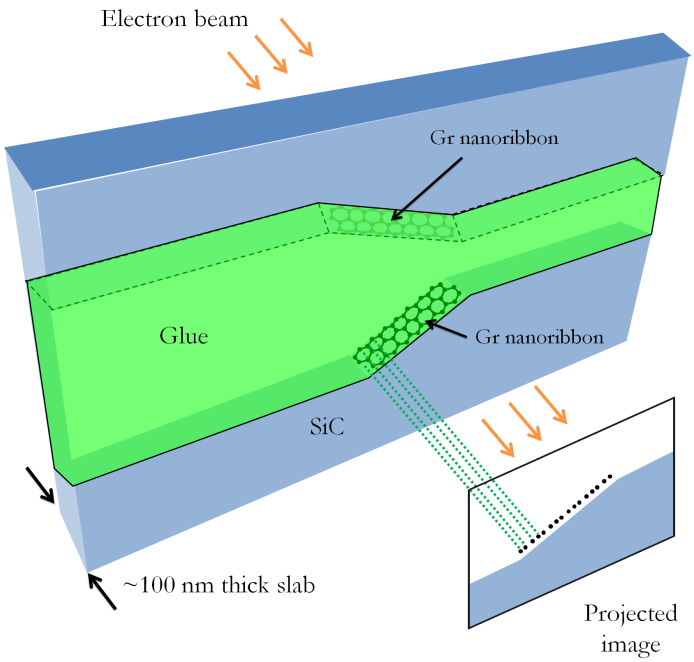

Figure B.10: Schéma de la mesure par microscopie électronique à transmission. Un faisceau d'électrons (flèches oranges) traverse les nanorubans de graphène sur SiC après avoir été amincis et collés en sandwich. Finalement la projection latérale des atomes est récupérée sur une camera CCD.

nement, polissage mécanique et bombardement ionique. L'étape de redimensionnement consiste à couper l'échantillon en deux et coller les deux parties en sandwich pour protéger les rubans de graphène à l'intérieur. Le sandwich est ensuite adapté à la taille des porte-échantillons du STEM. Plusieurs étapes de polissage mécanique avec des papiers diamantés sont faites jusqu'à obtenir un échantillon de quelques centaines de nm d'épaisseur. Finalement, l'échantillon est bombardé avec des ions d'argon pour éroder doucement la surface et atteindre l'épaisseur final souhaitée de $\sim$ 100 nm. Un schéma de l'échantillon après ces trois étapes est montré sur la fig. B.10. Le faisceau d'électrons du STEM (flèches oranges) traverse l'échantillon et une projection de l'arrangement des atomes est récupérée sur une camera CCD.

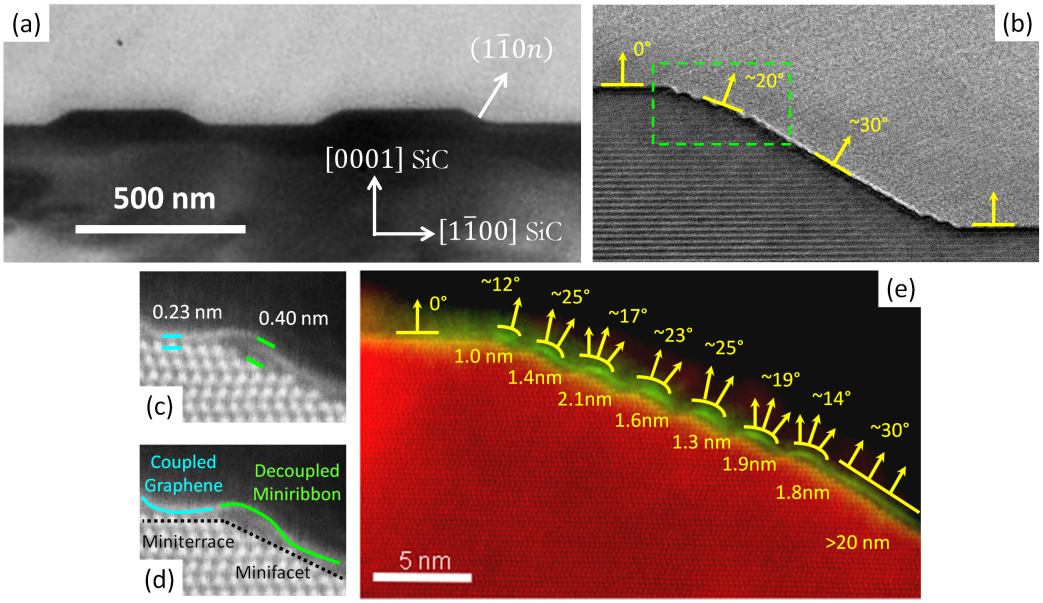

Figure B.11: (a) Image de STEM en coupe transversale de la structure globale où se trouvent les rubans de graphène. (b) Zoom sur la facette $(1\bar{1}0n)$ montrant une ondulation des parties haute et basse de la facette dite "sidewall". Cette région ondulée a des normales à $\sim$ 20° par rapport à la normale du SiC(0001). (c)(d) Zoom sur une ondulation où l'on voit le détail des régions ondulées. Il y a des mini-terrasses et des mini-facettes. La distance entre le graphène et le substrat dans la mini-terrasse est de 0.23 nm, ce qui indique que le graphène ici est couplé au substrat. La distance entre le graphène et le substrat dans la mini-facette est de 0.40 nm, ce qui indique que le graphène ici est découplé du substrat. (e) Zoom sur le rectangle vert dans le panneau (b) qui montre le graphène en vert et le SiC en rouge. Les nanorubans ont des normales entre $\sim$ 12° et 25° et une largeur de 1-2 nm.

La coupe transversale par STEM d'un ensemble de nanorubans de graphène est montrée à la fig. B.11a. L'agrandissement sur la facette $(1\bar{1}0n)$ (panneau b) permet

d'identifier une corrugation similaire à celle observée précédemment en STM dans les parties haute et basse de la facette dite "sidewall". Le détail de cette zone ondulée se montre dans les panneaux c-d: il y a des mini-terrasses d'orientation (0001) et des mini-facettes. Le graphène s'étend de manière continue entre ces deux régions mais la distance entre le graphène et le substrat change. La distance entre le graphène et le substrat dans les mini-terrasses est de 2.3 Å, ce qui suggère un fort couplage avec le substrat. En revanche, la distance entre le graphène et le substrat dans les mini-facettes est de 4.0 Å, ce qui résulte en un découplage du graphène ici et devrait donc être métallique. Cependant la normale de ces régions varie entre $\sim 12°$ et $25°$, ce qui correspond aux normales ou la bande interdite est observée par ARPES. Comme ces mini-rubans ont une largeur de 1-2 nm permettant d'ouvrir une bande interdite dans le graphène et qu'une bande interdite a été observée malgré le découplage du substrat, nous concluons que la raison de l'ouverture de la bande interdite est le confinement électronique dans ces nanorubans. Des mesures d'EELS avec résolution atomique et de calculs ab-initio soutiennent aussi cette interprétation.

Conclusions

Ce travail a été dédié à l'étude de bandes interdites dans la structure électronique du graphène par nanostructuration. Nous avons suivis deux approches : l'introduction d'un potentiel superpériodique sur le graphène par des substrats vicinaux de métaux nobles et le confinement électronique dans des nanorubans sur des facettes artificielles du SiC.

Dans les substrats vicinaux, nous avons induit un potentiel périodique dans le graphène sur deux substrats différents, sur Ir(332) et sur une surface multivicinal de Pt(111). Avec une croissance de type CVD nous avons produit du graphène continu sur la surface nanostructurée, ce qui a induit une modification de la structure de bandes du graphène que nous avons observé par ARPES. La bande π du graphène présente plusieurs minigaps associés au potentiel périodique dû à la nanostructuration. Ces minigaps peuvent être expliqués avec un hamiltonien de Dirac, ce qui nous a permis de déterminer la barrière de potentiel induite par la superpériodicité, qui dépend de la périodicité, du type de bord de marche et du type de substrat.

Dans les nanorubans de graphène "sidewall" nous avons réalisé la première étude de STM avec résolution atomique. Nous avons identifié des corrugations nanométriques que nous avons retrouvés aussi dans les études par STEM. Ces corrugations atomiques sont à l'origine de rubans de graphène d'une taille nanométrique découplés du substrat

et qui présentent une bande interdite, à cause du confinement électronique.

Bibliography

[1] J.-H. Wong, B.-R. Wu, and M.-F. Lin. Strain effect on the electronic properties of single layer and bilayer graphene. *The Journal of Physical Chemistry C*, 116:8271, 2012.

[2] V. Pereira, A. Castro Neto, and N. Peres. A tight-binding approach to uniaxial strain in graphene. *Physical Review B*, 80:045401, 2009.

[3] N. Levy, S. A. Burke, K. L. Meaker, M. Panlasigui, A. Zettl, F. Guinea, A. H. C. Neto, and M. F. Crommie. Strain-induced pseudo-magnetic fields greater than 300 Tesla in graphene nanobubbles. *Science*, 329:544, 2010.

[4] R. Balog, B. Jorgensen, L. Nilsson, M. Andersen, E. Rienks, M. Bianchi, M. Fanetti, R. Laegsgaard, A. Baraldi, S. Lizzit, Z. Sljivancanin, F. Besenbacher, B. Hammer, T.G. Pedersen, P. Hofmann, and L. Hornekaer. Bandgap opening in graphene induced by patterned hydrogen adsorption. *Nature Materials*, 9:315, 2010.

[5] B. R. Matis, J. S. Burgess, F. A. Bulat, A. L. Friedman, B. H. Houston, and J. W. Baldwin. Surface doping and band gap tunability in hydrogenated graphene. *ACS Nano*, 6:17, 2012.

[6] P. A. Denis. Band gap opening of monolayer and bilayer graphene doped with aluminium, silicon, phosphorus, and sulfur. *Chemical Physics Letters*, 492:251, 2010.

[7] P. A. Denis. Chemical reactivity of band-gap opening of graphene doped with gallium, germanium, arsenic, and selenium atoms. *ChemPhysChem*, 15:3994, 2014.

[8] R. Lv and M. Terrones. Towards new graphene materials: Doped graphene sheets and nanoribbons. *Materials Letters*, 78:209, 2012.

[9] A. Castellanos-Gomez, M. Wojtaszek, Arramel, N. Tombros, and B.J. van Wees. Reversible hydrogenation and bandgap opening of graphene and graphite surfaces probed by scanning tunneling spectroscopy. *Small*, 8:1607, 2012.

[10] Z. Luo, J. Shang, S. Lim, D. Li, Q. Xiong, Z. Shen, J. Lin, and T. Yu. Modulating the electronic structures of graphene by controllable hydrogenation. *Applied Physics Letters*, 97:233111, 2010.

[11] A. L. Elías, R. R. Nair, T. M. G. Mohiuddin, S. V. Morozov, P. Blake, M. P. Halsall, A. C. Ferrari, D. W. Boukhvalov, M. I. Katsnelson, A. K. Geim, and K. S. Novoselov. Control of graphene's properties by reversible hydrogenation: Evidence for graphene. *Science*, 323:610, 2009.

[12] K. Nakada, M. Fujita, G. Dresselhaus, and M. S. Dresselhaus. Edge state in graphene ribbons: Nanometer size effect and edge shape dependence. *Physical Review B*, 54:1, 1996.

[13] K. Wakabayashi, M. Fujita, H. Ajiki, and M. Sigrit. Electronic and magnetic properties of nanographite ribbons. *Physical Review B*, 59:8271, 1999.

[14] A. H. Castro Neto, N. M. R. Peres, K. S. Novoselov, and A. K. Geim. The electronic properties of graphene. *Reviews of Modern Physics*, 81:109, 2009.

[15] P. Wagner, C. P. Ewels, J.-J. Adjizian andL. Magaud, P. Pochet, S. Roche, A. Lopez-Bezanilla, V. V. Ivanovskaya, A. Yaya, M. Rayson, P. Briddon, and B. Humbert. Band gap engineering via edge-functionalization of graphene nanoribbons. *The Journal of Physucal Chemistry C*, 117:26790, 2013.

[16] Y. W. Son, M. L. Cohen, and S. G. Louie. Half-metallic graphene nanoribbons. *Nature*, 444:347, 2006.

[17] F. Ma, Z. Guo, K. Xu, and P. K. Chu. First-principle study of energy band structure of armchair graphene nanoribbons. *Solid State Communications*, 152:1089, 2012.

[18] F. J. Martín-Martínez, S. Fias, G. Van Lier, F. De Proft, and P. Geerlings. Electronic structure and aromaticity of graphene nanoribbons. *Chemistry - A European Journal*, 18:6183, 2012.

[19] V. Barone, O. Hod, and G.E. Scuseria. Electronic structure and stability of semiconducting graphene nanoribbons. *Nano Letters*, 6:2748, 2006.

[20] Y.-W. Son, M.L. Cohen, and S.G. Louie. Energy gaps in graphene nanoribbons. *Physical Review Letters*, 97:216803, 2006.

[21] L. Yang, C.-H. Park, Y.-W. Son, M. Cohen, and S. Louie. Quasiparticle energies and band gaps in graphene nanoribbons. *Physical Review Letters*, 99:186801, 2007.

[22] L. Pisani, J. Chan, B. Montanari, and N. Harrison. Electronic structure and magnetic properties of graphitic ribbons. *Physical Review B*, 75:064418, 2007.

[23] O.V. Yazyev. Emergence of magnetism in graphene materials and nanostructures. *Reports on Progress in Physics*, 73:056501, 2010.

[24] K. Wakabayashi and M. Sigrist Y. Takane. Perfectly conducting channel and universality crossover in disordered graphene nanoribbons. *Physical Review Letters*, 99:036601, 2007.

[25] C. Berger, Z. Song, T. Li, X. Li, A. Y. Ogbazghi, R. Feng, Z. Dai, T. Grenet, A. N. Marchenkov, E.H. Conrad, P.N. First, and W. A. de Heer. Ultrathin epitaxial graphite: 2D electron gas properties and a route towards graphene-based nanoelectronics. *The Journal of Physical Chemistry B*, 108:19912, 2004.

[26] J. Bai, X. Duan, and Y. Huang. Rational fabrication of graphene nanoribbons using a nanowire etch mask. *Nano Letters*, 9:2083, 2009.

[27] G. Liu, Y. Wu, Y.-M. Lin, D. B. Farmer, J. A. Ott, J. Bruley, A. Grill, P. Avouris, D. Pfeiffer, A. A. Balandin, and C. Dimitrakopoulos. Epitaxial graphene nanoribbon array fabrication using BCP-assisted nanolithography. *ACS Nano*, 6:6786, 2012.

[28] W. A. de Heer, C. Berger, X. Wu, P. N. First, E. H. Conrad, X. Li, T. Li, M. Sprinkle, J. Hass, M. L. Sadowski, M. Potemski, and G. Martinez. Epitaxial graphene. *Solid State Communications*, 143:92, 2007.

[29] Z. Chen, Y.-M. Lin, M. J. Rooks, and P. Avouris. Graphene nano-ribbon electronics. *Physica E: Low-dimensional Systems and Nanostructures*, 40:228, 2007.

[30] J. Sang-Chul. Fabrication of a graphene nanoribbon with electron beam lithography using a XR-1541/PMMA lift-off process. *Transactions on Electrical and Electronic Materials*, 11:190–193, 2010.

[31] M. Y. Han, B. Ozylmaz, Y. Zhang, and P. Kim. Energy band-gap engineering of graphene nanoribbons. *Physical Review Letters*, 98:206805, 2007.

[32] X.-D. Chen, Z.-B. Liu, Z.-S. Jiang, X.-Q. Yan, F. Xing, P. Wang, Y. Chen, and J.-G. Tian. The selective transfer of patterned graphene. *Scientific Reports*, 3:3216, 2013.

[33] J. A. Gardener and J. A. Golovchenko. Ice-assisted electron beam lithography of graphene. *Nanotechnology*, 23:185302, 2012.

[34] X. Wang and H. Dai. Etching and narrowing of graphene from the edges. *Nature Chemistry*, 2:661, 2010.

[35] A. Sinitskii and J. M. Tour. Patterning graphene nanoribbons using copper oxide nanowires. *Applied Physics Letters*, 100:103106, 2012.

[36] G. Xu, J. Bai, C. M. Torres, E. B. Song, J. Tang, Y. Zhou, X. Duan, Y. Zhang, and K. L. Wang. Low-noise submicron channel graphene nanoribbons. *Applied Physics Letters*, 97:073107, 2010.

[37] S. E. Bryan and R. Murali Y. Yang. Conductance of epitaxial graphene nanoribbons: Influence of size effects and substrate morphology. *The Journal of Physical Chemistry C*, 115:10230, 2011.

[38] W. S. Hwang, P. Zhao, K. Tahy, L. O. Nyakiti, V. D. Wheeler, R. L. Myers-Ward, C. R. Eddy Jr., D. K. Gaskill, J. A. Robinson, W. Haensch, H. (Grace) Xing, A. Seabaugh, and D. Jena. Graphene nanoribbon field-effect transistors on wafer-scale epitaxial graphene on SiC substrates. *APL Materials*, 3:011101, 2015.

[39] R. Ribeiro, J.-M. Poumirol, A. Cresti, W. Escoffier, M. Goiran, J.-M. Broto, S. Roche, and B. Raquet. Unveiling the magnetic structure of graphene nanoribbons. *Physical Review Letters*, 107:086601, 2011.

[40] L. Tapasztó, G. Dobrik, P. Lambin, and L. P. Biró. Tailoring the atomic structure of graphene nanoribbons by scanning tunnelling microscope lithography. *Nature Nanotechnology*, 3:397, 2008.

[41] Z. J. Qi, J. A. Rodríguez-Manzo, A. R. Botello-Méndez, S. J. Hong, E. A. Stach, Y. W. Park, J.-C. Charlier, M. Drndić, and A. T. C. Johnson. Correlating atomic structure and transport in suspended graphene nanoribbons. *Nano Letters*, 14:4238, 2014.

[42] G. Z. Magda, X. Jin, I. Hagymási, P. Vancsó, Z. Osváth, P. Nemes-Incze, C. Hwang, L. P. Biró, and L. Tapasztó. Room-temperature magnetic order on zigzag edges of narrow graphene nanoribbons. *Nature*, 514:608, 2015.

[43] Z. Q. Wei, D. B. Wang, S. Kim, S. Y. Kim, Y. K. Hu, M. K. Yakes, A. R. Laracuente, Z. T. Dai, S. R. Marder, C. Berger, W. P. King, W. A. de Heer, P. E. Sheehan, and E. Riedo. Nanoscale tunable reduction of graphene oxide for graphene electronics. *Science*, 328:1373, 2010.

[44] T. H. Vo, M. Shekhirev, D. A. Kunkel, M. D. Morton, E. Berglund, K. Kong, P. M. Wilson, P. A. Dowben, A. Enders, and A. Sinitskii. Large-scale solution synthesis of narrow graphene nanoribbons. *Nature Communications*, 5:3189, 2014.

[45] X. Jia, M. Hofmann, V. Meunier, B. G. Sumpter, J. Campos-Delgado, J. M. Romo-Herrera, H. Son, Y. P. Hsieh, A. Reina, J. Kong, M. Terrones, and M. S. Dresselhaus. Controlled formation of sharp zigzag and armchair edges in graphitic nanoribbons. *Science*, 323:1701, 2009.

[46] X. Li, X. Wang, L. Zhang, S. Lee, and H. Dai. Chemically derived, ultrasmooth graphene nanoribbon semiconductors. *Science*, 319:1229, 2008.

[47] C. Vallés, C. Drummond, H. Saadaoui, C. A. Furtado, M. He, O. Roubeau, L. Ortolani, M. Monthioux, and A. Pénicaud. Solutions of negatively charged graphene sheets and ribbons. *Journal of the American Chemical Society*, 130:15802, 2008.

[48] Z. S. Wu, W. Reb, L. Gao, B. Liu, J. Zhao, and H. M. Cheng. Efficient synthesis of graphene nanoribbons sonochemically cut from graphene sheets. *Nano Research*, 3:16, 2010.

[49] C. Tao, L. Jiao, O. V. Yazyev, Y.-C. Chen, J. Feng, X. Zhang, R. B. Capaz, J. M. Tour, A. Zettl, and S. G. Louie. Spatially resolving edge states of chiral graphene nanoribbons. *Nature Physics*, 7:616, 2011.

[50] A. Narita, X. Feng, Y. Hernandez, S. A. Jense, M. Bonn, H. Yang, I. A. Verzhbitskiy, C. Casiraghi, M. Ryan Hansen, A. H. R. Koch, G. Fytas, O. Ivasenko, B. Li, K. S. Mali, T. Balandina, S. Mahesh, S. De Feyter, and K. Müllen. Synthesis of structural well-defined and liquid-phase-processable graphene nanoribbons. *Nature Chemistry*, 6:126, 2013.

[51] J. Jiao, X. Wang, G. Diankov, H. Wang, and H. Dai. Facile synthesis of high-quality graphene nanoribbons. *Nature Nanotechnology*, 5:321, 2010.

[52] D. V. Kosynkin, A. L. Higginbotham, A. Sinitskii, J. R. Lomeda, A. Dimiev, B. K. Price, and J. M. Tour. Longitudinal unzipping of carbon nanotubes to form graphene nanoribbons. *Nature*, 458:872, 2009.

[53] D. B. Shinde, M. Majumder, and V. K. Pillai. Counter-ion dependent, longitudinal unzipping of multi-walled carbon nanotubes to highly conductive and transparent graphene nanoribbons. *Scientific Reports*, 4:4363, 2014.

[54] L. Jiao, L. Zhang, X. Wang, G. Diankov, and H. Dai. Narrow graphene nanoribbons from carbon nanotubes. *Nature*, 458:877, 2009.

[55] A. L. Elías, A. R. Botello-Méndez, D. Meneses-Rodríguez, V. Jehová González, D. Ramírez-González, L. Ci, E. Muñoz-Sandoval, P. M. Ajayan, H. Terrones, and M. Terrones. Longitudinal cutting of pure and doped carbon nanotubes to form graphitic nanoribbons using metal clusters as nanoscalpels. *Nano Letters*, 10:366, 2010.

[56] D. Wei, L. Xie, K. K. Lee, Z. Hu, S. Tan, W. Chen, H. Sow, K. Chen, Y. Liu, and A. T. S. Wee. Controllable unzipping for intramolecular junctions of grpahene nanoribbons and single-walled carbon nanotubes. *Nature Communications*, 4:1374, 2013.

[57] Y. Gong, M. Long, G. Liu, S. Gao, C. Zhu, X. Wei, W. Geng, M. Sun, C. Yang, L. Lu, and L. Liu. Electronic transport properties of graphene nanoribbon arrays fabricated by unzipping aligned nanotubes. *Physical Review B*, 87:165404, 2013.

[58] L. C. Campos, V. R. Manfrinato, J. D. Sanchez-Yamagishi, J. Kong, and P. Jarillo-Herrero. Anisotropic etching and nanoribbon formation in single-layer graphene. *Nano Letters*, 9:2600, 2009.

[59] L. Ci, Z. Xu, L. Wang, W. Gao, F. Ding, K. F. Kelly, B. I. Yakobson, and P. M. Ajayan. Controlled nanocutting of graphene. *Nano Research*, 1:116, 2008.

[60] S. S. Datta, D. R. Strachan, S. M. Khamis, and A. T. C. Johnson. Crystallographic etching of few-layer graphene. *Nano Letters*, 8:1912, 2008.

[61] J. Cai, P. Ruffieux, R. Jaafar, M. Bieri, T. Braun, S. Blankenburg, M. Muoth, A. P. Seitsonen, M .Saleh, X. Feng, K. Müllen, and R. Fasel. Atomically precise bottom-up fabrication of graphene nanoribbons. *Nature*, 466:470, 2010.

[62] S. Linden, D. Zhong, A. Timmer, N. Aghdassi, J. H. Franke, H. Zhang, X. Feng, K. Müllen, H. Fuchs, L. Chi, and H. Zacharias. Electronic structure of spatially aligned graphene nanoribbons on Au(788). *Physical Review Letters*, 108:216801, 2012.

[63] Y.-C. Chen, D. G. de Oteyza, Z. Pedramrazi, C. Chen, F. R. Fischer, and M. F. Crommie. Tuning the band gap of graphene nanoribbons synthesized from molecular precursors. *ACS Nano*, 7:6123, 2013.

[64] T. Kato and R. Hatakeyama. Site-and alignment-controlled growth of graphene-nanoribbons from nickel nanobars. *Nature Nanotechnology*, 7:651, 2012.

[65] A. N. Sokolov, F. L. Yap, N. Liu, K. Kim, K. Ci, O. B. Johnson, H. Wang, M. Vosgueritchian, A. L. Koh, J. Chen, J. Park, and Z. Bao. Direct growth of aligned graphitic nanoribbonsfrom a DNA template by chemical vapour deposition. *Nature Communications*, 4:2402, 2013.

[66] I. Martin-Fernandez, D. Wang, and Y. Zhang. Direct growth of graphene nanoribbons for large-scale device fabrication. *Nano Letters*, 12:6175, 2012.

[67] D. Wang, H. Tian, Y. Yang, D. Xie, T.-L. Ren, and Y. Zhang. Scalable and direct growth of graphene micro ribbons on dielectric substrates. *Scientific Reports*, 3:1348, 2013.

[68] Y. Kobayashi, K. Kusakabe, K. Fukui, and T. Enoki. STM/STS observation of peculiar electronic states at graphite edges. *Physica E: Low-dimensional Systems and Nanostructures*, 34:678, 2006.

[69] M. Ijäs, M. Ervasti, A. Uppstu, P. Liljeroth, J. van der Lit, I. Swart, and A. Harju. Electronic states in finite graphene nanoribbons: Effect of charging and defects. *Physical Review B*, 88:075429, 2013.

[70] Y. Liu, A. Dobrinsky, and B. Yakobson. Graphene edge from armchair to zigzag: The origins of nanotube chirality? *Physical Review Letters*, 105:235502, 2010.

[71] P. Gallagher, K. Todd, and D. Goldhaber-Gordon. Disorder-induced gap behavior in graphene nanoribbons. *Physical Review B*, 81:115409, 2010.

[72] M. Y. Han, J. C. Brant, and P. Kim. Electron transport in disordered graphene nanoribbons. *Physical Review Letters*, 104:056801, 2010.

[73] F. Sols, F. Guinea, and A. H. Castro Neto. Coulomb blockade in graphene nanoribbons. *Physical Review Letters*, 99:166803, 2007.

[74] C. Stampfef, J. Güttinger, S. Hellmüller, F. Molitor, K. Ensslin, and T. Ihn. Energy gaps in etched graphene nanoribbons. *Physical Review Letters*, 102:056403, 2009.

[75] J. B. Oostinga, B. Sacépé, M. F. Craciun, and A. F. Morpurgo. Magnetotransport through graphene nanoribbons. *Physical Review B*, 81:193408, 2010.

[76] D. Gunlycke and C. T. White. Scaling of the localization length in armchair-edge graphene nanoribbons. *Physical Review B*, 81:075434, 2010.

[77] C. Berger, Z. Song, X. Li, X. Wu, N. Brown, C. Naud, D. Mayou, T. Li, J. Hass, A. N. Marchenkov, E. H. Conrad, and P. N. First. Electronic confinement and coherence in patterned epitaxial graphene. *Science*, 312:1191, 2006.

[78] G. Xu, C. M. Torres, J. Bai, J. Tang, and T. Yu. Linewidth roughness in nanowire-mask-based graphene nanoribbons. *Applied Physics Letters*, 98:243118, 2011.

[79] J. Campos-Delgado, J. M. Romo-Herrera, X. Jia, D. A. Cullen, H. Muramatsu, Y. A. Kim, T. Hayashi, Z. Ren, D. J. Smith, Y. Okuno, T. Ohba, H. Kanoh, M. S. Dresselhaus, and M. Terrones. Bulk production of a new form of sp^2 carbon: Crystalline graphene nanoribbons. *Nano Letters*, 8:2773, 2008.

[80] D. V. Kosynkin, W. Lu, A. Sinitskii, G. Pera, Z. Sun, and J. M. Tour. Highly conductive graphene nanoribbons by londigutinal splitting of carbon nanotubes using potassium vapor. *ACS Nano*, 5:968, 2011.

[81] Y. Zhu and J. M. Tour. Graphene nanoribbon thin films using layer-by-layer assembly. *Nano Letters*, 10:4356, 2010.

[82] Y. Y. Li, M. X. Chen, M. Weinert, and L. Li. Direct experimental determination of onset of electron-electron interactions in gap opening of zigzag graphene nanoribbons. *Nature Communications*, 5:4311, 2014.

[83] S. Blackenburg, J. Cai, P. Ruffieux, R. Jaafar, D. Passerone, X. Feng, K. Müllen, R. Fasel, and C. A. Pignedoli. Intraribbon heterojunction formation of ultranarrow graphene nanoribbons. *ACS Nano*, 6:2020, 2012.

[84] J. Cai, C. A. Pignedoli, L. Talirz, P. Ruffieux, H. Söde, L. Liang, V. Meunier, R. Berger, R. Li, and X. Feng. Graphene nanoribbon heterojunctions. *Nature Nanotechnology*, 9:896, 2014.

[85] J. Kunc, Y. Hu, J. Palmer, Z. Guo, J. Hankinson, S. H/ Gamal, C. Berger, and W. A. de Heer. Planar edge Schottky barrier-tunneling transistors using epitaxial graphene/SiC junctions. *Nano Letters*, 14:5170, 2014.

[86] J. Baringhaus, M. Ruan, F. Edler, A. Tejeda, M. Sicot, A. Taleb-Ibrahimi, A.P. Li, Z. Jiang, E.H. Conrad, C. Berger, C. Tegenkamp, and W.A. de Heer. Exceptional ballistic transport in epitaxial graphene nanoribbons. *Nature*, 506:394, 2014.

[87] J. Baringhaus, F. Edler, and C. Tegenkamp. Edge-states in graphene nanoribbons: A combined spectroscopy and transport study. *Journal of Physics: Condensed Matter*, 25:392001, 2013.

[88] I. Palacio, A. Celis, M. N. Nair, A. Gloter, A. Zobelli, M. Sicot, D. Malterre, M. S. Nevius, W. A. de Heer, C. Berger, E. H. Conrad, A. Taleb-Ibrahimi, and A. Tejeda. Atomic structure of epitaxial graphene sidewall nanoribbons: Flat graphene, miniribbons, and the confinement gap. *Nanoletters*, 15:182, 2015.

[89] J. Hicks, A. Tejeda, A. Taleb-Ibrahimi, M. S. Nevius, F. Wang, K. Shepperd, J. Palmer, F. Bertran, P. Le Fèvre, J. Kunc, W. A. de Heer, C. Berger, and

E. H. Conrad. A wide-bandgap metal-semiconductor-meteal nanostructure made entirely from graphene. *Nature Physics*, 9:49, 2012.

[90] M. Sprinkle, J. Hicks, A. Tejeda, A. Taleb-Ibrahimi, P. Le Fèvre, F. Bertran, H. Tinkey, M. C. Clark, P. Soukiassian, D. Martinotti, J. Hass, and E. H. Conrad. Multilayer epitaxial graphene grown on the SiC(000-1) surface; structure and electronic properties. *Journal of Physics D: Applied Physics*, 43:374006, 2010.

[91] J. Baringhaus, A. Stör, S. Forti, S. A. Krasnikov, A. A. Zakharov, U. Starke, and C. Tegenkamp. Bipolar gating of epitaxial graphene by intercalation of Ge. *Applied Physics Letters*, 104:261602, 2014.

[92] S. Hertel, D. Waldmann, J. Jobst, A. Albert, M. Albrecht, S. Reshanov, A. Schoner, M. Krieger, and H.B. Weber. Tailoring the graphene/silicon carbide interface for monolithic wafer-scale electronics. *Nature Communications*, 3:957, 2012.

[93] J. Johnson, A. Behnam, S. Pearton, and A. Ural. Hydrogen sensing using Pd-functionalized multi-layer graphene nanoribbon networks. *Advances Materials*, 22:4877, 2010.

[94] F. Traversi, C. Raillon, S. M. Benameur, K. Liu, S. Khlybov, M. Tosun, D. Krasnozhon, A. Kis, and A. Radenovic. Detecting the translocation of DNA through a nanopore using graphene nanoribbons. *Nature Nanotechnology*, 8:939, 2013.

[95] M. Freitag, T. Low, W. Zhu, H. Yan, F. Xia, and P. Avouris. Photocurrent in graphene harnessed by tunable intrinsic plasmons. *Nature Communications*, 4:1951, 2013.

[96] S.-F. Shi, X. Xu, D. C. Ralph, and P. L. McEuen. Plasmon resonance in individual nanogap electrodes studied using graphene nanoconstrictions as photodetectors. *Nanoletters*, 11:1814, 2011.

[97] V. Ryzhii, M. Ryzhii, M. S. Shur, V. Mitin, A. Satou, and T. Otsuji. Resonant plasmonic terahertz detection in graphene split-gate field-effect transistors with lateral p-n junctions. *Journal of Physics D: Applied Physics*, 49:315103, 2012.

[98] F. Schwierz. Graphene transistors: Status, prospects, and problems. *Proceedings of the IEEE*, 101:1567, 2013.

[99] Y. Liu, L. Zhang, M. K. Brinkley, G. Bian, T. Miller, and T.-C. Chiang. Phonon-induced gaps in graphene and graphite observed by angle-resolved photoemission. *Physical Review Letters*, 105:136804, 2010.

[100] W. Liu, B. L. Jackson, J. Zhu, C.-Q. Miao, C.-H. Chung, Y.-J. Park, K. Sun, J. Woo, and Y.-H. Xie. Large scale pattern graphene electrode for high performance in transparent organic single crystal field-effect transistors. *ACS Nano*, 4:3927, 2010.

[101] V. Ryzhii, M. Ryzhii, A. Satou, and T. Otsuji. Current-voltage characteristics of a graphene-nanoribbon field-effect transistor. *AIP Journal of Applied Physics*, 103:094510, 2008.

[102] H. Mohamadpour and A. Asgari. Graphene nanoribbon tunneling field effect transistors. *Physica E: Low-dimensional systems and nanostructures*, 46:270, 2012.

[103] J. Chen. *Introduction to Scanning Tunneling Microscopy.* Oxford University Press, 1993.

[104] M. Schmid. The scanning tunneling microscope. `http://www.iap.tuwien.ac.at/www/surface/stm_gallery/stm_schematic`.

[105] Washington University. Scanning tunneling microscopy. `https://depts.washington.edu/nanolab/NUE_UNIQUE/Lab_Units/5_Lab_Unit_STM.pdf`.

[106] D. B. Williams and C. B. Carter. *Transmission Electron Microscopy: A textbook for Materials Science.* Springer Science, 2009.

[107] X. Li, A. Gloter, H. Gu, X. Cao, P. Jin, and C. Colliex. Role of epitaxial microsctructure, stress and twin boundaries in the metal-insulator transition mechanism in VO2/Al2O3 heterostructures. *Acta Materialia*, 61:6443, 2013.

[108] B. Fultz and J. M. Howe. *Transmission Electron Microscopy and Diffractometry of Materials.* Springer, 2008.

[109] Jeol. Glossary of TEM terms. `http://www.jeol.co.jp/en/words/emterms/search_result.html?keyword=LAADF-STEM`.

[110] C. Colliex. *La microscopie électronique.* Puf, 1998.

[111] W. Zhang. *Photoemission Spectroscopy on High Temperature Superconductor: A study of Bi2Sr2CaCu2O8 by Laser-Based Angle-Resolved Photoemission.* Springer, 2013.

[112] D. Malterre, B. Kierren, Y. Fagot-Revurat, S. Pons, A. Tejeda, C. Didiot, H. Cercellier, and A. Bendounan. ARPES and STS investigation of Schockley states in thin metallic films and periodic nanostructures. *New Journal of Physics*, 9:391, 2007.

[113] A. Tejeda and D. Malterre. *Photoémission dans les solides.* EDP Sciences, 2015.

[114] I. Šrut, V. M. Trontl, P. Pervan, and M. Kralj. Temperature dependence of graphene growth on a stepped iridium surface. *Carbon*, 56:193, 2013.

[115] P. J. Fiebelman. Pinning of graphene to Ir(111) bu flat Ir dots. *Physical Review B*, 77:165419, 2008.

[116] A. T. N'Diaye, S. Bleikamp, P. J. Fiebelman, and T. Michely. Two-dimensional Ir cluster lattice on a graphene moiré on Ir(111). *Physical Review Letters*, 97:215501, 2006.

[117] H. Hattab, A. T. N'Diaye, D. Wall, G. Jnawali, J. Coraux, C. Busse, R. van Gastel, B. Poelsema, T. Michely, F.-J. Meyer zu Heringdorf, and M. Horn von Hoegen. Growth temperature dependent graphene alignement on Ir(111). *Applied Physics Letters*, 98:141903, 2011.

[118] L. Meng, R. Wu, L. Zhang, L. Li, S. Du, Y. Wang, and H.-J. Gao. Multi-oriented moiré superstructures of graphene on Ir(111): Experimental observations and theoretical models. *Journal of Physics: Condensed Matter*, 24:314214, 2012.

[119] J. Coraux, A. T. N'Diaye, M. Engler, C. Busse, D. Wall, N. Buckanie, F.-J. Meyer zu Heringdorf, R. van Gastel, B. Poelsema, and T. Michely. Growth of graphene on Ir(111). *New Journal of Physics*, 11:023006, 2009.

[120] E. Loginova, S. Nie, K. Thürmer, N. C. Bartelt, and K. F. McCarty. Defects on graphene on Ir(111): Rotational domains and ridges. *Physical Review B*, 80:085430, 2009.

[121] J. Coraux, A. T. N'Diaye, C. Busse, and T. Michely. Structural coherency of graphene on Ir(111). *Nanoletters*, 8:565, 2008.

[122] I. Pletikosić, M. Kralj, P. Pervan, R. Brako, J. Coraux, A. T. N'Diaye, C. Busse, and T. Michely. Dirac cones and minigaps for graphene on Ir(111). *Physical Review Letters*, 102:056808, 2009.

[123] F. Jean, T. Zhou, N. Bland, R. Felici, J. Coraux, and G. Renaud. Effect of preparation on the commensurabilities and thermal expansion of graphene on Ir(111) between 10 and 1300 K. *Physical Review B*, 88:165406, 2013.

[124] C. Busse, P. Lazić, R. Djemour, J. Coraux, T. Gerber, N. Atodiresei, V. Caciuc, R. Brako, A. T. N'Diaye, S. Blügel, J. Zegenhagen, and T. Michely. Graphene on Ir(111): Physisorption with chemical modulation. *Physical Review Letters*, 107:036101, 2011.

[125] M. Kralj, I. Plestikosić, P. Pervan, M. Milun, A. T. N'Diaye, C. Busse, T. Michely, J. Fujii, and I. Vobornik. Graphene on Ir(111) characterized by angle-resolved photoemission. *Physical Review B*, 84:075427, 2011.

[126] E. Starodub, A. Botswick, L. Moreschini, S. Nie, F. El Gabaly, K. F. McCarty, and E. Rotenberg. In-plane orientation effects on the electronic structure, stability, and raman scattering of monolayer graphene on Ir(111). *Physical Review B*, 83:125428, 2011.

[127] A. Varykhalov, D. Marchenki, M. R. Scholz, E. D. L. Rienks, T. K. Kim, G. Bihlmayer, J. Sánchez-Barriga, and O. Rader. Ir(111) surface state with giant rashba splitting persists under graphene in air. *Physical Review Letters*, 108:066804, 2012.

[128] S.-H. Phark, J. Borme, A. León Vanegas, M. Corbetta, D. Sander, and J. Kirschner. Scanning tunneling spectroscopy of epitaxial graphene nanoisland on Ir(111). *Nanoscale Research Letters*, 7:255, 2012.

[129] A. T. N'Diaye, J. Coraux, T. N. Plasa, C. Busse, and T. Michely. Structure of epitaxial graphene on Ir(111). *New Journal of Physics*, 10:043033, 2008.

[130] H. Vita, S. Böttcher, K. Horn, E. N. Voloshina, R. E. Ovcharenko, Th. Kampen, A. Thissen, and Yu. s. Dedkov. Understanding the origin of band gap formation in graphene on metals: graphene on Cu/Ir(111). *Scientific Reports*, 4:5704, 2014.

[131] M. Sicot, Y. Fagot-Revurat, B. Kierren, G. Vasseur, and D. Malterre. Copper intercalation at the interface of graphene on Ir(111) studied by scanning tunneling microscopy. *Applied Physics Letters*, 105:191603, 2014.

[132] I. Pletikosić. *Electronic states of epitaxial graphene on iridium: From almost neutral to highly doped graphene*. PhD thesis, University of Zagreb, 2012.

[133] W. J. Arnoult and R. B. McLellan. The solubility of carbon in rhodium, ruthenium, iridium and rhenium. *Scripta Metallurgica*, 6:1013, 1972.

[134] T. Bottoni. Étude par photoémission et spectroscopie tunnel des modifications des proprietés électroniques de graphène épitaxié sur Ir(111) induites par intercalation de Cu. Master's thesis, Institut Jean Lamour, 2013.

[135] A. T. N'Diaye. *Epitaxial graphene and cluster lattices on Iridium(111)*. PhD thesis, RWTH Aachen University, 2010.

[136] M. Andersen, L. Hornekaer, and B. Hammer. Understanding intercalation structures formed under graphene on Ir(111). *Physical Review B*, 90:155428, 2014.

[137] A. Mugarza, A. Mascaraque, V. Pérez-Dieste, V. Repain, S. Rousset, F. J. García de Abajo, and J. E. Ortega. Electron confinement in surface states on a stepped gold surface revealed by Angle-resolved Photoemission. *Physical Review Letters*, 87:107601, 2001.

[138] C. Didiot, V. Cherkez, B. Kierren, Y. Fagot-Revurat, and D. Malterre. Bulk state confinement and band folding in nanostructured surfaces. *Physical Review B*, 81:075421, 2010.

[139] C. Didiot, A. Tejeda, Y. Fagot-Revurat, V. Repain, B. Kierren, S. Rousset, and D. Malterre. Interacting quantum box superlattice by self-organized Co nanodots on Au(788). *Physical Review B*, 76:081404, 2007.

[140] D. Pacilé, P. Leicht, M. Papagno, P. M. Sheverdyaeva, P. Moras, C. Carbone, K. Krausert, K. Zielke, M. Fonin, Y. S. Dedkov, F. Mittendorfer, J. Doppler, A. Garhofer, and J. Redinger. Artificially lattice-mismatched graphene/metal interface: Graphene/Ni/Ir(111). *Physical Review B*, 87:035420, 2013.

[141] R. Decker, J. Brede, N. Atodiresei, V. Caciuc, S. Blügel, and R. Wiesendanger. Atomic-scale magnetism of cobalt-intercalated graphene. *Physical Review B*, 87:041403, 2013.

[142] I. Gierz, T. Suzuki, R. T. Weitz, D. S. Lee, B. Krauss, C. Riedl, U. Starke, H. Höchst, J. H. Smet, C. R. Ast, and K. Kern. Electronic decoupling of an epitaxial graphene monolayer by gold intercalation. *Physical Review B*, 81:235408, 2010.

[143] E. N. Voloshina, A. Generalov, M. Weser, S. Böttcher, K. Horn, and Y. S. Dedkov. Structural and electronic properties of the graphene/Al/Ni(111) intercalation system. *New Journal of Physics*, 13:113028, 2011.

[144] Y. S. Dedkov, A. M. Shikin, V. K. Adamchuk, S. L. Molodstov, C. Laubschat, A. Bauer, and G. Kaindl. Intercalation of copper underneath a monolayer of graphite on Ni(111). *Physical Review B*, 64:035405, 2001.

[145] A. M. Shikin, G. V. Prudnikova, and V. K. Adamchuk. Surface intercalation of gold underneath a graphite monolayer on Ni(111) studied by angle-resolved photoemission and high-resolution electron-energy-loss spectroscopy. *Physical Review B*, 62:13202, 2000.

[146] M. Gyamfi, T. Eelbo, M. Waśniowska, and R. Wiesendanger. Impact of intercalated cobalt on the electronic properties of graphene on Pt(111). *Physical Review B*, 85:205431, 2012.

[147] G. Giovannetti, P. A. Khomyakov, G. Brocks, V. M. Karpan, J. van den Brink, and P. J. Kelly. Doping graphene with metal contacts. *Physical Review Letters*, 101:026803, 2008.

[148] A. Varykhalov, M. R. Scholz, T. K. Kim, and O. Rader. Effect of noble-metal contacts doping and band gap of graphene. *Physical Review B*, 82:121101, 2010.

[149] M. F. Crommie, C. P. Lutz, and D. M. Eigler. Confinement of electrons to quantum corrals on a metal surface. *Science*, 262:218, 1993.

[150] T.-C. Chiang. Photoemission studies of quantum well states in thin films. *Surface Science Reports*, 39:181, 2000.

[151] A. Mugarza and J. E. Ortega. Electronic states at vicinal surfaces. *Journal of Physics : Condensed Matter*, 15:S3281, 2003.

[152] C. Kittel. *Introduction to Solid State Physics*. John Wiley and Sons, 2005.

[153] R. de L Kronig and W. G. Penney. Quantum mechanics of electrons in crystal lattices. *Proceedings of the Royal Society A*, 130:499, 1931.

[154] J. E. Ortega, J. Lobo-Checa, G. Peschel, S. Schirone, Z. M. Abd El-Fattah, M. Matena, F. Schiller, P. Borghetti, P. Gambardella, and A. Mugarza. Scattering of surface electrons by isolated steps versus periodic step arrays. *Physical Review B*, 87:115425, 2013.

[155] J. R. F. Lima. Electronic structure of a graphene superlattice with a modulated Fermi velocity. *Physics Letters A*, 379:1372, 2015.

[156] J. R. F. Lima. Controlling the energy gap of graphene by Fermi velocity engineering. *Physics Letters A*, 379:179, 2015.

[157] N. M. R. Peres. Scattering in ond-dimensional heterostructures described by the Dirac equation. *Journal of Physics:Condensed Matter*, 21:095501, 2009.

[158] R. Larciprete, S. Ulstrup, P. Lacovig, M. Dalmiglio, M. Bianchi, F. Mazzola, L. Hornekaer, F. Orlando, A. Baraldi, P. Hofmann, and S. Lizzit. Oxygen switching of the epitaxial graphene - metal interaction. *ACS Nano*, 6:9551, 2012.

[159] I. Pletikosić, M. Kralj, D. Šok čević, R. Brako, P. Lazíc, and P. Pervan. Photoemission and density functional theory study of Ir(111); energy band gap mapping. *Journal of Physics: Condensed Matter*, 22:135006, 2010.

[160] J. Wintterlin and M.-L. Bocquet. Graphene on metal surfaces. *Surface Science*, 603:1841, 2009.

[161] T. A. Land, T. Michely, R. J. Behm, J.C. Hemminger, and G. Comsa. STM investigation of single layer graphite structures produced on Pt(111) by hydrocarbon decomposition. *Surface Science*, 264:261, 1992.

[162] M. Gao, Y. Pan, L. Huang, H. Hu, L. Z. Zhang, H. M. Guo, S. X. Du, and H.-J. Gao. Epitaxial growth and structural property of graphene on Pt(111). *Applied Physics Letters*, 98:033101, 2011.

[163] P. Sutter, J. T. Sadowski, and E. Sutter. Graphene on Pt(111): Growth and substrate interaction. *Physical Review B*, 80:245411, 2009.

[164] H. Ueta, M. Saida, C. Nakai, Y. Yamada, M. Sasaki, and S. Yamamoto. Highly oriented monolayer graphite formation on Pt(111) by a supersonic methane beam. *Surface Science*, 560:183, 2004.

[165] E. Cazzanelli, T. Caruso, M. Castriota, A. R. Marino, A. Politano, G. Chiarello, M. Giarola, and G. Mariotto. Spectroscopic characterization of graphene films grown on Pt(111) surface by chemical vapor deposition of ethylene. *Journal of Raman spectroscopy*, 44:1393, 2013.

[166] G. S. Hodges. *Growth of graphene films on Pt(111) by thermal decomposition of propylene*. PhD thesis, Texas State University - San Marcos, 2010.

[167] R. Addou and M. Batzill. Defects and domain boundaries in self-assembled terephthalic acid (TPA) monolayers on CVD-grown graphene on Pt(111). *Langmuir*, 29:6354, 2013.

[168] T. Gao, S. Xie, Y. Gao, M. Liu, Y. Chen, Y. Zhang, and Z. Liu. Growth and atomic-scale characterizations of graphene on multifaceted texture Pt foils prepared by chemical vapor deposition. *ACS Nano*, 5:9194, 2011.

[169] A. Tejeda and G. Baudot and V. Repain and S. Rousset and J. Ferré and J. P. Jamet and A. Thiaville and L. Barbier. Periodic magnetic anisotropy in ultrathin ferromagnetic films on faceted surfaces. *Europhysics Letters*, 71:117, 2005.

[170] M. Sprinkle, M. Ruan, Y. Hu, J. Hankinson, M. Rubio-Roy, B. Zhang, X. Wu, C. Berger, and W. A. de Heer. Directed self-organization of graphene nanoribbons on SiC. *Nature Nanotechnology*, 5:727, 2010.

[171] D. A. Areshkin, D. Gunlycke, and C. T. White. Ballistic transport in graphene nanostrips in the presence of disorder: Importance of edge effects. *Nano Letters*, 7:204, 2007.

[172] D. Querlioz, Y. Apartet, A. Valentin, K. Huet, A. Bournel, S. Galdin-Retailleau, and P. Dolfus. Suppression of the orientation effects on bandgap in graphene nanoribbons in the presence of edge disorder. *Applied Physical Letters*, 92:042108, 2008.

[173] A. Cresti and S. Roche. Edge-disorder-dependent transport length scales in graphene nanoribbons: From Klein defects to the superlattice limit. *Physical Review B*, 79:233404, 2009.

[174] W. A. de Heer, C. Berger, M. Ruan, M. Sprinkle, X. Li, Y. Hu, B. Zhang, J. Hankinson, and E. Conrad. Large area and structured epitaxial graphene produced by confinement controlled sublimation of silicon carbide. *Proceedings of the National Academy of Sciences*, 108:16900, 2011.

[175] C. Riedl, C. Coletti, and U. Starke. Structural and electronic properties of epitaxial graphene on SiC(0001): A review of growth, characterization, transfer doping and hydrogen intercalation. *Journal of Physics D*, 43:374009, 2010.

[176] M. S. Nevius, F. Wang, C. Mathieu, N. Barrett, A. Sala, T. O. Mentes, A. Locatelli, and E. H. Conrad. The bottom-up growth of edge specific graphene nanoribbons. *Nano Letters*, 14:6080, 2014.

[177] H. Zaid, M. H. Berger, D. Jalabert, M. Walls, R. Akrobetu, I. Fongkaew, W. R. L. Lambrecht, N. J. Goble, X. P. A. Gao, P. Berger, and A. Sehirlioglu. Atomic-resolved depth profile of strain and cation intermixing around LaAlO3/SrTiO3 interfaces. *Scientific Reports*, 6:28118, 2016.

[178] F. Ming and A. Zangwill. Model and simulations of the epitaxial growth of graphene on non-planar 6H-SiC surfaces. *Journal of Physics D: Applied Physics*, 45:154007, 2012.

[179] W. Norimatsu and M. Kusunoki. Transitional structures of the interface between graphene and 6H-SiC(0001). *Chemical Physics Letters*, 468:52, 2009.

[180] K. V. Emtsev, F. Speck, Th. Seyller, and L. Ley. Interaction, growth and ordering of epitaxial graphene on SiC(0001) surfaces: A comparative photoelectron spectroscopy study. *Physical Review B*, 77:155303, 2008.

[181] C. Riedl, U. Starke, M. Franke, and K. Heinz. Structural properties of the graphene-SiC(0001) interface as a key for the preparation of homogeneous large-terrace graphene surfaces. *Physical Review B*, 76:245406, 2007.

[182] G. Nicotra, Q. M. Ramasse, I. Deretzis, A. La Magna, C. Spinella, and F. Giannazzo. Delaminated graphene at silicon carbide facets: Atomic scale imagning and spectroscopy. *ACS Nano*, 7:3045, 2013.

[183] M. Ostler, I. Deretzis, S. Mammadov, F. Giannazzo, G. Nicotra, C. Spinella, Y. Seyller, and A. La Magna. Direct growth of quasi-free standing epitaxial graphene on nonpolar SiC surfaces. *Physics Review B*, 88:085408, 2013.

[184] N. Dobigeon and N. Brun. Spectral mixture analysis of EELS spectrum-images. *Ultramicroscopy*, 120:25, 2012.

[185] M. S. Nevius, M. Conrad, F. Wang, A. Celis, M.N. Nair, A. Taleb-Ibrahimi, A. Tejeda, and E. H. Conrad. Semiconducting graphene from highly ordered substrate interactions. *Physical Review Letters*, 115:136802, 2015.

[186] D. Rossouw, G. A. Botton, E. Najafi, V. Lee, and A. P. Hitchcock. Metallic and semiconducting single-walled carbon nanotubes: Differentiating individual SWCNT by their carbon 1s spectra. *ACS Nano*, 6:10965, 2012.

[187] S. Kim, J. Ihm, H. J. Choi, and Y.-W. Son. Origin of anomalous electronic structures of epitaxial graphene on silicon carbide. *Physical Review Letters*, 100:176802, 2008.

[188] F. Varchon, R. Feng, J. Hass, X. Li, B. Ngoc Nguyen, C. Naud, P. Mallet, J.-Y. Veuillen, C. Berger, E. H. Conrad, and L. Magaud. Electronic structure of epitaxial graphene layers on SiC: Effect of the substrate. *Physical Review Letters*, 99:126805, 2007.

[189] D. Prezzi, D. Varsano, A. Ruini, A. Marini, and E. Molinari. Optical properties of graphene nanoribbons: The role of many-body effects. *Physical Review B*, 77:041404, 2009.

[190] D. Prezzi, D. Varsano, A. Ruini, , and E. Molinari. Quantum dot states and optical excitations of edge modulated graphene nanoribbons. *Physical Review B*, 84:041401, 2011.

université PARIS-SACLAY
ÉCOLE DOCTORALE
Physique en île-de-France (EDPIF)

Titre : Gap en graphène sur des surfaces nanostructurées de SiC et des surfaces vicinales de métaux nobles.

Mots-clés : graphène, nanostructure, bande interdite, STM, ARPES, STEM

Résumé : L'électronique basé sur le graphène fait face à un verrou technologique, qui est l'absence d'une bande interdite (gap) permettant une commutation entre les états logiques allumé et éteint. Les nano-rubans de graphène rendent possible l'obtention de ce gap mais il est difficile de produire de tels rubans avec une largeur précise à l'échelle atomique et des bords bien ordonnés. Le confinement électronique est une façon élégante d'ouvrir un gap et peut en principe être réglé en ajustant la largeur des nano-rubans. Cette thèse est consacrée à la compréhension de l'ouverture du gap par nano-structuration. Nous avons suivis deux approches : l'introduction d'un potentiel super-périodique sur le graphène par des substrats vicinaux de métaux nobles et le confinement électronique dans des nano-rubans sur des facettes artificielles du SiC.

Des potentiels super-périodiques ont été introduits avec deux substrats nano-structurés: l'Ir(332) et un cristal courbé de Pt(111) multi-vicinale. Le graphène modifie les marches initiales des substrats et les transforme en une succession de terrasses (111) et de régions d'accumulation de marches, observés par STM. La nano-structuration du substrat induit alors un potentiel super-périodique dans le graphène entraînant l'ouverture de gaps sur la bande π du graphène observée par ARPES, ce qui est cohérent avec la périodicité structurale observé par STM et LEED. Les gaps peuvent être convenablement expliqués par un modèle de type hamiltonien de Dirac; ce dernier nous permet de retrouver la force du potentiel à la jonction entre les terrasses (111) et la région d'accumulation des marches. La force du potentiel dépends du substrat, de la périodicité associée à la surface et du type de bord des marches (soit type A ou B). Nous avons aussi changé le potentiel de surface en intercalant du Cu sur l'Ir(332), qui reste préférentiellement au niveau de l'accumulation des marches. La surface présente des régions dopées n alors que les régions non-intercalées restent dopées p, conduisant à une succession de rubans dopés n et p pour une même couche de graphène continue.

La seconde approche pour contrôler le gap est par confinement électronique dans des nano-rubans de graphène synthétisés sur du SiC. Ces rubans sont obtenus sur des facettes du SiC ordonnées périodiquement. Comme l'ouverture d'un gap d'origine inconnue avait été observé par ARPES, nous avons réalisé les premières études atomiquement résolues par STM. Nous démontrons la régularité et la chiralité des bords, nous localisons précisément les nanorubans de graphène sur les facettes et nous identifions des mini-facettes sur du SiC. Afin de comprendre le couplage entre le graphène et le substrat, nous avons étudié une coupe transversale par STEM/EELS, en complement des études par ARPES et STM/STS. Nous observons que la facette $(1\bar{1}07)$ où le graphène se trouve présente un sub-facettage sur les extrémités haute et base. Le sub-facettage comprend des mini-terraces (0001) et des mini-facettes $(1\bar{1}05)$. Le graphène s'étend tout au long du la région sub-facettée, et est couplé au substrat dans les mini-terraces (0001), ce qui le rend semi-conducteur. En revanche, le graphène au-dessus des mini-facettes $(1\bar{1}05)$ est découplé du substrat mais présente un gap observé par EELS, et compatible avec les observations faites par ARPES. L'origine du gap est expliqué par le confinement électronique sur des nano-rubans de graphène de 1 - 2 nm de largeur localisés sur ces mini-facettes $(1\bar{1}05)$.

Université Paris-Saclay
Espace Technologique / Immeuble Discovery
Route de l'Orme aux Merisiers RD 128 / 91190 Saint-Aubin, France

université PARIS-SACLAY
ÉCOLE DOCTORALE
Physique en île-de-France (EDPIF)

Title : Gap opening in graphene on nanostructured SiC and vicinal noble metal surfaces.

Keywords : graphene, nanostructure, band gap, STM, ARPES, STEM

Abstract : The major challenge for graphene-based electronic applications is the absence of the band-gap necessary to switch between on and off logic states. Graphene nanoribbons provide a route to open a band-gap, though it is challenging to produce atomically precise nanoribbon widths and well-ordered edges. A particularly elegant method to open a band-gap is by electronic confinement, which can in principle be tuned by adjusting the nanoribbon width. This thesis is dedicated to understanding the ways of opening band-gaps by nanostructuration. We have used two approaches: the introduction of a superperiodic potential in graphene on vicinal noble metal substrates and the electronic confinement in artificially patterned nanoribbons on SiC.

Superperiodic potentials on graphene have been introduced by two nanostructured substrates, Ir(332) and a multivicinal curved Pt(111) substrate. The growth of graphene modifies the original steps of the pristine substrates and transforms them into an array of (111) terraces and step bunching areas, as observed by STM. This nanostructuration of the underlying substrate induces the superperiodic potential on graphene that opens mini-gaps on the π band as observed by ARPES and consistent with the structural periodicity observed in STM and LEED. The mini-gaps are satisfactorily explained by a Dirac-hamiltonian model, that allows to retrieve the potential strength at the junctions between the (111) terraces and the step bunching. The potential strength depends on the substrate, the surface periodicity and the type of step-edge (A or B type). The surface potential has also been modified by intercalating Cu on Ir(332), that remains preferentially on the step bunching areas, producing there n-doped ribbons, while the non-intercalated areas remain p-doped, giving rise to an array of n- and p- doped nanoribbons on a single continuous layer.

In the second approach to control the gap, we have studied the gap opening by electronic confinement in graphene nanoribbons grown on SiC. These ribbons are grown on an array of stabilized sidewalls on SiC. As a band-gap opening with unclear atomic origin had been observed by ARPES, we carried-out a correlated study of the atomic and electronic structure to identify the band gap origin. We performed the first atomically resolved study by STM, demonstrating the smoothness and chirality of the edges, finding the precise location of the metallic graphene nanoribbon on the sidewalls and identifying an unexpected mini-faceting on the substrate. To understand the coupling of graphene to the substrate, we performed a cross-sectional study by STEM/EELS, complementary of our ARPES and STM/STS studies. We observe that the $(1\bar{1}07)$ SiC sidewall facet is sub-faceted both at its top and bottom edges. The subfacetting consists of a series of (0001) miniterraces and $(1\bar{1}05)$ minifacets. Graphene is continuous on the whole subfacetting region, but it is coupled to the substrate on top of the (0001) miniterraces, rendering it there semiconducting. On the contrary, graphene is decoupled on top of the $(1\bar{1}05)$ minifacets but exhibits a bandgap, observed by EELS and compatible with ARPES observations. Such bandgap is originated by electronic confinement in the 1 - 2 nm width graphene nanoribbons that are formed over the $(1\bar{1}05)$ minifacets.

Université Paris-Saclay
Espace Technologique / Immeuble Discovery
Route de l'Orme aux Merisiers RD 128 / 91190 Saint-Aubin, France